
Attosecond Electron Spectroscopy Theory and its Applications

Justin Gagnon



München 2010

Attosecond Electron Spectroscopy Theory and its Applications

Justin Gagnon

Dissertation
an der Fakultät für Physik
der Ludwig-Maximilians-Universität
München

vorgelegt von
Justin Gagnon
aus Halifax, Nova Scotia, Canada

München, den 3. Dezember 2010

Erstgutachter: Prof. Dr. Ferenc Krausz

Zweitgutachter: Prof. Dr. Armin Scrinzi

Tag der mündlichen Prüfung: 12. Januar 2011

Contents

| | |
|--|-------------|
| Contents | vi |
| List of Figures | viii |
| List of Tables | ix |
| Summary | xiii |
| Zusammenfassung | xv |
| List of Contributions | xvii |
| Introduction | 1 |
| 1 Characterizing Attosecond Pulses | 9 |
| 1.1 The RABITT Technique | 9 |
| 1.2 Gating the Attosecond Pulse Train | 11 |
| 1.2.1 Temporal Gating of the Attosecond Pulse Train | 14 |
| 1.2.2 Spectral Filtering of the Attosecond Pulse Train | 15 |
| 1.3 The Attosecond Streaking Measurement | 17 |
| 1.4 A Classical Trajectory Analysis of Streaking for Extracting the Attosecond Chirp | 21 |
| 1.5 The Semi-Classical Description of Attosecond Streaking | 30 |
| 1.6 The Attosecond FROG | 34 |
| 1.6.1 FROG Reconstruction | 36 |
| 1.6.2 The PCGPA | 44 |
| 1.6.3 The LSGPA | 46 |
| 1.6.4 A Comparison Between the LSGPA and the PCGPA | 49 |
| 1.7 The Robustness of Attosecond Streaking Measurements | 51 |
| 1.7.1 Streaking with a Single Isolated Attosecond Pulse | 53 |
| 1.7.2 Streaking with a Sequence of Two Attosecond Pulses | 58 |

| | | |
|----------|---|------------|
| 2 | Measuring Attosecond Electron Wave Parcels | 67 |
| 2.1 | The FROG Characterization of an Attosecond Electron Wave Parcel from a Streaking Measurement | 67 |
| 2.2 | Laser-Dressed Scattering of an Attosecond Electron Wave Packet | 73 |
| | Conclusion | 85 |
| A | Energy-Resolved Photoelectron Angular Distributions | 87 |
| A.1 | The Coupled-Wave Lippmann-Schwinger Equation | 88 |
| A.2 | Bound-Free Transition Dipole Matrix Elements | 91 |
| A.3 | Scattering States for a Long Range Potential | 93 |
| A.4 | A Treatment of the Scattering Potential for Atoms and Molecules | 95 |
| B | A Little Bit of This and a Little Bit of That | 99 |
| B.1 | The Obligatory Coordinate Transformations | 99 |
| B.2 | The Beloved Atomic Units | 101 |
| B.3 | A Simple Relation Between Bandwidth, Dispersion and Duration | 103 |
| | Bibliography | 113 |
| | Acknowledgments | 115 |
| | Personal Record | 120 |

List of Figures

| | | |
|------|---|----|
| 1 | Schematic of the recollision process | 5 |
| 1.1 | A RABITT measurement | 10 |
| 1.2 | Recollision energies as a function of time for short and long driving laser pulses | 12 |
| 1.3 | An attosecond streaking measurement | 19 |
| 1.4 | The basic manifestations of the attosecond streaking effect | 20 |
| 1.5 | Streaking effects for a gaussian attosecond pulse | 25 |
| 1.6 | Streaking measurements with a non-gaussian XUV spectrum | 26 |
| 1.7 | Illustration of the iCrap procedure for a cosine-like streaking field | 28 |
| 1.8 | Illustration of the iCrap procedure for a sine-like streaking field | 29 |
| 1.9 | Application of iCrap to very noisy spectrograms | 29 |
| 1.10 | Comparison between the CVA and the TDSE | 33 |
| 1.11 | The basic loop of the PCGPA and the LSGPA | 38 |
| 1.12 | Characterization of an attosecond pulse from a spectrogram computed by numerical evaluation of the TDSE | 40 |
| 1.13 | FROG retrieval of a sequence of two attosecond pulses from a streaking spectrogram | 41 |
| 1.14 | The signal matrix assumed by the LSGPA | 47 |
| 1.15 | Comparison between the LSGPA and the PCGPA | 50 |
| 1.16 | Streaking spectrograms for various uncertainties in the parameters of an isolated attosecond pulse | 53 |
| 1.17 | Attosecond FROG retrieval with uncertainty in the central energy | 55 |
| 1.18 | Attosecond FROG retrieval with uncertainty in the bandwidth | 56 |
| 1.19 | Attosecond FROG retrieval with uncertainty in the group-delay dispersion | 56 |
| 1.20 | Attosecond FROG retrieval with uncertainty in the timing for a single attosecond pulse | 57 |
| 1.21 | Streaking spectrograms for various uncertainties in the parameters of a sequence of two attosecond pulses | 59 |
| 1.22 | Attosecond FROG retrieval with uncertainty in the relative intensity between two attosecond pulses | 60 |
| 1.23 | Attosecond FROG retrieval with uncertainty in the relative phase between two attosecond pulses | 61 |

| | | |
|------|---|----|
| 1.24 | Attosecond FROG retrieval with uncertainty in the relative timing between two attosecond pulses | 62 |
| 1.25 | Fringe positions for different values of relative timing between two attosecond pulses | 63 |
| 1.26 | Attosecond FROG retrieval with uncertainty in the timing for a sequence of two attosecond pulses | 64 |
| 2.1 | FROG retrieval of an electron wave parcel | 70 |
| 2.2 | Two-path interference of an electron emitted from a localized state | 74 |
| 2.3 | Photoelectron spectra for right-going and left-going wave packets | 76 |
| 2.4 | Comparison of TDSE and CVA photoelectron spectra for a spatially extended system | 77 |
| 2.5 | A wave parcel represented in position space | 78 |
| 2.6 | The effect of a control field on the reflected wave parcel | 80 |
| 2.7 | Comparison of TDSE and classically-adjusted photoelectron spectra for a spatially extended system | 82 |
| B.1 | Illustration of spherical and cylindrical coordinate vectors | 99 |

List of Tables

| | | |
|-----|---|-----|
| B.1 | Transformations between rectangular, cylindrical and spherical coordinates | 100 |
| B.2 | Orthogonal unit vectors $\hat{\mathbf{x}}, \hat{\mathbf{y}}, \hat{\mathbf{z}}, \hat{\boldsymbol{\rho}}, \hat{\boldsymbol{\phi}}, \hat{\mathbf{r}}, \hat{\boldsymbol{\theta}}$ in rectangular, cylindrical and spherical coordinates | 100 |
| B.3 | Common differential operators in rectangular, cylindrical and spherical coordinates | 100 |
| B.4 | Physical constants in SI and atomic units | 101 |
| B.5 | Atomic units of fundamental physical quantities with their values in SI units | 102 |

I've had enough of someone else's propaganda. I'm for truth, no matter who tells it. I'm for justice, no matter who it's for or against.

Malcolm X

Summary

Since the original prediction and demonstration of attosecond pulses, attosecond physics has entrenched itself in the ultrafast sciences, and promises to advance a wide range of scientific disciplines. It has the potential to provide key developments and insights in several research areas, such as atomic physics, quantum chemistry, biology and medicine.

At present, engaging in this novel field of research is rather prohibitive, due to the high costs of cutting-edge technology and a steep learning curve. After all, playing with attosecond pulses is tantamount to playing with the shortest events ever made by man! Nonetheless, these are just typical growing pains of a new and exciting research area, and will eventually subside to make attosecond science accessible to a broad research community. In the meanwhile, as this promising field is taking its baby steps, it is the responsibility of those working at the cutting edge to propose novel experiments, and develop the tools and models that will be used in the future, as the field matures.

Attosecond science comprises two frontiers: (i) the generation and characterization of increasingly intense, energetic, short and isolated attosecond pulses; and (ii) the design of experiments to probe physical systems on the attosecond time scale, the holy grail being the attosecond pump-attosecond probe time-resolved spectroscopic measurement. The second frontier offers a deeper understanding of the temporal behavior of the microcosm, but relies on advancements made in the first one. At present, both of these frontiers heavily rely on the attosecond streaking technique, which consists in energy-resolving photoelectrons ejected by an attosecond extreme ultraviolet pulse, in the presence of a phase-stabilized and temporally synchronized near-infrared field. Although it was originally devised as a means to characterize attosecond pulses, this measurement technique has even produced new discoveries in atomic and solid-state physics, due to pioneering experiments by M. Drescher, A. Cavalieri, G. Sansone, M. Schultze, and others, and has inspired novel theories of laser-dressed photoionization by V. S. Yakovlev, A. Scrinzi, O. Smirnova, M. Y. Ivanov and others.

In the first part of this thesis, I focus on new methods I developed [II,III,IV,XII] for the analysis of attosecond streaking measurements [I,V,VI,VII,IX,XI]. One of these methods [XII], based on a formalism I devised based on electron trajectories in a laser field, can directly recover the chirp of an attosecond pulse from a set of streaked photoelectron spectra. Next, I describe a robust optimization algorithm [II,III,IV], based on a formalism due to M. Kitzler *et al.*, that can completely recover the temporal profile of an attosecond pulse with an arbitrary shape. This optimization algorithm was used to characterize the

field of ~ 80 as pulses [I], the shortest on record, and to uncover a delay of ~ 20 as between the photoemissions from the $2s$ and $2p$ sub-shells of neon [VII]; both experiments were performed here at the Max Planck Institut für Quantenoptik in 2008 and 2010, respectively.

Moreover, during the course of this work, it was established [VIII] by V. S. Yakovlev *et al.* that the attosecond streaking technique generally measures a quantity that is related to the photoelectron wave packet, not the attosecond light pulse. Only when the energy-resolved dipole response, given by the bound-free transition matrix elements, is nearly constant can we take the electron wave packet as a replica of the attosecond pulse. In light of this finding, I show that the attosecond streaking technique provides a means to measure and even time-resolve the energy-dependent *phase* of transition dipole matrix elements.

Finally, I consider the laser-dressed scattering of an attosecond photoelectron wave packet [X]. I show that the scattering of a photoelectron, emitted by an attosecond pulse from a localized state in a spatially extended system, can be influenced by a near-infrared laser field. Measuring the photoelectron spectrum reveals an interference pattern which is affected by the intensity of the near-infrared field. To describe these effects, I introduce a model based on classical trajectories that quantitatively predicts laser-dressed photoelectron spectra for such a spatially-extended system.

Zusammenfassung

Seit der ursprünglichen Vorhersage und Realisierung von Attosekundenpulsen, hat sich die Attosekundenphysik in der kurz-zeit Physik etabliert und verspricht in einem breiten Spektrum von Fachrichtungen grosse Fortschritte. Es hat das Potenzial, wichtige Entwicklungen und Einblicke in mehreren Forschungsbereichen, wie zum Beispiel der Atomphysik, der Quanten-Chemie, der Biologie und der Medizin zu bieten.

Durch die der hohen Kosten für modernste Technologie und die schnelle Entwicklung ist es derzeitiger fast unerschwinglich in diesen neuartigen Forschungsbereich einzusteigen. Immerhin ist das Erzeugen von Attosekundenpulsen gleichbedeutend mit der Erzeugung mit dem kürzesten Ereignis, das jemals von der Menschheit erzeugt wurde! Dennoch sind diese nur typische Geburtswehen eines neuen und spannenden Forschungsfelds, die schließlich abklingen werden, und auf diese Weise wird Attosekundenphysik für ein breites Forschungs-Community zugänglich sein. Mittlerweile, während dieses viel versprechende Feld die ersten Schritte unternimmt, ist es die Verantwortung von denjenigen, die an der wegbereitenden Technologie arbeiten, neue Experimente zu erdenken, und Werkzeuge und Modelle zu entwickeln, die in der Zukunft angewendet werden können.

Attosekundenphysik besteht aus zwei Felder die stets weiter ausgedehnen: (i) die Erzeugung und Charakterisierung von Attosekundenpulse die immer intensiver, energetischer und kürzer werden; und (ii) die Gestaltung von Experimenten für die Untersuchung von physikalischen Systemen an der Attosekunden-Zeitskala. Ein Beispiel für das zweite ist die zeitaufgelöste Attosekunden Pump- Attosekunden Probe Spectroscopie, die den Heilige Gral dieser Wissenschaft darstellt. Das zweite Feld eröffnet ein tieferes Verständnis der zeitlichen Abläufe des Mikrokosmos. Aber es beruht sich auf die Entwicklungen in dem ersten Feld. Momentan sind beide Felder auf die "Attosekunden-Streaking Methode" angewiesen, die auf der energieaufgelöste Messung von Photoelektronen beruht. Bei einer solchen Messung werden Photoelektronen von einem Attosekundenpuls im extremen ultraviolett herausgeschlagen und deren Bewegungen von phasenstabilisierten und zeitlich synchronisierten Pulsen in dem Nah-Infrarot beeinflusst. Obwohl diese Methode ursprünglich für die Charakterisierung von Attosekundenpulsen entstanden ist, hat sie uns neue Entdeckungen in der Atom- und Festkörperphysik gegeben. Wie dank den wegweisenden Experimente von M. Drescher, A. Cavalieri, G. Sansone, M. Schultze und weiteren gezeugt werden konnte. Ausserdem hat es neuartige Theorien zur Photoionisierung in gehgenwart eines Laserfeldes von unter anderen V. S. Yakovlev, A. Scrinzi, O. Smirnova, M. Y. Ivanov inspiriert.

Im ersten Teil dieser Doktorarbeit werde ich mich auf diese neue Methoden konzentrieren [II,III,IV,XII], welche ich für die Analysis von “Attosekunden-Streaking Experimenten” entwickelt habe [I,V,VI,VII,IX,XI]. Eine dieser Methoden [XII] basierend auf dem von mir entwickelten Formalismus mit Elektron-trajektorien in einem Laserfeld. Diese kann den Chirp von einem Attosekundenpuls aus einigen “streaked” Photoelektronenspektren sofort zurückgeben. Als Nächstes werde ich eine stabile Optimierung Methode vorstellen [II,III,IV], die auf dem eher quantum-mechanischen Formalismus von M. Kitzler et al. Beruht. Dieser kann das beliebige temporäre Profil eines Attosekundenpulses vollkommen zurückgeben. Der Optimierungsalgorithmus wurde für die Charakterisierung von ~ 80 as Pulsen benutzt [I], die bisher kürzeste gemessene Pulsdauer der Welt darstellt. Außerdem wurde die gleiche Methode für die Feststellung von einer Verzögerung von ~ 20 as zwischen den Photoemissionen von den $2s$ - und $2p$ -Energieniveaus von Neon angewendet [VII]; beide Experimente wurden am Max-Planck-Institut für Quantenoptik in den Jahren 2008 und 2010 durchgeführt.

Darüber hinaus wurde im Verlauf dieser Arbeit von V. S. Yakovlev klargestellt, dass die Attosekunden-Streaking-Methode eine Größe misst, die prinzipiell mit dem Photoelektronen-Wellenpaket und nicht mit dem Attosekunden-Lichtpuls im Zusammenhang steht [VIII]. Nur wenn das energieaufgelöste Dipolmoment, gegeben durch die gebunden-freien Übergangsmatrixelemente, näherungsweise konstant ist, kann das Elektronenwellenpaket als eine Nachbildung des Attosekundenpuls betrachtet werden. Anhand dieses Ergebnisses zeige ich dass die Attosekunden-Streaking-Methode die Möglichkeit bietet, die energieabhängige Phase der Übergangsmatrixelemente zu messen und sogar zeitlich aufzulösen.

Zum Schluss betrachte ich die Streuung eines Attosekunden-Photoelektronen-Wellenpakets in Gegenwart eines Laserfeldes [X]. Ich zeige, dass die Streuung eines Photoelektrons, das von einem lokalisierten Zustand in einem räumlich ausgedehntem System durch einen Attosekundenpuls herausgelöst wird, durch Laserstrahlung im Nahen Infrarot (NIR) beeinflusst werden kann. Die Messung des Photoelektronenspektrums zeigt ein Interferenzbild, das von der Intensität des NIR-Feldes beeinflusst wird. Um diesen Effekt zu beschreiben stelle ich eine Methode vor, die auf klassischen Trajektorien beruht und quantitative Aussagen zu Photoelektronenspektren in Gegenwart eines Laserfeldes erlaubt.

List of Contributions

This thesis is supported by the following journal and conference papers:

I. E. Goulielmakis, M. Schultze, M. Hofstetter, V. S. Yakovlev, J. Gagnon, M. Uiberacker, A. L. Aquila, E. M. Gullikson, D. T. Atwood, R. Kienberger, F. Krausz and U. Kleineberg, *Single-cycle nonlinear optics*, Science **320** (2008), 1614

◊ Using the FROG algorithm I developed [II], I performed an in-depth analysis of a streaking measurement performed by E. Goulielmakis and M. Schultze, yielding a record duration of 80 as (officially certified by GUINNESS WORLD RECORDS LTD).

II. J. Gagnon, E. Goulielmakis and V. S. Yakovlev, *The accurate FROG characterization of attosecond pulses from streaking measurements*, Appl. Phys. B **92** (2008), 25

◊ I introduced a new algorithm for processing attosecond streaking spectrograms. The algorithm is based on generalized projections, but adopts a radically new approach to the FROG algorithm, which is optimal for characterizing the shortest attosecond pulses. This paper was covered by the article *FROG reaches the attosecond scale* appearing in the July 7, 2008 edition of optics.org.

III. J. Gagnon and V. S. Yakovlev, *The robustness of attosecond streaking measurements*, Opt. Expr. **17** (2009), 17678

◊ For this paper, I analyzed the robustness of the attosecond streaking measurement, and specifically assessed the reliability of attosecond FROG retrieval against various uncertainties in the parameters of the attosecond pulse.

IV. J. Gagnon, V. S. Yakovlev, E. Goulielmakis, M. Schultze and F. Krausz, *A New Generalized Projections Algorithm Geared Towards Sub-100 Attosecond Pulse Characterization*, Ultrafast Phenomena XVI: Proceedings of the 16th International Conference **92** (2009), 911

◊ The algorithm described in [II] was presented to a broad audience in the ultrafast community.

V. E. Goulielmakis, M. Schultze, M. Hofstetter, M. Uiberacker, J. Gagnon, V. S. Yakovlev, U. Kleineberg, F. Krausz, *Sub-100-as soft x-ray pulses*, Ultrafast Phenomena XVI: Proceedings of the 16th International Conference **92** (2009), 3

◇ The results pertaining to the streaking measurement that yielded 80 as pulses [I] was presented to a broad audience in the ultrafast community.

VI. E. Goulielmakis, M. Schultze, F. Reiter, U. Graf, J. Gagnon, M. Hofstetter, V. S. Yakovlev, R. Kienberger, U. Kleineberg and F. Krausz, *En route to the generation and attosecond control of intense single-cycle light pulses*, 2009 IEEE LEOS Annual Meeting Conference Proceedings (2009), 313

◇ I provided data analysis and general theoretical support for the experimental results that were presented.

VII. M. Schultze, M. Fieß, N. Karpowicz, J. Gagnon, M. Korbman, M. Hofstetter, S. Neppl, A. L. Cavalieri, Y. Komninos, T. Mercouris, C. A. Nicolaides, R. Pazourek, S. Nagele, J. Feist, J. Burgdörfer, A. M. Azzeer, R. Ernstorfer, R. Kienberger, U. Kleineberg, E. Goulielmakis, F. Krausz and V. S. Yakovlev, *Delay in Photoemission*, Science **328** (2010), 1658

◇ With the help of the FROG algorithm I developed [II], I performed an in-depth analysis of the attosecond streaking measurement performed on neon, uncovering a delay in photoemission of ~ 20 as between the $2s$ and $2p$ shells.

VIII. V. S. Yakovlev, J. Gagnon, N. Karpowicz and F. Krausz, *Attosecond Streaking Enables the Measurement of Quantum Phase*, Phys. Rev. Lett. **105** (2010), 073001

◇ In this paper, I contributed ideas, and processed simulated streaking measurements using the FROG algorithm [II] to show that the analysis of attosecond streaking measurements generally recover not the attosecond pulse, but rather a quantity that is closely related to the free electron wave packet.

IX. M. Hofstetter, M. Schultze, M. Fieß, A. Guggenmos, J. Gagnon, E. Magerl, E. Botschafter, R. Ernstorfer, R. Kienberger, E. Gullikson, F. Krausz, U. Kleineberg, *First Attosecond Pulse Control by Multilayer Mirrors above 100 eV Photon Energy*, 17th International Conference on Ultrafast Phenomena, 2010

◇ I performed the FROG characterization of attosecond pulses to support the design goal of aperiodic multilayer XUV mirrors.

X. J. Gagnon, V. S. Yakovlev and F. Krausz, *Laser-dressed scattering of an attosecond electron wave packet*, Phys. Rev. A: At. Mol. Opt. Phys. **82** (2010), 033435

◇ I considered the scattering of an electron wave packet by a two-center potential, ejected by an attosecond pulse, in the presence of an infrared dressing field. I developed a semi-classical model based on electron trajectories for describing this process.

XI. M. Fieß, M. Schultze, E. Goulielmakis, B. Dennhardt, J. Gagnon, M. Hofstetter, R. Kienberger and F. Krausz, *Versatile apparatus for attosecond metrology and spectroscopy*, Rev. Sci. Instrum. **81** (2010), 093103

◇ Using the FROG algorithm I developed [II], I performed a FROG analysis of the attosec-

ond streaking measurement, shown in Fig. 6 and Fig. 7.

XII. J. Gagnon and V. S. Yakovlev, *The direct evaluation of attosecond chirp from a streaking measurement*, Appl. Phys. B (2010), accepted

◇ Using semi-classical analysis, I derive an equation describing the spectral broadening due to the streaking effect. I use this equation as a basis for a new method to evaluate the chirp of an attosecond pulse from a set of streaked photoelectron spectra.

XIII. M. G. Hofstetter, M. Schultze, M. Fieß, B. Dennhardt, A. Guggenmos, J. Gagnon, V. S. Yakovlev, E. Goulielmakis, R. Kienberger, E. M. Gulikson, F. Krausz and U. Kleineberg, *Attosecond dispersion control by extreme ultraviolet multilayer mirrors*, Opt. Expr. **19** (2011), 1767

◇ Using the algorithm described in [II], I performed the careful analysis of the streaking spectrograms and FROG characterization of attosecond pulses to support the design goal of aperiodic multilayer XUV mirrors.

Introduction

This thesis is concerned with tracking physical processes on an unprecedented time scale: that of electron motions in atoms and molecules. The necessary tool for such a measurement is the attosecond pulse, a flash of light that is used to take snapshots of the shortest events in the microcosm. In photography, the best pictures are taken when the photographer masters his camera, and keeps his eyes open for interesting photo opportunities. Likewise, attosecond metrology is most effective when the generation and characterization of attosecond pulses is accurate and robust, and it truly shines when used for capturing physical processes that are too fast to be resolved by any other means. Careful analysis of such “attosecond photographs” can uncover temporal detail that was previously overlooked, thereby allowing for the discovery of new phenomena. Accordingly, the main goal of this work is to provide theory and methods for analyzing and extracting information from attosecond measurements.

The notion of time-resolving physical phenomena is certainly not new or exotic, it’s simply part of our experience. Every day we face a world that unfolds as a sequence of events in time. As a result, our intuition entices us to adopt a perspective that is anchored in the time domain, which in turn influences the manner in which we pursue research. Indeed, numerous processes are currently scientifically studied by following their temporal evolution: cell division, plate tectonics, climate change, star and galaxy formation, and the collapse of the stock market, to name but a few examples. In fact, when discussing the properties of antimatter, we turn to the Stückelberg-Feynman interpretation which states that antiparticles are just negative-energy particles evolving backwards in time. Thus, we adhere to the concept of time evolution even when it makes barely any sense at all!

Yet, as science began exploring the microcosm at the beginning of the last century, time-resolved measurements had to be postponed because the technology of that era was simply incapable of tracking the extremely fast dynamics of atoms and molecules. Instead of resolving these processes in time, experiments were designed to detect their end-products—photons, electrons, atomic and molecular ions—which were time-integrated and *spectrally* resolved in some direction, infinitely far from the interaction region. Any time scales pertaining to the process in question were simply inferred from the spectrum.

These spectroscopic measurements still provided a wealth of information about the microcosm, enabling comparisons with theoretical predictions and ultimately leading to the great success of quantum mechanics. Yet, such measurements are incomplete because they are time-integrated, while quantum theory actually describes the *time-evolution* of quan-

tum mechanical processes. This temporal information is contained in an energy-dependent *spectral phase*, which is ignored in a time-integrated, purely spectroscopic measurement.

But since the advent of attosecond pulses, a host of fundamental physical phenomena have become available for us to fully investigate in the time domain—from the photoelectric effect, electronic decay processes and quantum coherences in atoms and molecules, all the way to shielding effects and charge transport in solids and nanoparticles. Of course, it goes without saying that a better understanding of such effects will make it possible to control how they unfold in time, by wielding the power of attosecond metrology.

Towards an Understanding of Strong-Field Light Matter Interactions

The field of attosecond science arose from rapid developments that were taking place in laser technology. As lasers were producing ever stronger radiation fields, a new regime of light-matter interactions became possible, one that presented new and puzzling effects which were difficult to interpret from time-integrated measurements.

It all started the day disco died, back in 1979 when Pierre Agostini discovered *above-threshold ionization* (ATI) [3], an ionization process in which an electron experiences a significant amount of free-free transitions after its ejection from an atom. The ATI photoelectron spectrum consists of discrete lines separated in energy by an amount equal to that of a laser quantum, $\hbar\omega_L$. The spectrum falls off with energy until it reaches a plateau, extending from about twice the ponderomotive energy, $2U_P$ ¹, all the way up to an energy of $10U_P$ [138]. Since the ATI spectrum abruptly changes at an energy of $2U_P$ [148], the high-energy portion of the spectrum extending from $2U_P$ all the way up to $10U_P$ is referred to as “hot”, “high-order”, or “high-energy” ATI (HATI). The discovery of ATI shook the community, since it was previously assumed that a bound electron would not absorb more photons than that needed to be free. At the very least, the probability of such an occurrence was assumed to be vanishingly small because, once free, an electron cannot absorb a photon due to energy and momentum conservation.

Shortly after the discovery of ATI, another curiosity appeared with the first observations [59, 126] of *high-order harmonic generation* (HHG) in noble gases²: the conversion of a near-infrared (NIR) field into extreme ultraviolet (XUV) radiation. The HHG spectrum consists of discrete peaks located at odd integer multiples of the fundamental NIR harmonic frequency. The spectrum initially falls off with energy, but then remains constant, forming a plateau which ends at an energy of about $W + 3.17U_P$ [119, 125], W being the ionization energy of the gas-phase medium.

¹The ponderomotive energy $U_P = \frac{e^2}{4m_e} \frac{F^2}{\omega^2} = \frac{I\lambda^2}{2\pi^2 c^3 \epsilon_0}$ is the cycle-averaged kinetic energy of an electron quivering in an electromagnetic field of wavelength $\lambda = 2\pi c/\omega$ and intensity $I = \frac{1}{2}c\epsilon_0 F^2$.

²Actually, a similar phenomenon was discovered by N. H. Burnett *et al.* in 1977 [25] for laser light incident on a solid target. As we’ll see in the next section, the generation of harmonics from solids is described by different mechanisms which are not treated here.

Although ATI and HHG seemed connected—they only occur in the presence of an intense laser field, and yield discrete spectra that are parameterized by the laser wavelength and intensity—there was no intuitive picture to explain their happenings. Of course, numerical solutions of the time-dependent Schrödinger equation (TDSE) reproduced both these effects [120]. But then again, TDSE simulations are little more than experiments on a computer. They provide about as much insight as, well, a modern-day TV news report!

Suddenly, in the late 1980's, a simple model [75, 38] was presented by Gallagher and Corkum *et al.* which managed to explain the structure of the ATI photoelectron spectrum, but only for low energies ($\lesssim 2U_P$). This model, heavily inspired by the work of Keldysh and others [108, 5, 42, 150], describes a two-step process where an electron is first extracted from the atom by the strong laser field (step 1), then quivers and drifts in the field (step 2) before reaching the detector. The model treats the propagation of the free electron in a laser field using ordinary classical mechanics, and ad-hoc ionization rates are taken from tunneling theory to account for the ionization step. Based on these considerations, this “two-step” model was able to explain the low-energy structure of ATI spectra for linearly and circularly polarized NIR laser fields. Now, with one of the strong-field phenomena already accounted for, the race was on to explain the others: the high-energy part of the ATI spectrum, and the mysterious properties of the HHG spectrum.

This quasi-classical two-step model drew some attention at the time, as it represented a paradigm shift in atomic physics. Since N. Bohr and A. Sommerfeld, atomic physics was primarily described with quantum theory [180, 14], later to be called quantum mechanics. This early quantum theory later ramified into several versions and interpretations of quantum mechanics [170, 15, 91, 203, 207, 60, 13, 54, 55, 88, 219], the most prominent of which—the one originally cooked up by E. Schrödinger, W. Heisenberg, M. Born and P. Jordan [170, 15, 91], and further baked by P. A. M. Dirac and J. von Neumann [46, 12]—deals with state vectors and operators on a Hilbert space, and has been shown repeatedly to describe many-body quantum systems to a tee [90, 161, 56, 158]. It is also used to describe low-order multi-photon processes [45, 80, 2, 204, 205].

However, this quantum description relies on a perturbative treatment of the electron's interaction with light, i.e. an “ n -photon process” is described by the n th-order term of a perturbative expansion of the light-matter interaction Hamiltonian [17, 176]. This perturbative approach is valid for light fields that are not too strong, or not too slowly-varying. As long as the field is weak enough or sufficiently oscillatory, electronic transitions can be viewed as the absorption or emission of discrete amounts of energy quanta of size $\hbar\omega_L$.

Now, for a time after T. H. Maiman's invention of the laser in 1960 [133], coherent light was still sufficiently weak to describe light-matter multi-photon interactions (e.g. bound-bound and bound-free transitions) perturbatively, so all was fine in laserland. Indeed, over the years this perturbative approach became so successful that atomic physicists viewed light-matter interactions almost exclusively in terms of electrons interacting with photons, and completely forgot that they relied on a theory which treats the electromagnetic field strictly classically.

As laser fields became more intense, the new regime of strong-field light-matter inter-

actions pulled the rug from under everyone’s feet. In this regime, new phenomena arose (e.g. HHG and ATI) which could not be understood as the interaction between electrons and discrete quanta of the radiation field. Was this a failure of non-relativistic quantum mechanics? Certainly not, since these strong-field effects do come out of numerical TDSE simulations. Therefore, something was necessarily wrong with the perturbative approach, i.e. the photon picture.

It is now understood that, for a sufficiently strong or slowly-varying laser field, ionization is best described as the result of a tunneling effect [121, 108, 177, 5]. Tunneling occurs because the laser’s electric field bends the Coulombic potential due to the positively charged atomic nucleus. This creates a barrier that allows part of the bound electronic wave function to leak out and become free. The free part of the wave function, a wave packet, subsequently evolves in the laser field. Tunneling ionization, which is central in strong-field processes, cannot be easily formulated within a multiphoton picture; in this regime, the strong and slowly-varying laser field behaves rather classically [169, 79, 21]. Yet, despite its intractability from a quantum perspective, the tunneling regime facilitates a rather intuitive physical picture in terms of electron trajectories [166, 178].

It is fortunate, then, that by the time strong-field phenomena came to the fore, R. P. Feynman previously devised an alternate and equivalent version of quantum mechanics based on trajectories [60]. Trajectories were strictly verboten in the original quantum mechanics laid out by Heisenberg, Schrödinger, and Co [170, 15, 91]. But according to Feynman, an initial state can evolve into a final state by taking a number of possible trajectories, or paths in phase-space. Mathematically, the electron’s evolution is computed by *coherently* summing the probability amplitudes of all possible paths the electron can take from an initial state to a final state. Since there exists a continuum of paths, this summation is actually an integral. These paths need not be classically allowed, and each one has an associated phase given by the classical action, i.e. the integral of the Lagrangian function along the path. It turns out that the main contributions to the path integral usually come from those trajectories that are near the classically allowed ones, while classically forbidden contributions tend to destructively interfere, and contribute little to the evolution of the electron³.

This brings us back to the quasi-classical treatment of strong-field light-matter interactions. As it happens, the reason why Gallagher and Corkum’s two-step model works so well is precisely because classically forbidden trajectories contribute little to the free electron’s time evolution. After tunneling, the evolution of the free wave packet is described by trajectories that are bundled around that of a classical electron moving in a laser field. Even so, this two-step model still couldn’t explain HHG and the high-energy part of the ATI spectrum. To account for these processes, a key ingredient was needed.

Building upon the successes of this quasi-classical approach, it took merely four more years before a more comprehensive model [36] was finally put forth that explained those remaining strong-field effects, and as a bonus it even accounted for another recently dis-

³This is not always the case. As will be shown in Section 2.2, trajectories which are “bundled” around a classically-forbidden one can also significantly contribute to the path integral.

covered one: the correlated emission of two electrons in an intense laser field [64], unfortunately⁴ referred to as *non-sequential double ionization* (NSDI). This new and improved model, due to P. B Corkum and inspired by the work of F. Brunel [22], builds upon the two-step quasi-classical model [38] from 1989. It still treats the free electron as a classical particle and makes use of ionization rates from tunneling theory. In order to account for HATI, HHG, and NSDI, a third step has to be included: the interaction between the free electron and its parent ion.

After tunneling out of the atom, the laser field can drive the free electron back to its parent ion, where the electron can re-scatter elastically or inelastically. In the case of an elastic collision, classical considerations show that the free electron can acquire an energy up to $10U_P$ at the moment it recollides, contributing to the high-energy ATI plateau. If it inelastically scatters from its parent ion, it can eject a second electron from the atom, whose momentum is correlated with that of the original electron. This provides a mechanism for NSDI.

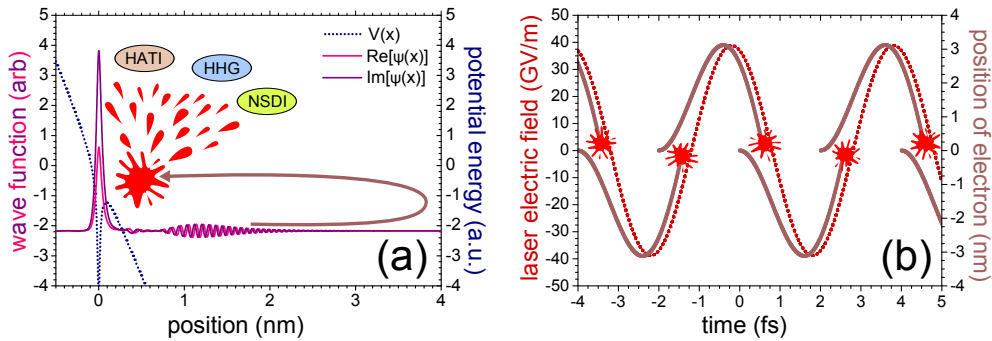


Figure 1: (a) After tunneling through the barrier (located at $x \approx 0.1$ nm) created by the combined potential of the ion and the laser electric field, the laser electric field can drive the electron wave packet (centered at $x \approx 1.2$ nm) back to its parent ion, where it splatters all over the parent ion which can result in HHG, NSDI or HATI. The solid lines depict the real and imaginary parts of the electron's wave function, while the dotted line represents the combined potential created by the ion and the laser field. (b) Due to its periodicity, the laser field drives the recollision process occurs twice per period, and adjacent recollision events are spatially inverted. The dashed line represents a monochromatic driving field $F(t) = F_0 \cos(\omega t)$, while the solid thick line shows the trajectories taken by an electron after tunneling, $x(t) = -\frac{eF_0}{m_e\omega^2} (\cos(\omega t) - \cos(\omega t_0) + \omega(t - t_0) \sin(\omega t_0))$, for various moments of birth t_0 .

Last but not least, the recolliding electron can be captured by its parent ion into a bound state, leading to the release of an energetic photon. In fact, a classical analysis of

⁴The emission of two electrons via recollision is indeed a sequential process, as it arises from a sequence of events: the extraction of a first electron via tunneling, which is then driven back to the parent atom to eject a second electron. Yet, because one of the electrons is kicked out by the other, the two electrons are necessarily correlated. In my humble opinion, this process should have been called *correlated* double ionization (CDI).

this process reveals that the highest possible energy acquired by the recolliding electron in the laser field is $3.17U_P$. Hence, recombination to the ground state should emit a photon with a maximum energy of $W + 3.17U_P$, coinciding with the observed HHG cutoff energy. These events are depicted in Figure 1.

In addition to accounting for the cutoff energy, the three-step model also explains the discrete nature of the HHG spectrum. Because the three steps—ionization, excursion and recombination—occur twice per laser period, the radiation is produced with a periodicity equal to half a laser cycle. In the spectral domain, such a time structure leads to discrete peaks separated by twice the laser frequency. Lastly, the three-step model explains why harmonics are not produced with a circularly polarized laser field: In this case, the electron trajectories do not revisit the parent ion, precluding an electron-ion recombination. Indeed, these arguments provided quite an intuitive and compelling explanation for the HHG spectrum.

Although it neglects many quantum-mechanical effects, such as interferences and entanglement of the free electron with the bound electrons, the three-step model introduced a very useful paradigm that guides intuition, and onto which further theoretical work can be built. Indeed, the quasi-classical theory has inspired subsequent quantum-mechanical theories of strong-field processes, such as those developed by M. Lewenstein [123, 124]. Lewenstein’s models are direct quantum-mechanical extensions of the quasi-classical approach. They quantitatively predict ATI and HHG spectra by coherently summing (integrating) the probability amplitudes of different paths launched at various times, and with various probabilities, by the laser field.

While Bohr and Sommerfeld apparently had trajectories in mind as they pioneered the original quantum theory, these trajectories don’t appear as explicitly in the quantum mechanics of Heisenberg and Schrödinger. Nevertheless, as suggested by the aforementioned developments in laser science, trajectories are crucial to our understanding of strong-field light-matter interactions and should not be ignored. A significant part of this thesis aims to illustrate the power of these trajectories.

Transcending Harmonic Generation

Of the strong-field processes listed in the previous section, the one that results in the emission of energetic electromagnetic radiation is the recombination of the laser-driven electron with its parent ion, resulting in HHG. Since taking center stage as the method of choice for generating coherent table-top XUV radiation, HHG has turned into a field of research on its own, with continual attempts to increase XUV photon energies and yields by exploiting the $U_P \propto \lambda^2$ scaling law [188, 34, 186, 66], and using creativity in phase-matching [77, 211, 153, 9] the generation and propagation of harmonics. As a matter of fact, the HHG process has been considered in a variety of other scenarios, some departing wildly from the three-step model.

Perhaps the nearest cousin to the three-step model is *coherent wake emission* (CWE) [155]. CWE occurs when an intense light field reflects upon an over-dense plasma with

a high density gradient. As the light field interacts with the medium, it periodically extracts attosecond electron bunches out of the material, and then drives them back inside, exciting plasma oscillations within the material periodically with the light field oscillations, thus generating harmonic radiation with photon energies up to the plasma frequency. This process has been investigated numerically [76, 156] and experimentally [192, 50], and through an autocorrelation experiment based on two-photon ionization [144], CWE harmonics have been shown to consist of a train of attosecond pulses.

By extending the CWE experiment to relativistic light intensities, harmonic generation enters a completely new regime described by the *relativistically oscillating mirror* (ROM) model [23, 127]. Harmonics generated by ROM originate from entirely different physics, which cannot be described by a three-step recollision model. Just as for CWE, ROM requires an intense light field that impinges upon a material with a high plasma density gradient. However, instead of relying on plasma oscillations in the material, the “ROM harmonics” are generated by the surface of the material, which is driven back and forth by the ultra-intense light field to relativistic velocities. Since the relativistic driving field is still periodic, any events driven by the laser field occur periodically. As electrons at the surface are accelerated and decelerated by the periodic laser field, they radiate integer multiples of the fundamental driving frequency (harmonics). These harmonics are contained in the field that is reflected by the relativistically-driven material. Since this process is largely independent of the nature of the generating material, the properties of ROM harmonics mainly scale with the parameters of the incident light pulse [81, 7]⁵, thus enabling the generation of harmonics of thousands of orders, well into the keV range. According to simulations [152, 162, 198], ROM harmonics can lead to an attosecond pulse train and even an isolated attosecond pulse [164]. However, ongoing experimental research [49, 193, 50] has yet to unequivocally confirm these predictions.

Another approach to harmonic generation, which resembles the three-step model but otherwise seems to come from another planet, is the generation of a train of gamma-ray bursts from the periodic creation and annihilation of positron-electron pairs from the vacuum. In this proposed method [44], which actually takes advantage of the Schwinger limit, a super-intense laser pulse extracts a positron-electron pair from the vacuum near the peak of each laser half-cycle. Due to their opposite charges, the particles are accelerated by the relativistic light field in opposite directions, and are driven back together—to mutual annihilation—at every half-cycle of the laser field, thus generating a train of sub-laser-cycle gamma-ray bursts.

These examples illustrate the Pandora’s box of ideas that arose since the beginnings of HHG, to convert existing radiation to higher photon energies in a coherent manner. Although it is certainly permitted and encouraged to dream, in this thesis I will constrain myself to reality, and discuss processes involving XUV radiation generated within the parameters of the original three-step model, i.e. HHG in gaseous media using moderately

⁵This is the case until the Schwinger limit [92, 173, 24] is reached, where positron-electron pairs are generated from the vacuum by the light pulse, thus putting a limit on the available power. But who knows, perhaps even this seemingly hard limit can be softened by e.g. squeezing the vacuum...

intense ($\sim 10^{14}\text{W}/\text{cm}^2$) infrared light fields.

From the established theoretical understanding of the HHG mechanism as a three-step process, it was soon speculated [89, 154, 6] that this XUV radiation might exhibit temporal structure on the sub-femtosecond time scale. In theory, due to the highly nonlinear tunneling ionization probability with respect to laser field strength [5], free electron trajectories are launched with greatest probability near the peaks of each laser half-cycle, thereby creating a train of very short bursts of XUV radiation consisting of attosecond pulses separated in time by half a laser period.

Of course, to unequivocally claim that attosecond pulses are produced in the laboratory, it is not sufficient to simply measure an HHG spectrum and point to the three-step recollision model. An HHG spectrum *might* correspond to a train of pulses in the time domain, but only if there is a well-defined phase relationship between the discrete harmonic peaks. In other words, the harmonic spectrum has to be *coherent*.

Thus, the generation of attosecond pulses was merely speculation at the time because a number of effects could conceivably make the harmonics de-cohere after their generation, thereby preventing them from remaining phase-locked. It was not until P. M. Paul *et al.* showed experimentally [147] that there actually does exist a well-defined phase relationship between the harmonics in the far-field—which was soon corroborated by direct autocorrelation measurements of the attosecond pulse train [199, 175, 140]—that the idea of attosecond science took hold.

Chapter 1

Characterizing Attosecond Pulses

Since a harmonic spectrum only *indicates* attosecond time structure, a phase-sensitive measurement of the generated harmonics is required to claim anything about how that radiation looks in the time domain. A discrete spectrum alone does not necessarily correspond to a train of pulses in the time domain. Thus, in order to be of any significant use in attosecond time-resolved experiments, the attosecond temporal structure of the generated high-harmonic radiation has to be known. Moreover, in order to achieve *total* unadulterated attosecond time resolution, additional methods are required to isolate a single attosecond pulse from the generated harmonic spectrum.

In this chapter, I describe the ensemble of experimental and theoretical techniques that are used to measure the temporal structure of the harmonic radiation, with emphasis put on the isolation and characterization of individual attosecond pulses.

1.1 The RABITT Technique

Immediately after the milestone experiment [147] by Paul *et al.* in 2001, H. G. Muller devised a measurement technique [139] called *Reconstruction of Attosecond Beating by Interference of Two-photon Transitions* (RABITT), to measure the phases of the harmonics. In order to perform the RABITT measurement, the laser field is heavily attenuated and sent, together with the temporally synchronized harmonic field (Figure 1.1-b), onto a second target. The XUV harmonics are responsible for ionizing the second target, while the role of the weak NIR field is to dress the single-photon ionization. Without the laser field, each harmonic of order $2m + 1$ generates a peak in the photoelectron spectrum located at an energy $\varepsilon_{\text{odd}} = (2m + 1)\hbar\omega_L - W$. The role of the dressing NIR field is to add a set of even photoelectron peaks at energies $\varepsilon_{\text{even}} = 2m\hbar\omega_L - W$. These even photoelectron peaks are the result of a constructive interference between two two-photon processes¹.

An even photoelectron peak, say of order $2m$, can be the result of (i) ionization by the $(2m - 1)$ th harmonic followed by the absorption of a NIR laser quantum $\hbar\omega_L$, or (ii)

¹Ironically, RABITT, the first method used to characterize HHG, relies on the perturbative multiphoton picture, which is useful here since the laser field is weak.

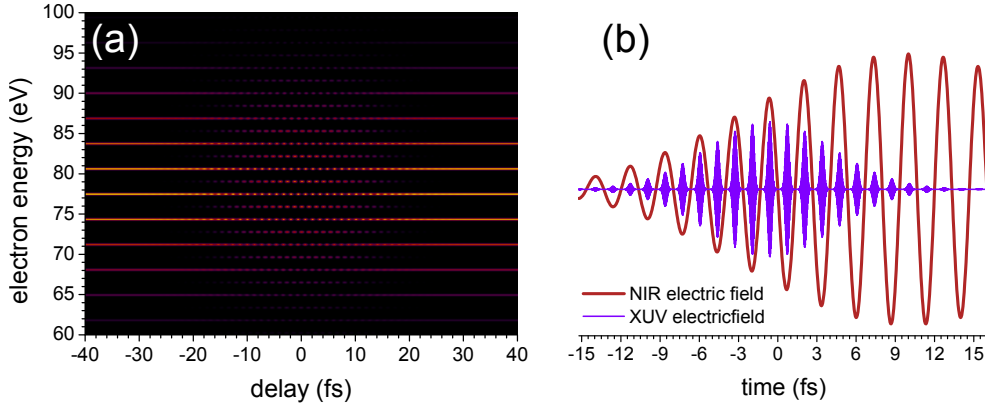


Figure 1.1: The RABITT measurement (a) shows the appearance of discrete peaks between the odd harmonics when the dressing laser field overlaps with the attosecond pulse train (b). These “even” peaks result from the interference between two biphoton processes, which can be destructive or constructive depending on the delay between the XUV and NIR fields.

ionization by the $(2m + 1)$ th harmonic followed by the emission of a quantum of energy $\hbar\omega_L$ back into the NIR field. In the absence of any “which way” information [136, 174] between these two processes, the even photoelectron peaks result from the interference between those two quantum paths.

In the region where the XUV and NIR fields overlap, the intensities of photoelectron peaks change periodically as the harmonics are time-delayed with respect to the dressing laser field, as shown in Figure 1.1-a. By recording the oscillations of the even photoelectron peaks as a function of the XUV-NIR delay, it is possible to extract relative phases between the harmonics. The introduction of this methodology, i.e. the characterization of harmonics via laser-dressed photoelectron spectrograms, established a blueprint for future characterization techniques in attosecond metrology.

Of course, RABITT does not provide the *complete* characterization of the harmonics, because it associates only a single phase to each harmonic. In reality, the harmonic peaks are of finite width because the attosecond pulse train is of finite duration. As a result, for each harmonic, there is a frequency-dependent spectral phase $\tilde{\varphi}_{2m+1}(\omega)$ over the bandwidth of the $(2m + 1)$ th harmonic. This spectral phase is not resolved by the RABITT technique.

Basically, the working assumption for RABITT is that the attosecond pulses in the train are all identical apart from their intensities and their carrier-envelope phases. Under this assumption, there is a simple relation between the attosecond pulse train and the harmonic spectrum: the overall spectral profile of the harmonic *comb* is the Fourier representation of one attosecond pulse in the *train*; conversely, the overall temporal profile of the attosecond pulse train is given by the spectral amplitude and phase of a single harmonic peak. In mathematical terms, if the electric field of an attosecond pulse train, composed of $N + 1$

pulses, is given by

$$E(t) = F(t) \sum_{k=-N/2}^{N/2} (-1)^k f(t - k\pi/\omega_L), \quad (1.1)$$

then the associated harmonic comb is well described by

$$\tilde{E}(\omega) = \tilde{f}(\omega) \sum_{\kappa=-M/2}^{M/2} \tilde{F}(\omega - (2\kappa + 1)\omega_L), \quad (1.2)$$

where $M = \omega_{\max}/\omega_L$, so that the comb covers the highest possible frequency ω_{\max} occupied by a single pulse in the train. The sign change of the electric field between consecutive attosecond bursts² is explicitly written out in (1.1). $F(t)$ is the temporal envelope of the pulse train while $f(t)$ is the temporal profile of a single attosecond pulse in the train, and the train contains $N + 1$ pulses; the tilde notation denotes the Fourier transform, i.e. $\tilde{A}(y) = \mathcal{F}[A(x)](y)$.

Consequently, the bandwidth of the attosecond pulse, which is also the bandwidth of the comb, together with the spacing of the harmonics ($2\omega_L$), set the total number of harmonics in the comb. From (1.1) and (1.2), it is clear that RABITT cannot detect any variations between pulses in the train, nor can it provide the relative phases and intensities between the pulses. Nevertheless, the information provided by RABITT has proven sufficient in many groundbreaking applications [135, 98, 131, 167, 160, 53, 99, 16], and continues to be immensely valuable to attosecond science. To this day, RABITT remains the state-of-the-art for characterizing attosecond pulse trains.

Following the discovery of phase-locked harmonics, attosecond science branched off in two directions: one led to experiments with attosecond pulse trains while the other sought to reduce the train to a single, isolated pulse in order to truly confine the attosecond probe in time³. This latter approach to attosecond science, which gave rise to a series of scientific breakthroughs [94, 48, 10, 110, 83, 168, 200, 85, 86, 172], will be the focus of this thesis.

1.2 Gating the Attosecond Pulse Train

Isolating a single attosecond pulse from the train [94] has proven a formidable challenge, and has required the development of new technologies which eventually became fields of research in their own right. The most prominent approaches to this end involve gating the attosecond pulse train in the time domain [39] or in the frequency domain [31].

²The sign change of the electric field, or equivalently a phase drift of π , between consecutive attosecond bursts is a consequence of the spatial inversion of recollision events between adjacent half-cycles of the laser field. This is why odd and not even harmonics of the driving field are observed for gas-phase media.

³Much in the same way as brushing and flossing your teeth serve two different yet complementary purposes!

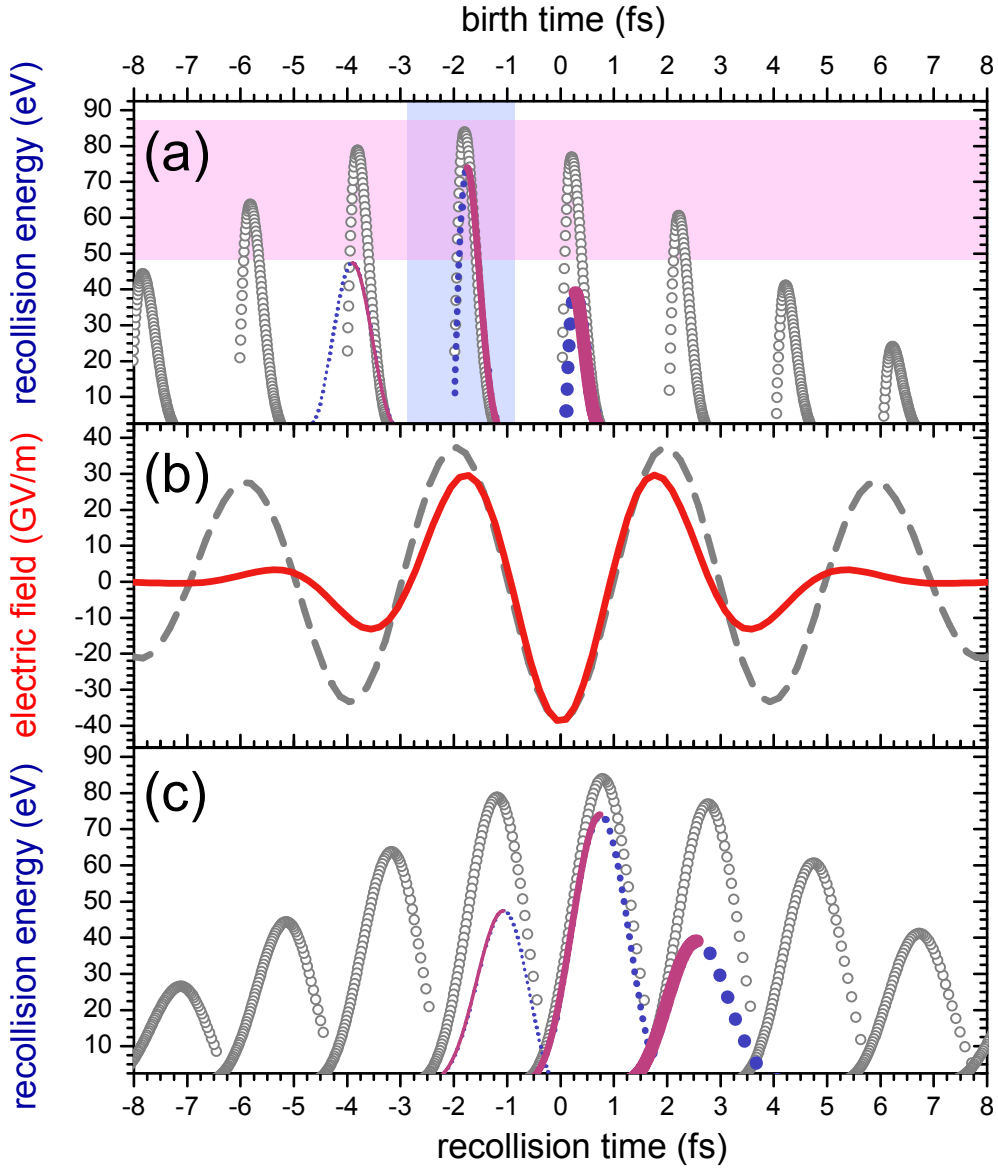


Figure 1.2: Panel (b) plots the electric fields of a 4 fs laser pulse (solid line) and a 12 fs laser pulse (dashed line). In panels (a) and (c), recollision energies are plotted as a function of birth time and recollision time respectively. The lines in panels (a) and (c) represent the recollision energies generated by a 4 fs laser pulse, for the short (solid lines) and long (dotted lines) trajectories. The thickness of the lines indicates the probability of the trajectory to occur (thicker lines indicate larger probability). The hollow circles represent recollision energies for the 12 fs laser pulse. The shaded areas illustrate two possible ways to isolate a single attosecond pulse: via spectral filetering (horizontal shade) or temporal gating (vertical shade).

Figure 1.2 shows plots of recollision energies—the electron’s energy at the moment of recollision—evaluated from purely classical considerations, as a function of the time of birth (panel (a)) and time of recollision (panel (c)). It has been shown [67, 209], through the time-frequency analysis of the time-dependent recombination dipole moment, that these classical recollision energies represent a simplified but accurate picture of the harmonic generation process. The classical analysis presented here was performed assuming both long (12 fs) and short (4 fs) driving laser pulses, centered at a wavelength of $1.2\ \mu\text{m}$, plotted in Figure 1.2-b as dashed and solid lines respectively. The recollision energies pertaining to the long driving pulse are plotted with hollow circles, while those for the short driving pulse are shown as full dots.

Comparing panels (a) and (c), the first thing to note here is that the most energetic electrons are released near the peak of oscillation cycles of the driving field, and recollide slightly more than half an optical cycle later. Moreover, as shown in panel (c), for each half-cycle contribution there are two recollision events that occur at different moments in time but with the same energy. These two events correspond to two different free electron trajectories, a “long” one and a “short” one [123], which are launched by the driving field at different moments of birth, as shown in panel (a). As their names suggest, the long trajectory (represented by the dotted lines) starts earlier and ends later, while the short trajectory (solid lines in panels (a) and (c)) begins later and ends earlier.

Electrons following these two trajectories generate two temporally distinct bursts of radiation when they recombine [188], which hinders the temporal “cleanliness” of the emitted radiation. However, it is possible to suppress one of these contributions by employing an appropriate focusing geometry [69].

There is also a *probability* associated to the half-cycle contributions, which is evidenced in Figure 1.2-a and 1.2-c by the thickness of the recollision curves for the 4 fs driving pulse. Although to some extent the spread of the recolliding electron wave packet during its excursion as a free particle affects the recombination cross-section⁴, the probability of a recollision event is largely determined by the strength of the half-cycle that launches the free electron trajectories. The probability of the different half-cycle contributions is represented in Figure 1.2-a and 1.2-b with the thickness of the recollision energy curves for the 4 fs driving pulse.

In order to achieve an *isolated* attosecond pulse, the biggest problem is limiting the recollision process, and thus the HHG contribution, to all but one half-cycle of the driving field. As suggested by the shaded areas in Figure 1.2-a, gating the HHG spectrum in time or in energy are two possible methods that can yield an isolated attosecond pulse. The spectral filter (horizontal shade) lends itself well to harmonic radiation generated by a very short driving pulse. On the other hand the temporal filter (vertical shade) appears to be more useful for longer pulses, although it also has its shortcomings, as we will see in the following section.

⁴This already makes the long trajectories contribute less to the harmonic emission, which is yet another reason to eliminate them.

1.2.1 Temporal Gating of the Attosecond Pulse Train

Time-domain gating is achieved by tailoring the temporal behavior of the electric field of the driving laser pulse. One type of temporal gating capable of generating isolated attosecond pulses has been proposed and demonstrated by S. Leone and co-workers [151, 1]. They have shown that if the intensity of the driving laser pulse is simply cranked up, only the first few half-cycles at the leading edge of the pulse yield attosecond bursts because the medium is heavily ionized by the subsequent half-cycles. The resulting plasma significantly inhibits further recollision events, and ruins the propagation of any attosecond XUV bursts that do manage to come out.

Temporal gating can also be achieved by taking advantage of another degree of freedom of the driving field: its polarization. Recalling that harmonics can only be generated by a linearly polarized driving field—since an elliptically polarized field doesn’t drive the electron back to its parent ion [123]—then, restricting the driving field’s linear polarization to a single half-cycle should create an isolated attosecond burst. This is the strategy used in the so-called *polarization gating* (PG) technique [39, 179]. Specifically, if the driving field’s polarization state changes as a function of time, and exploiting ,

To achieve PG, an elegant scheme [189] has been presented, where a femtosecond pulse is passed through two quarter-wave plates resulting in a sequence of two time-delayed laser pulses with opposite circular polarizations. If the two pulses are sufficiently separated in time, then a single significant linearly-polarized half-cycle will appear right in the region where they temporally overlap. This linear half-cycle is responsible for driving a single recollision event, initiated by the previous half-cycle. The PG technique was used in 2006 by Sansone *et al.* [168] to generate an isolated attosecond pulse with a record-breaking duration of 130 as, showcasing the PG technique as a valuable tool for attosecond metrology.

Unfortunately, the PG technique has a couple of disadvantages. First, the ionizing and driving half-cycles are necessarily weak because they must only occur in the overlapping region between the two pulses, where the pulses are weak. This limits the cutoff energy and the intensity of the isolated attosecond burst. Second, if one tries to fix this problem by cranking up the intensity of both laser pulses, then the medium might be completely ionized by the first pulse before the arrival of the linearly-polarized half-cycle, further limiting the efficiency of HHG⁵.

To alleviate these shortcomings, a bit of creativity was required. It was shown [53] that mixing the driving field with its second harmonic—yes, the old-fashioned second harmonic using the second-order $\chi^{(2)}$ susceptibility—extends the periodicity of HHG to a full laser cycle, resulting in a harmonic spectrum with peaks separated by $\hbar\omega_L$. By suitably time delaying the second harmonic pulse with respect to the fundamental pulse, recollision events can be made to occur only once per laser cycle.

⁵As an aside, the term HHG should be taken with a grain of salt within the context of an isolated attosecond pulse because such a spectrum is not made of discrete harmonic peaks. Rather, it is completely continuous! Nevertheless, the same physics are at play, so it is customary to refer to a continuous XUV spectrum, produced by a single recollision event, as a “harmonic” spectrum.

This effect presents an obvious boon to the PG technique. Essentially, mixing the two (counter) circularly polarized laser pulses with their second harmonic allows for a greater temporal overlap between the two pulses while preserving a single linearly polarized driving half-cycle. This means that the driving and ionization half-cycles can be made much more intense. This has been used in an extension of PG, dubbed *Double Optical Gating* (DOG) [137], to drastically increase the efficiency and energy of the recolliding electron.

1.2.2 Spectral Filtering of the Attosecond Pulse Train

The isolation of an attosecond pulse from the train can also be achieved in the frequency domain. In this case, one attempts to generate an HHG spectrum that contains a continuous (unmodulated) portion which can be singled out from the rest of the HHG spectrum with an appropriate spectral filter [208]. The next challenge, then, is to generate an HHG spectrum that contains such a continuous part that is broad enough to support an attosecond pulse.

Thanks to numerous advances in ultrafast photonics [19]—notably, chirped pulse amplification [183, 163], the development of spectral broadening in hollow-core fibers [142] together with the invention of chirped multi-layer mirrors [184, 182]—the duration of phase-stable [190, 159] laser pulses has been progressively approaching the single optical cycle [143, 10, 29, 84]. Such a short driving pulse exhibits half-cycles that vary wildly in strength over the duration of the pulse. These half-cycles generate harmonic radiation at very distinct energies [31, 85], which can be easily filtered in the spectral domain.

The electric field of an ultrashort pulse is described within the carrier and envelope formalism [18] as

$$F(t) = F_0(t) \cos(\omega_L t + \varphi(t) + \varphi_0), \quad (1.3)$$

where $F_0(t)$ represents the envelope of the pulse, and the carrier wave is represented by the cosine function, oscillating at a nominal frequency ω_L and with $\varphi(t)$ containing the higher-order temporal dependence of the phase (the chirp). There is also an overall phase offset φ_0 , referred to as the *carrier-envelope phase* (CEP). For a long⁶ laser pulse, the CEP just shifts the carrier with respect to the envelope, and hardly changes the HHG spectrum. However, it was realized early on that when the envelope of the pulse is very short—comparable to the period of the carrier—the CEP influences the relative sizes of the few half-cycles within the envelope, which greatly impacts the HHG spectrum, particularly near the cutoff [191, 10].

In fact, for a given CEP, there normally exists a single half-cycle that can produce harmonic radiation with the highest possible energies, extending well beyond the $W + 3.17U_P$ cutoff⁷. Since the generation of those spectral components is localized in time,

⁶A “long” laser pulse is one that encloses several oscillation cycles of the carrier wave. For a NIR carrier, a long laser pulse would have a duration $\gtrsim 20$ fs.

⁷Recall that the $W + 3.17U_P$ law arises from purely classical considerations, i.e. classical mechanics *forbids* an electron to recollide with an energy greater than $3.17U_P$. However, such stark classical restrictions

they form a continuum. That single most energetic and temporally localized burst can be singled out by applying an appropriate spectral filter to the HHG spectrum. Prior to being filtered, that attosecond burst originally possesses lower-energy spectral components that overlap with those originating from other half-cycles. Therefore, part of the original attosecond burst, i.e. its less energetic components, are removed by the spectral filter making it slightly longer in time as a result of spectral filtering. Incidentally, this is why attosecond pulses in a train can reach shorter durations than isolated ones [114].

It was originally thought that the best way to obtain an isolated attosecond pulse through spectral filtering was to set the CEP to $\varphi_0 = 0$, which corresponds to a *cosine* pulse [209, 110], such as the ones shown in Figure 1.2-b. This is because the cosine pulse contains the strongest possible half-cycle of any CEP setting, which sits right at the center of the pulse. Moreover, the contrast between that strong central half-cycle and its neighboring ones is also the largest of any CEP setting. Thus, a cosine pulse produces HHG radiation at the highest possible energies, and which can most easily be distinguished from the rest of the HHG spectrum, resulting in the broadest possible continuous XUV bandwidth. Figure 1.2 shows that the central half-cycle drives the electron to recollision with much higher energy than the other half-cycles.

However, let's not forget that it takes two consecutive half-cycles to create a recollision event: an *ionizing* half-cycle to release the electron, and a *driving* half-cycle to make the free electron return to its parent ion. Now, for a cosine pulse, the most energetic recollision event, which is driven by the strongest half-cycle, is launched by a weak ionizing half-cycle. So although this recollision event does indeed produce the highest possible XUV energies, the corresponding burst of attosecond XUV radiation is rather weak in intensity.

It was later found [85] that a broad XUV continuum can be achieved when the driving laser pulse is so short that at most two half-cycles are able to produce recollision events with significant probability. In this case, most CEP settings open up a sufficiently broad and continuous⁸ spectral region. For the spectral mirror used in that experiment, it was found that a CEP of $\sim 70^\circ$ was optimal for producing the broadest and most intense continuum, leading to an ~ 80 as isolated pulse [85], which made it into the Guinness Book of World Records in 2008. Thanks to ongoing advancements in the technology of XUV multilayer mirrors [95], current XUV mirrors can now be tailored to produce isolated attosecond pulses with a particular central energy and chirp.

Now, for a given an ultrashort driving pulse, the broadest harmonic continuum does not necessarily originate from the most energetic recollision. It can be produced by a

are softened because the electron is a quantum-mechanical particle, and can assume classically forbidden trajectories. So instead of a sharp cutoff edge, as predicted by classical mechanics, the HHG spectrum actually rolls off exponentially for energies $\gtrsim W + 3.17U_P$

⁸By referring to a spectrum as “sufficiently continuous”, I mean that the spectral components need to be generated around the same time, i.e. within the same half-cycle. If that's not the case, then interference will appear, resulting in a modulation of that spectrum. Yet, if this spectral modulation is weak enough, then one might describe the spectrum as “approximately” or “sufficiently” continuous. This is equivalent to saying that most of the spectrum is made up of components originating around the same time value, with small contributions (later referred to as satellite pulses) originating at large time values.

recollision event launched by a sequence of equally strong ionizing and driving half-cycles, ensuring a high probability of ionization as well as a high recollision energy. As a case in point, the record 80 as pulses from 2008 were obtained, after spectral filtering, using a driving field which had two comparably intense consecutive half-cycles used for ionization and recollision.

Of course, under these conditions the harmonic continuum can overlap with spectral components from an adjacent half-cycle. Therefore, the filtered HHG spectrum is not quite continuous, but exhibits a small amount of spectral modulation with a fringe spacing of $2\hbar\omega_L$, which is the inverse of half a laser period. In the time domain, this means that the filtered XUV radiation consists of two attosecond pulses separated by half a laser period. Since the spectral filtering is optimized for one of the half-cycle contributions, a *main* pulse generated by the most intense half-cycle is followed or preceded by a smaller *satellite* pulse coming from the next strongest half-cycle. It was shown [85] that, for a ~ 3 fs driving laser pulse, over 90% of the generated XUV energy is concentrated in the main pulse over a broad range of CEP settings, $30^\circ \lesssim \varphi_0 \lesssim 90^\circ$.

In principle one should be able to directly diagnose the amount of power in the satellite pulse from the contrast of the spectral modulation, and then optimize the CEP to concentrate energy in the main pulse. However, there are a number of practical reasons [70] that preclude an accurate estimation of the intensity of the satellite pulse from the fringe contrast. The fringe pattern is highly sensitive to the parameters of the laser pulse, and can be easily smeared out by variations in the laser CEP, a non-uniform XUV beam profile, laser timing jitter, and generally any variations in the XUV pulse parameters. These effects are discussed in more detail in section 1.7.

Above and beyond issues of attosecond pulse contrast, the ability to generate an isolated attosecond pulse requires the concomitant development of new techniques to fully characterize its temporal structure. But what about RABITT? If it can fully characterize attosecond pulses in a train, is there any reason why it can't also be used to characterize an *isolated* attosecond pulse?

1.3 The Attosecond Streaking Measurement

If the RABITT method, described in the previous section, is already able to fully characterize the temporal structure of an isolated attosecond pulse in a train, then why can't it also be used to characterize an isolated attosecond pulse? After all, the attosecond pulse train occupies the same energy and bandwidth as the isolated attosecond pulse. So why bother with a new pulse characterization scheme, can't we just rely on the good ol' RABITT to characterize an isolated attosecond pulse? Well, fortunately for me⁹, it turns out we can't rely on ol' RABITT.

The reason for RABITT's failure is the fact that (i) it requires a discrete harmonic spectrum in order to assign phases to the harmonics based on the interference pattern between even and odd photoelectron peaks and (ii) it assumes the train to be composed of

⁹Otherwise, most of this thesis would have to be thrown out the window, along with my degree!

identical attosecond pulses. Although a single, isolated attosecond pulse trivially satisfies (ii), it possesses an entirely continuous spectrum, failing to meet the first requirement. For a sequence of two attosecond pulses produced by adjacent half-cycles of the driving field, we can bend over backwards and think of the modulation in the spectrum as discrete harmonics, satisfying the first point (i). However, in this case the two pulses originate from vastly different half-cycles, so the assumption of identical pulses is invalid.

RABITT works when the dressing field is weak, so as to drive only *single*-photon free-free transitions. For RABITT, a weak dressing field is sufficient¹⁰ to induce substantial changes in the photoelectron spectrum, which allows the recovery of the harmonic phases and therefore the temporal characteristics of the attosecond pulses in the train. However, if one performs a RABITT measurement with an isolated attosecond pulse, the resulting laser-dressed photoelectron spectra are pretty much identical for all XUV-NIR delays: they all resemble the undressed photoelectron spectrum and therefore provide little reliable information about the temporal characteristics of the isolated attosecond pulse. A stronger dressing field is needed in order to significantly modify the electron spectrum produced by an isolated attosecond pulse.

Increasing the intensity of the NIR field has the effect of shifting and distorting the photoelectron spectra, recorded as a function of the delay between the XUV and NIR fields. In fact, the resulting spectrogram—a sequence of photoelectron spectra acquired for different XUV-NIR delays—uncannily resembles the field oscillations of a laser pulse, as shown in Figure 1.3-a. In this regime of laser-dressed photoionization, the modification of the photoelectron spectrum by the dressing field is referred to as the *attosecond streaking* effect; its namesake will soon be clear.

In order to explain this very different behavior of the photoelectron spectra when dressed by a stronger NIR field, we recall that the perturbative multi-photon picture is inappropriate for describing light-matter interactions when the electromagnetic field is strong or slowly-varying. In the present context, a “slowly-varying” laser field is one whose half-period is much longer than the duration over which the photoelectron is emitted.

If the attosecond pulse’s duration is much shorter than the half-period of the dressing field, the emitted photoelectron interacts with the dressing field in a manner that is rather classical: its evolution in the dressing field can be described with electron trajectories. In this case, the dressing field is said to be slowly-varying, and a classical description of the light-matter interaction, relying on electron trajectories in a laser field, is more appropriate¹¹.

The next challenge is to find methods to deduce the temporal characteristics of the attosecond pulse from the observed shifts and distortions of the photoelectron spectrum

¹⁰An excessively strong NIR dressing field, used in a RABITT measurement, would drive higher-order multiphoton free-free transitions which would complicate the interferences in the RABITT trace, preventing an accurate harmonic phase retrieval.

¹¹This is to be contrasted with the RABITT measurement, where a *train* of attosecond pulses emits the photoelectron over several half-cycles of the dressing field. In this case, the dressing field is certainly not slowly-varying with respect to the duration of the photoionization, which is why the analysis of RABITT measurements instead relies on the multiphoton picture.

due to the attosecond streaking effect. Although these methods will be explained in detail in the following sections, let's first have a look at their underlying premises.

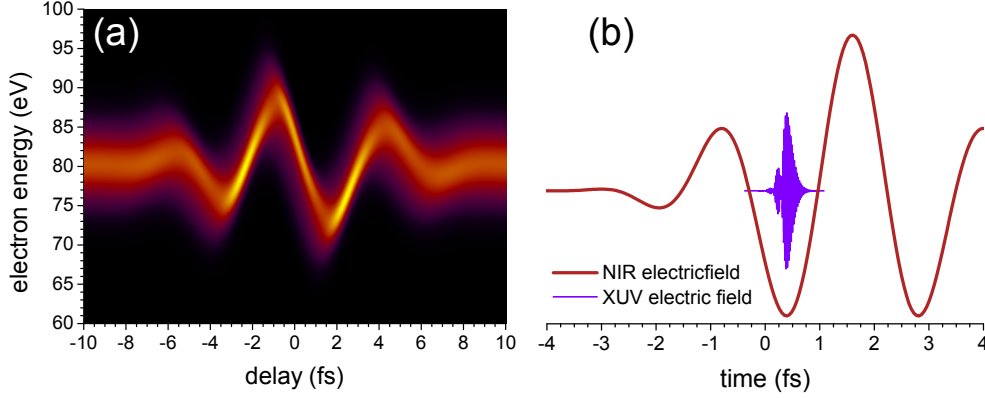


Figure 1.3: The attosecond streaking measurement maps the initial time-momentum distribution of the photoelectron, generated by an isolated attosecond pulse in the presence of a NIR dressing field (b), to a final momentum distribution recorded at the detector. A streaking spectrogram (a), composed of streaked photoelectron spectra for different delays between the XUV and NIR fields (b), contains information about the temporal structure of the attosecond pulse.

As photoionization takes place, electron trajectories are launched at different moments of time over the duration of the attosecond pulse, with probabilities and initial momenta $p(t)$ given, respectively, by the instantaneous intensity and frequency¹² of the attosecond XUV field at the moment of ionization t . Thus, a trajectory's *probability* is mainly related to the *envelope* of the attosecond pulse, while its initial momentum is related to the *chirp* of the attosecond pulse—the rate at which its frequency changes as a function of time. Now, since the dressing NIR field varies during the course of photoionization, electron trajectories launched at different times t will end up with different final momenta $p_s = p(t) - eA_L(t)$ after the laser pulse has ended, where $A_L(t)$ is the vector potential of the NIR field. The laser field then just redistributes the electron's momenta; it performs this role in the time domain, as photoionization takes place over the attosecond pulse's duration.

Specifically, the laser field affects the mapping of the electron's initial momenta $p(t)$, launched at different moments of time t by the attosecond pulse, to final momenta p_s observed at the detector. As a result of this streaking effect, the laser-dressed photoelectron spectrum is generally quite different from the one that is measured when the laser field is turned off, i.e. the *field-free* photoelectron spectrum. Figure 1.4 depicts two cases of the streaking effect: (a) when photoionization occurs at a peak of the laser field's vector

¹²There's a subtlety here. The initial ensemble of the photoelectron's dynamical variables, launched by the attosecond pulse, is given by a time-energy distribution [210]. This basically means that the energy of a photoelectron, released at some moment in time, is not only determined by the attosecond pulse's instantaneous carrier frequency, but also by its energy spread. This will be described in more detail in the following section.

potential (near a zero-crossing of its electric field) and (b) when photoionization occurs at a zero-crossing of the laser field's vector potential (near a peak of its electric field).

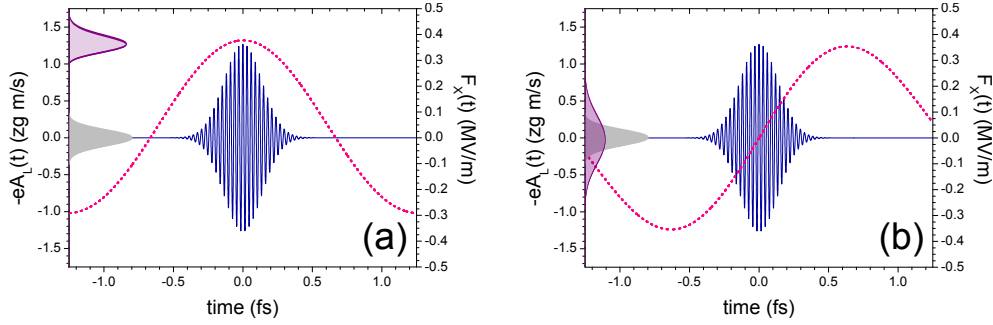


Figure 1.4: During the course of photoionization, the attosecond pulse (solid line) launches photoelectron trajectories which are then boosted by an amount $-eA_L(t)$ (dotted line) due to the NIR streaking field. Because of this time-dependent momentum boost, the laser-dressed photoelectron spectra (shaded areas with solid outlines) are markedly different from the field-free photoelectron spectrum (plain shaded areas). The photoelectron momentum spectra shown on the left side of the graphs are shifted by the electron's (unstreaked) central momentum. In panel (a), photoionization occurs at a peak of the laser field's vector potential, resulting in a shift of the photoelectron spectrum, while in panel (b) the attosecond pulse coincides with a zero-crossing of the NIR vector potential, resulting in the largest change in photoelectron bandwidth. The photoelectron spectra were evaluated by numerically propagating the time-dependent Schrödinger equation in one dimension assuming a soft-core Coulomb potential.

As a first approximation, taking the laser vector potential $A_L(t)$ to be constant over the duration of the attosecond pulse, the momentum shift imparted to each trajectory is then the same (ignoring the initial momentum spread due to the finite bandwidth of the attosecond pulse). So, to “lowest-order”, the attosecond streaking effect manifests itself as an overall shift of the photoelectron's spectrum [110]. This is why an attosecond streaking measurement produces a spectrogram that resembles a laser pulse: the centroids of the laser-dressed photoelectron spectra approximately trace out the vector potential. It can be said that attosecond streaking provides *complete* quantitative information about the laser pulse, including its CEP and its intensity. However, we are concerned here with characterizing the attosecond pulse, not the NIR laser pulse, and a mere shift of the photoelectron spectrum doesn't provide any information about the temporal profile of the attosecond pulse.

Luckily, attosecond streaking engenders more subtle changes to the distribution of photoelectron energies [96] than merely an overall shift. Let's now assume that the attosecond pulse coincides with a maximum of the NIR electric field $F(t) = -\dot{A}(t)$ ($\neq 0$), so that the electric field is approximately constant over the duration of the attosecond pulse, but the vector potential crosses zero and decreases roughly linearly as a function of time. In this case, electron trajectories launched before the zero-crossing of $A(t)$ will therefore be

decelerated while those launched at later times will be accelerated, and this will affect the *breadth* of the photoelectron spectrum, while keeping it centered at the same energy as the field-free spectrum. If the attosecond pulse is not chirped, then it launches an ensemble of trajectories with roughly the same initial momentum, and the vector potential of the streaking field—which crosses zero—doesn’t shift the initial momentum distribution but just spreads it out, resulting in a streaked photoelectron spectrum that is broader than the field-free one.

On the other hand, let’s now consider photoionization by a chirped attosecond pulse, again at the zero-crossing of the laser’s vector potential. For a positively (negatively) chirped attosecond pulse, i.e. one whose instantaneous frequency increases (decreases) with time, trajectories are launched with initial momenta that increase (decrease) as a function of time. Thus, the effect of the streaking field—which decelerates the earlier trajectories and accelerates the later ones—on the final spread of momenta depends on the attosecond pulse’s chirp. For instance, if the attosecond pulse is negatively chirped, then the streaking field decelerates the faster part and accelerates the slower part of the photoelectron, which can result in a narrowed final momentum distribution. While if the attosecond pulse is positively chirped, the faster part of the electron is further accelerated while its slower part is further decelerated, resulting in a broader photoelectron spectrum.

Therefore, the bandwidth of the streaked photoelectron spectrum is both a function of the streaking field at the moment of ionization as well as the attosecond pulse’s chirp. Since the streaking field can be completely determined by looking at the centroids of the laser-dressed spectra, then this laser-induced change in the bandwidth of the photoelectron spectrum actually provides a means to *measure* the attosecond pulse’s chirp.

The following section will provide a more formal (yet classical) treatment of the streaking effects just described, and will showcase a novel method that can be used to extract the chirp of an isolated attosecond pulse from a set of streaked photoelectron spectra.

1.4 A Classical Trajectory Analysis of Streaking for Extracting the Attosecond Chirp

In this section, I derive analytical formulas describing the main effects of attosecond streaking—the shift and broadening of the photoelectron spectrum due to the laser field—by considering classical electron trajectories in a NIR streaking field. Using these analytical expressions, I implement a simple method [71] to evaluate the group-delay dispersion (GDD) of an isolated attosecond pulse from a set of streaked photoelectron spectra. This method is robust and much more efficient than the standard algorithms used for characterizing attosecond pulses. However, it is suited to recover only the lowest orders of the attosecond pulse’s dispersion, by considering the two most important manifestations of the streaking effect: the change in central energy and bandwidth of the photoelectron spectrum due to the streaking field.

Please note that all equations and expressions will henceforth be given in

atomic units ($\hbar = e = m_e = a_0 = 1$) unless otherwise specified. Conversion tables between atomic units and SI units for various quantities and physical constants can be found in Appendix B.2.

Let us first consider an attosecond XUV pulse with electric field $F_X(t)$ given by

$$F_X(t) = |F_X(t)|e^{i(\Omega_X t + \varphi_X(t))}, \quad (1.4a)$$

$$\varphi_X(t) = \frac{1}{2}\beta_1 t^2 + \frac{1}{6}\beta_2 t^3 + \dots, \quad (1.4b)$$

where the spectrum of the attosecond pulse is centered at Ω_X with small variations in frequency due to the higher-order temporal phase $\varphi_X(t)$. The attosecond pulse launches electron trajectories that are parameterized with an initial time t as well as an electron energy $\varepsilon = p^2/2$. Due to the attosecond pulse's finite *bandwidth*, I consider the energy ε as an independent variable, while the independent variable t is a result of the finite *duration* of the attosecond pulse. Thus, the set of trajectories is described by a time-energy distribution with respect to $\{t, \varepsilon\}$.

The final energy ε_S of an electron, launched at some moment t in a continuum permeated by a near-infrared (NIR) laser field, is then

$$\varepsilon_S = \frac{1}{2} \left(\sqrt{2(\varepsilon + \omega_X(t))} - A_L(t) \right)^2 \quad (1.5a)$$

$$\approx \varepsilon - pA_L(t) + \frac{1}{2}A_L^2(t) + \left(1 - \frac{A_L(t)}{p}\right) \omega_X(t), \quad (1.5b)$$

where I define the instantaneous frequency $\omega_X(t) = \dot{\varphi}_X(t)$ due to the chirp of the attosecond pulse, and $A_L(t)$ is the vector potential of the laser field. Since the change in frequency over the temporal profile of the attosecond pulse is much smaller than the central frequency Ω_X , the last term in (1.5b) is comparably small and can be dropped, leading to the simple relation

$$\varepsilon_S \approx \varepsilon - pA_L(t) + A_L^2(t)/2 \quad (1.6)$$

for the shift of the photoelectron spectrum.

It is known [110] that the spectral shift alone is not sufficient to obtain information about the attosecond pulse's chirp because the final energy ε_S is hardly sensitive to the temporal phase $\varphi_X(t)$ of the attosecond pulse. The main manifestation of the attosecond chirp in the streaking measurement is the change in breadth of the streaked photoelectron spectrum. To describe this effect, we can interpret (1.5a) as a mapping of the initial time and energy of an electron trajectory to a final energy (e.g. measured at the detector). To describe the effect of chirp, it is useful to consider small changes $d\varepsilon_S$ in the final energy with respect to small changes in the initial energy $d\varepsilon$ and time dt of the trajectory. The total differential of (1.5a) is then

$$d\varepsilon_S \approx \left(1 - \frac{A_L(t)}{p}\right) \left((\beta_X(t) + pF_L(t)) dt + d\varepsilon \right), \quad (1.7)$$

where I again neglect the small terms containing $\omega_X(t)$. The temporal phase of the attosecond pulse appears in (1.7) as $\beta_X(t) = \ddot{\varphi}_X(t)$, which defines the *chirp* of the attosecond pulse. I have also introduced the electric field of the laser pulse $F_L(t) = -\dot{A}_L(t)$. Thus, the chirp of the attosecond pulse and the electric field of the laser pulse both influence the spread in final energies resulting from the streaking effect.

To proceed further, I propose the following interpretation for the effects of the NIR field on the time-energy distribution of electron trajectories, as described by (1.7). Initial inspection of (1.7) shows that the NIR field imparts an additional energy sweep of $pF_L(t)$ to the photoelectron, resulting in a total chirp $\beta_S(t) = \beta_X(t) + pF_L(t)$. Furthermore, the NIR field re-scales the energy spread by a factor $(1 - A_L(t)/p)$. As a result, both the NIR electric field $F_L(t)$ and the NIR vector potential $A_L(t)$ have a role in modifying the breadth of the photoelectron spectrum.

In order to account for the effects of the streaking field, recall that the attosecond electron wave packet can be viewed as a replica [96] of the attosecond pulse $F_X(t)$. I model this photoelectron replica as

$$\chi(t) = e^{-\frac{1}{2}(t/\tau_X)^2} e^{i(\varepsilon_C t + \frac{1}{2}\beta_X t^2)}, \quad (1.8)$$

where ε_C is the central photoelectron energy. Naturally, since the electron trajectories are launched by the attosecond pulse, the duration τ_X of the electron wave packet [212] should be nearly the same as that of the attosecond pulse; and as $\chi(t)$ is a replica of $F_X(t)$, its chirp β_X is the same as that of the attosecond pulse. For simplicity, assume β_X to be constant and also assume that the attosecond pulse is shorter than any relevant time scale of the NIR field, so that $F_L(t)$ and $A_L(t)$ are evaluated at the central time t_0 of the attosecond pulse.

Now, in order to include the effects of the streaking field, we first consider the shift of the photoelectron spectrum due to $A_L(t_0)$ and the change in bandwidth due to the chirp induced by $F_L(t_0)$. The wave packet's central energy $\varepsilon_C = p_C^2/2$ and chirp β_X are then modified as follows:

$$\varepsilon_C \longrightarrow \varepsilon_S = \varepsilon_C - p_C A_L(t_0) + \frac{1}{2} A_L^2(t_0) \quad (1.9a)$$

$$\beta_X \longrightarrow \beta_S = \beta_X(t) + p_C F_L(t). \quad (1.9b)$$

With these substitutions in mind, the *streaked* photoelectron wave packet can be modeled as

$$\chi_S(t) = e^{-\frac{1}{2}(t/\tau_X)^2} e^{i(\varepsilon_S t + \frac{1}{2}\beta_S t^2)}. \quad (1.10)$$

To obtain an expression for the bandwidth of the streaked photoelectron spectrum, note that the streaked photoelectron spectrum is just a Fourier-transform of $\chi_S(t)$ [111]. Since the streaked wave packet is a Gaussian, the Fourier transform of $\chi_S(t)$ can be carried out analytically, yielding the following expression for the bandwidth of the streaked spectrum:

$$\delta_S(t_0) = \frac{\delta_X}{\eta_X} \left(1 - \frac{A_L(t_0)}{p_C} \right) \sqrt{\left(\eta_X^{(0)} \right)^2 + \left(\delta_X^2 \gamma_S(t_0) \right)^2}, \quad (1.11a)$$

$$\gamma_S(t_0) = \gamma_X + \left(\frac{\eta_X}{\delta_X^2} \right)^2 p_C F_L(t_0), \quad (1.11b)$$

where δ_X and γ_X represent the bandwidth and group-delay dispersion (GDD)—defined as the second derivative of the spectral phase—of the attosecond pulse. The quantity $\eta_X = \sqrt{\left(\eta_X^{(0)} \right)^2 + \left(\delta_X^2 \gamma_X \right)^2}$ is the attosecond pulse's time-bandwidth product, with a Fourier-limited time-bandwidth product $\eta_X^{(0)}$ ($\eta_X^{(0)} = 1/2$ for a Gaussian spectrum). The quantities τ_X , δ_X and $\delta_S(t_0)$ are all taken as standard deviations of their respective distributions. According to (1.11), γ_X determines the width $\delta_S(t_0)$ of the streaked spectrum as a function of t_0 . Provided that the characteristics of the field-free spectrum (Ω_X , δ_X and $\eta_X^{(0)}$) as well as those of the laser field ($A_L(t)$ and $F_L(t)$) are known, γ_X remains the only free parameter.

In writing (1.11), I also explicitly included the energy re-scaling pre-factor $(1 - A_L(t_0)/p_C)$. Similar but less general expressions for the streaked photoelectron bandwidth were previously derived in [96, 70] from the semi-classical expression for streaking [111]. These expressions consider photoionization at the zero-crossing of the vector potential, $A_L(t_0) = 0$, where there is no spectral shift but only a change in spectral bandwidth due to the NIR field. These expressions therefore do not contain the bandwidth re-scaling factor $(1 - A_L(t_0)/p_C)$, which is needed to accurately represent the bandwidth of the streaked spectra at arbitrary delay times t_0 , when the NIR field simultaneously shifts the photoelectron spectrum and changes its bandwidth.

Although (1.11) was deduced assuming a Gaussian wave packet, it actually applies to more general pulse shapes owing to the fact that the relation $\eta_X^2 = \left(\eta_X^{(0)} \right)^2 + \delta_X^4 \gamma_X^2$ holds for arbitrary spectra with a constant GDD (see Appendix B.3). This will be further supported by numerical examples later in this section.

As the treatment of streaking presented here relies on several assumptions and approximations, the accuracy of the formulas (1.11) and (1.11b) needs to be examined. For one, the assumption that the NIR vector potential and electric field are constant over the duration of the XUV pulse, as well as the use of the central momentum p_C in (1.9a) and (1.9b) to account for the streaking effect, would appear to restrict the parameter space in which (1.11) is able accurately describe the bandwidth of the streaked spectrum. Moreover, the derivation of (1.11) relies on the particular interpretation I gave above for the differential (1.7). This interpretation ignores several terms (i.e. those containing $\omega(t)/\varepsilon$) and therefore its validity needs to be tested.

Figure 1.5-a shows a set of streaked photoelectron spectra evaluated from the time-dependent Schrödinger equation (TDSE), numerically propagated using a split-step FFT scheme. The Hamiltonian is that of a single electron in one dimension, assuming a soft-core potential with an ionization energy $W \approx 59$ eV. The streaked spectra are evaluated for

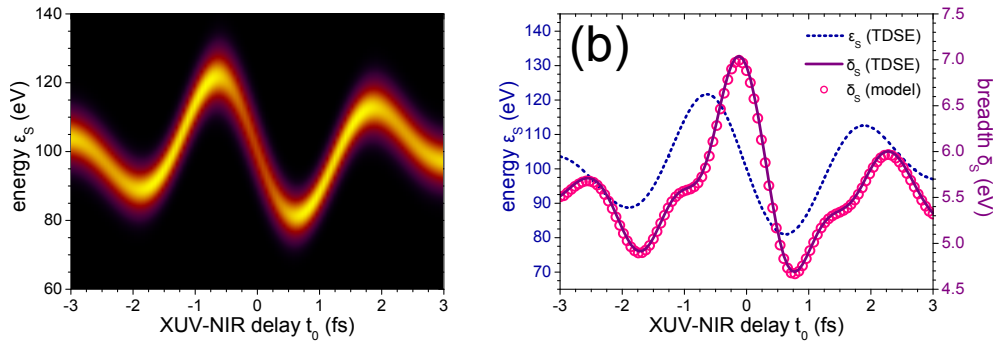


Figure 1.5: Panel (a) shows a set of streaked photoelectron spectra evaluated numerically by solving the time-dependent Schrödinger equation, while panel (b) displays the centroids (dashed line) and standard deviations (solid) of the streaked spectra evaluated as a function of the XUV-NIR delay. The hollow circles represent the standard deviations evaluated according to (1.11).

different delays between the XUV and NIR fields, i.e. the arrival time t_0 of the attosecond pulse. The attosecond XUV pulse has a Gaussian spectrum with a FWHM bandwidth of ~ 12.6 eV, centered at 160 eV, and a GDD of ~ -987 as², yielding a full-width-at-half-maximum (FWHM) duration of 150 as. The streaking field is a NIR laser pulse centered at a wavelength of 800 nm with a 3 fs FWHM duration and a peak intensity of 10 TW/cm².

Although the spectra are shifted in a manner that resembles the NIR field's vector potential, as shown in Figure 1.5-b by the dashed line, the solid line showing their breadths δ_s resembles neither $A_L(t)$ nor the laser's electric field $F_L(t)$. Rather, it contains a signature of the attosecond pulse's spectral parameters γ and δ . The hollow circles in Figure 1.5-b represent the breadths evaluated from equation (1.11).

Given this excellent agreement between the TDSE results and the model I presented above, I will now show that equation (1.11) can be used as a basis for a method to directly extract the attosecond chirp from a set of streaked spectra. Since the method doesn't energy-resolve the attosecond pulse's GDD, it does not provide a complete reconstruction of the pulse. As such, I call this method **inComplete Reconstruction of Attosecond Pulses** (iCrap). iCrap is surprisingly simple.

Equation (1.11) serves as the basis for a method to extract the attosecond chirp from a streaking measurement. This procedure is very straightforward: I first evaluate the first moments (ϵ_s) of the streaked spectra to obtain the laser field's vector potential $A_L(t)$, which in turn gives the laser's electric field $F_L(t)$. I also compute a curve $\delta_s^{(M)}(t_0)$ of standard deviations of the measured streaked spectra as a function of the XUV-NIR delay t_0 . Finally, I find the attosecond chirp γ_X —the only free parameter in (1.11)—which minimizes the discrepancy between the widths $\delta_s^{(M)}(t_0)$ obtained from the set of streaked spectra and

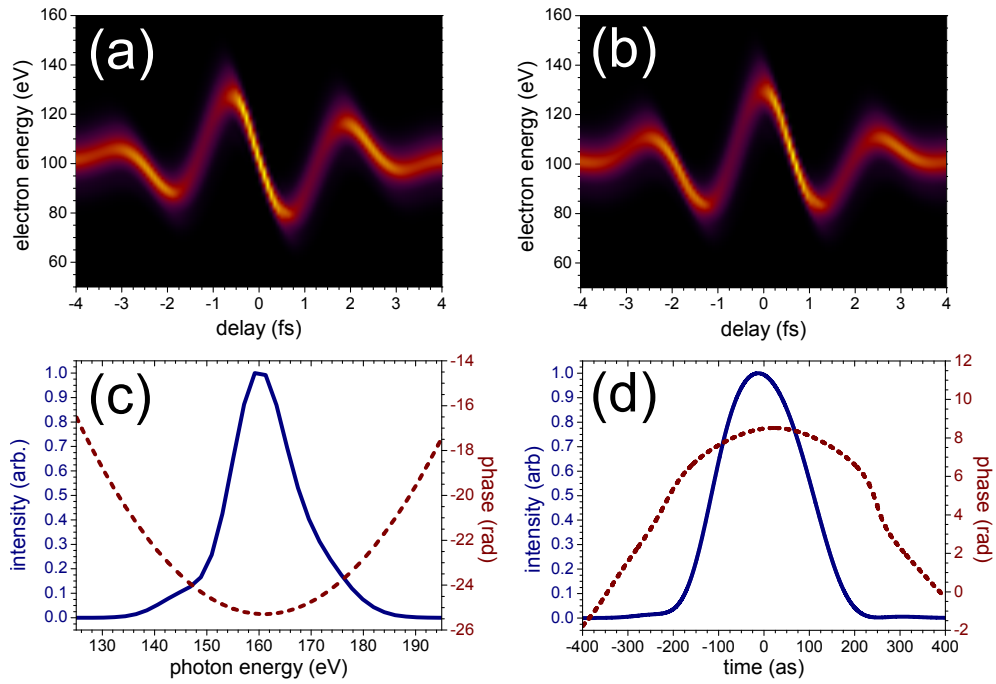


Figure 1.6: Panels (a) and (b) show sets of 101 streaked photoelectron spectra evaluated by solving the TDSE, using streaking fields with $\phi_0 = 0$ and $\phi_0 = \pi/2$, respectively. Panel (c) shows the attosecond pulse's spectrum (solid line) and phase (dotted line), while panel (d) displays its temporal intensity profile (solid line) and temporal phase (dotted line).

those given by the model (1.11). To compare these two, we can define a figure of merit

$$M = \frac{\sum_j \left(\delta_S(t_j) - \delta_S^{(M)}(t_j) \right)^2}{\sum_j \left(\delta_S(t_j) \right)^2 + \sum_j \left(\delta_S^{(M)}(t_j) \right)^2}, \quad (1.12)$$

where the sums range over the XUV-NIR delays t_j . The goal of this procedure is to find γ_X that best reproduces the measured curve $\delta_X^{(M)}(t_0)$ according to model (1.11).

As an example, let's consider the case of a non-Gaussian ~ 226 as XUV pulse. This pulse has a constant GDD of $\sim 5885 \text{ as}^2$. However, since its spectrum (Figure 1.6-b) is irregular ($\eta_X^{(0)} \approx 0.5515$), i.e. it is asymmetric and contains some fine structure, its chirp β_X is time-dependent. The streaking field is a NIR pulse given by

$$A_L(t) = A_0 \cos^4(t/\tau_L) \sin(\omega_L t + \phi_0) \quad (1.13)$$

with $\tau_L \approx 5.743 \text{ fs}$, yielding a 3 fs full width at half maximum (FWHM) duration, $\omega_L \approx 2.355 \text{ rad/fs}$ corresponding to a central wavelength of 800 nm and with $A_0 \approx -0.41915 \text{ a.u.}$, giving a peak intensity of 20 TW/cm^2 . For this example, we will consider carrier-envelope phase values of $\phi_0 = 0$ (Figure 1.6-a) and $\phi_0 = \pi/2$ (Figure 1.6-b).

The simulated streaking measurements, shown in Figure 1.6-a and Figure 1.6-b, are composed of a sequence of streaked spectra computed for different delays between the XUV and NIR fields by propagating the time-dependent Schrödinger equation (TDSE) using a split-step FFT scheme. The Hamiltonian is that of a single electron in one dimension, assuming a soft-core potential with an ionization energy $W \approx 59 \text{ eV}$.

The results of the iCrap procedure, applied to the spectrograms shown in Figures 1.6-a and 1.6-b, are shown in Figures 1.7 and 1.8. In both cases, I applied iCrap to different subsets of streaked spectra, by considering a varying number N of spectra about the central delay value $t_0 = 0$.

For the case $\phi_0 = 0$, Figure 1.7-a shows a false-color plot of the figure of merit M as defined in (1.12). Darker areas correspond to a smaller value of M . When too few spectra are considered, Figure 1.7-a shows a local minimum near $\gamma_X = 12\,500 \text{ as}^2$ which disappears as more spectra ($N \gtrsim 13$) are considered. Nonetheless, Figure 1.7-b shows that we recover the exact GDD (the dashed line) from the global minimum to within $\sim 4\%$ with as few as three spectra. As N increases, the global minimum eventually stabilizes around the red dashed line representing the exact GDD, and iCrap converges nearly to the exact value $\gamma_X = 5885 \text{ as}^2$. Figure 1.7-c shows that the model (1.11) reproduces the correct curve $\delta_S(t_0)$ for the exact GDD.

For $\phi_0 = \pi/2$, Figure 1.8-a shows that the figure of merit has only one minimum as a function of GDD. This minimum quickly converges to the correct GDD as more spectra are considered in the evaluation, as displayed in Figure 1.8-b, and is already accurate to within 0.7% for $N = 13$ spectra. Figure 1.8-c shows that the model (1.11) once again reproduces the correct curve (hollow circles) of streaked breadths for the exact GDD $\gamma = 5885 \text{ as}^2$.

The main advantage of the iCrap procedure is that it requires very few spectra. As long as $A_L(t_0)$ is properly sampled by the delay step between the spectra, there is enough

information for iCrap to recover the GDD of the attosecond pulse. To illustrate this point, I apply iCrap to a subset of the spectra shown in Figure 1.6-a and 1.6-b. Specifically, I consider 17 spectra over the interval $[-2 \text{ fs}, 1.84 \text{ fs}]$ (containing 1.5 cycles of the streaking field), with a delay step of 240 as between them, i.e. a third of the original spectra in $[-2 \text{ fs}, 2 \text{ fs}]$. Even with so few spectra, iCrap still recovered accurate GDD's of 6150 as^2 and 6110 as^2 for $\phi_0 = 0$ and $\phi_0 = \pi/2$, respectively.

To further demonstrate iCrap's robustness against a non-Gaussian spectrum, let's now consider a clipped version of the XUV spectrum shown in Figure 1.6-c, for which I removed the energy components above 175 eV. Experimentally, such a sharp edge in the XUV spectrum might result from the beam's transmission through a metallic filter. Using the clipped XUV spectrum, I compute sets of 101 streaked photoelectron spectra, with the same parameters as those displayed in Figure 1.6-a and 1.6-b. In spite of this heavy clipping, iCrap recovers GDD's of 5940 as^2 and 5960 as^2 for $\phi_0 = 0$ and $\phi_0 = \pi/2$, respectively.

As previously mentioned, these examples assume a constant GDD over an irregular spectral distribution, resulting in a chirp β_X that depends on time. Since expression (1.11)—which is at the core of the iCrap procedure—assumes a constant chirp in time, then the chirp parameter β_X is interpreted as the *average* chirp over the attosecond pulse's temporal profile. Conversely, if a non-uniform GDD was considered, then iCrap would have recovered the *average* GDD over the spectral profile.

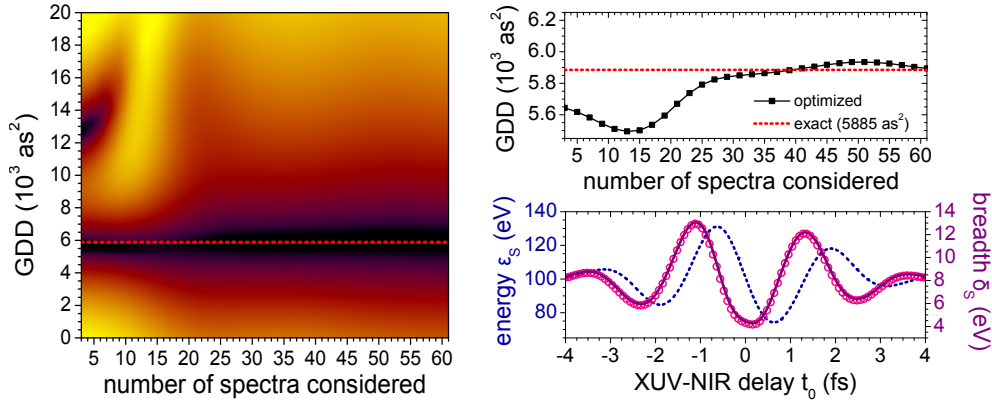


Figure 1.7: The analytical chirp evaluation (iCrap) is applied to the streaking example shown in Figure 1.6-a. Panel (a) is a false-color logarithmic plot of the figure of merit M , defined by (1.12), versus the number of spectra (N) considered for the iCrap procedure. Panel (b) plots the retrieved GDD (squares) at the global minimum of M as a function of N . In panels (a) and (b), the dotted red line represents the exact GDD. Panel (c) shows the energy ϵ_S (dotted line) and breadth $\delta_S^{(M)}(t_0)$ (solid line) evaluated from the streaked spectra. The hollow circles represent the breadths $\delta_S(t_0)$ computed from (1.11) with the exact $\gamma_X = 5885 \text{ as}^2$.

As an additional verification of iCrap's robustness, I now investigate the effect of noise in the streaked spectra. Thus, I add Poisson noise to the sets of 101 spectra shown in Figure 1.6-a and 1.6-b. Specifically, I assume that the number of counts n in a spectral bin

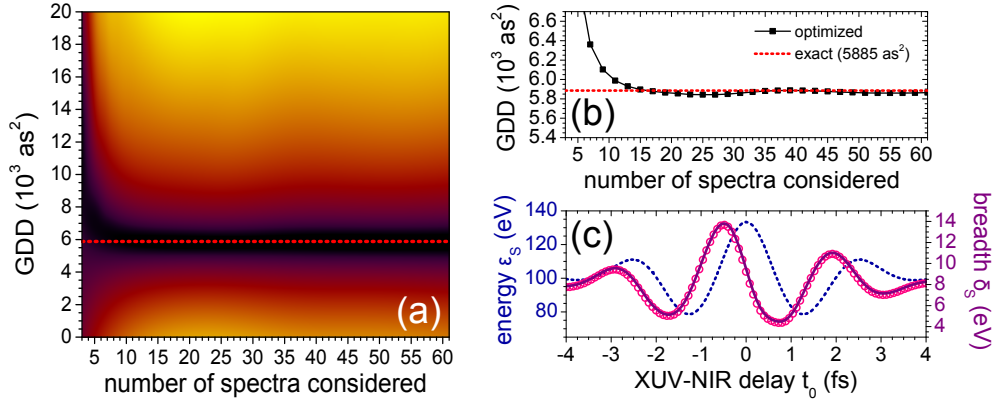


Figure 1.8: The analytical chirp evaluation (iCrap) is applied to the streaking example shown in Figure 1.6-b. The data shown here are presented in the same manner as in Figure 1.7.

follows a Poisson distribution $P(n; \mu) = \mu^n e^{-\mu} / n!$ with an expectation value μ proportional to the spectral intensity (I set $\mu = 1$ for the peak of the spectrogram, corresponding to a very low count rate). From these considerations, I compute the noisy spectra which are shown in Figure 1.9.

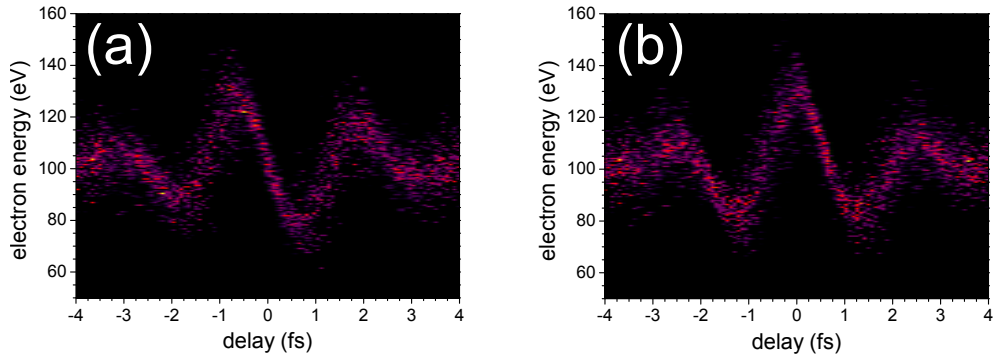


Figure 1.9: Panels (a) and (b) shows sets of streaked spectra, computed by adding Poisson noise to those of Figures 1.6-a and 1.6-b, respectively. iCrap recovers GDD's of 5590 as^2 and 6040 as^2 from the spectra in panels (a) and (b), respectively.

Even under such nefarious conditions, iCrap recovers accurate values of the GDD: 5480 as^2 from the spectrogram shown in Figure 1.9-a, and 5830 as^2 from the one in Figure 1.9-b. This example demonstrates that iCrap can tolerate very noisy spectra, and moreover that it is robust against errors in the vector potential $A_L(t_0)$, as evaluated from the streaked spectra.

In this section, I derived a general analytical expression (1.11) for the change in spectral breadth due to the streaking effect by considering the trajectories of a photoelectron ejected by an isolated attosecond pulse in a laser field. This shows that classical considerations are

sufficient to explain the main aspects of the streaking effect: the NIR-induced change in the center and the breadth of the photoelectron spectrum. These effects can in turn be used to reliably extract the most important parameters of the attosecond pulse, namely its chirp and its duration, from a streaking measurement. However, in order to measure its finer temporal characteristics, a more quantum-mechanical treatment of attosecond streaking is needed. This is the subject of the following section.

1.5 The Semi-Classical Description of Attosecond Streaking

In this section, I introduce the quantum-mechanical formalism and derive the semi-classical **master equation** [111, 96] that is used as a basis for extracting the complete temporal profile of an attosecond pulse from a set of laser-dressed photoelectron spectra—referred to as a *spectrogram*. I begin with the quantum-mechanical description of the attosecond streaking measurement, i.e. the momentum-resolved spectroscopy of photoelectrons ejected by an attosecond pulse in the presence of a dressing laser field. For simplicity, let's assume the single active electron (SAE) approximation, so that only one electron from the atom participates in the interaction with the laser field, and the others contribute an effective potential $V(\mathbf{r})$. This process is governed by the time-dependent Schrödinger equation (TDSE):

$$H(t)|\psi(t)\rangle = i\frac{d}{dt}|\psi(t)\rangle, \quad (1.14)$$

where atomic units ($\hbar = e = m_e = a_0 = 1$) are used to clean up the mess left behind by the physical constants. The electron's state vector is $|\psi(t)\rangle$, and its time evolution is determined by the Hamiltonian $H(t)$. Let's further assume that the radiation field is position-independent. This is the *dipole approximation*, and is valid when the smallest wavelength of the radiation field is still much larger than the size of the system (e.g. the largest possible extent of the electron's wave function). Within the dipole approximation, $H(t)$ can be written as

$$H(t) = \underbrace{(\mathbf{p} + \mathbf{A}_L(t))^2/2 + V(\mathbf{r})}_{H_L(t)} + \underbrace{\mathbf{F}_X(t) \cdot \mathbf{r}}_{V_X(t)}, \quad (1.15)$$

where \mathbf{p} is the canonical momentum operator, $\mathbf{A}_L(t)$ is the vector potential of the laser field, $V(\mathbf{r})$ is the shielded ionic potential, and $\mathbf{F}_X(t) = F_X(t)\hat{\mathbf{n}}_X$ is the electric field of the attosecond XUV pulse polarized along the unit vector $\hat{\mathbf{n}}_X$. The Hamiltonian $H_L(t)$ describes the laser field interacting with the electron as it moves in the potential $V(\mathbf{r})$, and the term $V_X(t)$ is responsible for populating continuum states, i.e. for photoionizing the system. The velocity gauge is used for describing the interaction between the electron and the NIR field, while the length gauge is used for its interaction with the attosecond XUV pulse. The reason for this choice of mixed gauges will soon become obvious.

At this point, we are still dealing with the traditional form of quantum mechanics, from which time-dependent perturbation theory can be used to derive bound-bound and bound-free transition amplitudes. However, as previously shown, the interaction between the electron and the NIR laser field the streaking regime is more intuitively described from the point of view of trajectories. Trajectories arise naturally by introducing time-evolution operators.

A time-evolution operator $U(t_0, t)$ is a unitary operator that propagates a state from an initial time t_0 to a later time t : $|\psi(t)\rangle = U(t_0, t)|\psi(t_0)\rangle$. This operator allows for a formal solution to the TDSE, but it is not explicitly known. Basically, by introducing it we have just transferred our ignorance of $|\psi(t)\rangle$ to ignorance of $U(t_0, t)$. Nevertheless, the time-evolution operator possesses a couple of useful properties: It satisfies the TDSE,

$$H(t)U(t_0, t) = i\frac{d}{dt}U(t_0, t), \quad (1.16)$$

as well as the obvious relation $U(t_0, t_0) = 1$. These properties allow us to write an exact formal solution to (1.14) as

$$|\psi(t)\rangle = -i \int_{t_0}^t U(t', t) V_X(t') U_L(t_0, t') |\psi(t_0)\rangle dt' + U_L(t_0, t) |\psi(t_0)\rangle. \quad (1.17)$$

Actually, two time-evolution operators, $U(t', t)$ and $U_L(t_0, t')$, appear in (1.17). These operators are associated respectively to the Hamiltonians H and H_L , and therefore obey the following Schrödinger equations:

$$H(t)U(t_0, t) = i\frac{d}{dt}U(t_0, t), \quad (1.18a)$$

$$H_L(t)U_L(t_0, t) = i\frac{d}{dt}U_L(t_0, t). \quad (1.18b)$$

Because the full Hamiltonian is separated into two parts, $H_L(t)$ and $V_X(t)$, the formal solution (1.17) consists of two terms. The second term simply represents the propagation of the initial state in the NIR field alone, it is solution to the TDSE when the term $V_X(t)$ is turned off. The first term contains the particular solution, which represents the photoionization dynamics. Physically, this term says that, at any moment t' , the system can feel a “kick” from the XUV field, after which it subsequently evolves under the full Hamiltonian $H_L(t)$ until the final time t . All these instantaneous kicks are added up coherently, via the integral, with probability amplitudes given by the instantaneous value of the attosecond XUV field ($V_X(t') = \mathbf{F}_X(t') \cdot \mathbf{r}$).

Now, since we're out to model the photoelectron spectrum, which amounts to energy-resolving the plane-wave components of the wave function, naturally we need to project (1.17) onto free-particle eigenbras $\langle \mathbf{p} |$, giving the probability amplitudes of the momentum components as

$$\tilde{\psi}(\mathbf{p}, t) \approx -i \int_{t_0}^t \langle \mathbf{p} | U_L(t', t) V_X(t') U_L(t_0, t') |\psi(t_0)\rangle dt', \quad (1.19)$$

for which two approximations are made. First, the contribution from the second term of (1.17) is neglected because the laser field is assumed to be too weak to significantly ionize or otherwise to produce energetic photoelectrons via ATI, which spectrally overlap with those emitted by the XUV field. In other words, we assume that the NIR field does not populate *relevant* free-particle eigenstates. Second, we ignore the action of the attosecond XUV field on the free electron, since attosecond XUV fields currently used in streaking measurements are still too weak to significantly drive free-free transitions; therefore, $U(t', t) \approx U_L(t', t)$.

Now, the operators $U_L(t_0, t')$ and $U_L(t', t)$ respectively account for the evolution of the bound system under the action of the laser field and the subsequent evolution of the free electron in the ionic potential, under the combined laser and XUV fields. These operators cannot be represented with closed-form expressions, and must be approximated in order to be rendered useful.

Firstly, we treat the operator $U_L(t', t)$ with the Coulomb-Volkov approximation (CVA) [51, 52, 117], which relies on semiclassical arguments to obtain a suitable approximation for $\langle \mathbf{p} | U_L(t', t)$. Before directly attacking this problem, let's first consider a simpler situation, where there is no dressing field ($\mathbf{A}_L(t) = 0$). In the absence of the dressing field, $\langle \mathbf{p} | U_L(t', t)$ can be viewed as a plane-wave state $\langle \mathbf{p} |$ propagated backwards in time from t to t' in the presence of the potential $V(\mathbf{r})$. Such a state corresponds to a plane wave incident upon a scattering potential $V(\mathbf{r})$. If the final time t is large enough, the state at time t' is approximately an incoming-type scattering state:

$$\langle \mathbf{p} | U_L(t', t) \rightarrow \langle \phi_{\mathbf{p}}^{(-)} | e^{-\frac{i}{2} p^2 (t-t_0)}, \text{ for } t \gg t' \text{ and } \mathbf{A}_L(t) = \mathbf{0} \quad (1.20)$$

($p = |\mathbf{p}|$), where the “ $(-)$ ” superscript denotes an incoming-type scattering state, i.e. corresponding to an advanced Green's function (see Appendix A for further details on this).

Now, for the CVA we modify this ansatz by making use of semi-classical arguments. We expect that an electron with a final energy $p^2/2$ at the detector must have started with an initial kinetic energy $(\mathbf{p} + \mathbf{A}_L(t'))^2/2$ at the initial moment t' of its ionization. Therefore, we project to the left on the initial scattering state as $\langle \phi_{\mathbf{p}+\mathbf{A}_L(t')}^{(-)} |$. Furthermore, we assume that the quantum phase accumulated by the free electron due to its interaction with the streaking field is not influenced by the ionic potential $V(\mathbf{r})$, but is solely due to the laser field. We therefore assign the Volkov phase,

$$\phi_L(t) = - \int_t^\infty \frac{1}{2} (\mathbf{p} + \mathbf{A}_L(t'))^2 dt' \quad (1.21)$$

to the free electron's state vector, which corresponds to propagation under the time-dependent Hamiltonian $(\mathbf{p} + \mathbf{A}_L(t))^2/2$. Thus, with the laser field, (1.20) is approximated under the CVA as

$$\langle \mathbf{p} | U_L(t', t) \approx \langle \phi_{\mathbf{p}+\mathbf{A}_L(t')}^{(-)} | e^{-\frac{i}{2} \int_{t'}^t (\mathbf{p}+\mathbf{A}_L(t''))^2 dt''}. \quad (1.22)$$

Hence, the CVA decouples the motion of the electron in the ionic potential, represented by the bra on the RHS, from its motion in the laser field, represented by the exponential

phase factor (containing the Volkov phase). Since we are still projecting onto field-free scattering states $\langle \phi_{\mathbf{p}+\mathbf{A}_L(t')}^{(-)} |$, the CVA is more accurate when the NIR electric field is weak, so that the ionic potential is minimally distorted and the states $\langle \phi_{\mathbf{p}+\mathbf{A}_L(t')}^{(-)} |$ form a suitable basis for representing the laser-dressed continuum. Moreover, the CVA works better when the photoelectron is energetic, so that it hardly feels the ionic potential. This makes the Volkov phase—which excludes the contribution from the ionic potential—more accurate in representing the quantum phase accumulated by the electron from the moment of its ionization until it reaches the detector.

Having dealt with $U(t', t)$, we now wish to approximate the first time-evolution operator $U_L(t_0, t')$, representing the propagation of the bound state prior to photoionization. For this, we assume that the bound electron doesn't feel the effect of the dressing field—either directly or through the laser-induced polarization of other electron shells. In this case, $U_L(t_0, t')$ can be approximated as $U_L(t_0, t') \approx e^{-iW(t'-t_0)}$.

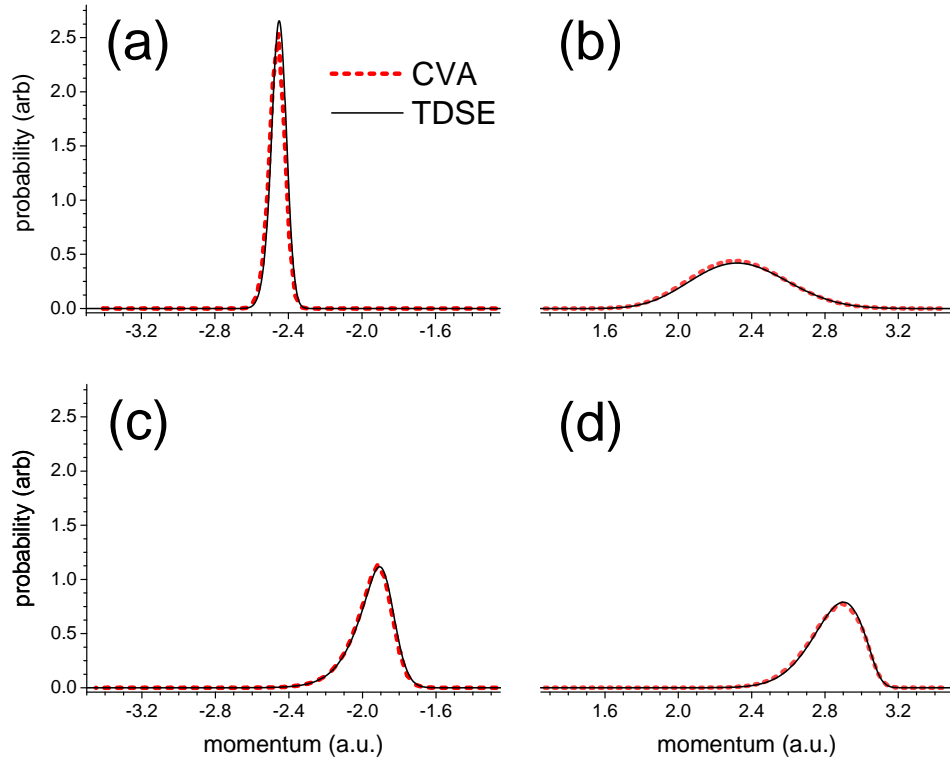


Figure 1.10: Streaked photoelectron spectra computed using the Coulomb-Volkov approximation (solid lines), computed from (1.23a), accurately represent the photoelectron spectra obtained by solving the TDSE (dotted lines). The top panels show streaked spectra for negative (a) and positive (b) momenta in the case where the ionization occurs near the peak of the NIR electric field. While for the bottom spectra, with negative (c) and positive (d) momenta, ionization occurs near a zero-crossing of the NIR electric field.

Finally, considering that the system began evolving long before its interaction with the XUV and NIR fields, $t_0 \rightarrow -\infty$, and that the electron reaches the detector much later, $t \rightarrow \infty$, we are now in a position to write down the **master equation** that is used for describing laser-dressed photoelectron spectra in the streaking regime:

$$I(\mathbf{p}, \tau) = \left| \int_{-\infty}^{\infty} F_X(t) d(\mathbf{p} + \mathbf{A}_L(t + \tau)) e^{i\phi_L(t+\tau, \mathbf{p})} e^{i(p^2/2 + W)t} dt \right|^2, \quad (1.23a)$$

$$\phi_L(t + \tau, \mathbf{p}) = - \int_{t+\tau}^{\infty} \left(\mathbf{p} \cdot \mathbf{A}_L(t') + \frac{1}{2} A_L^2(t') \right) dt', \quad (1.23b)$$

where we defined the matrix element of the dipole operator, between the bound state $|\psi(t_0)\rangle$ and the positive-energy scattering state $\langle\phi_{\mathbf{p}}^{(-)}|$, as $d(\mathbf{p}) = \langle\phi_{\mathbf{p}}^{(-)}|\mathbf{r} \cdot \hat{\mathbf{n}}_X|\psi(t_0)\rangle$, and introduced an explicit timing delay τ between the NIR and XUV fields such that the laser pulse precedes the attosecond pulse for positive values of τ .

The master equation (1.23a) is a result of numerous approximations to the exact expression (1.17). Nevertheless, streaked spectra computed with (1.23a) compare surprisingly well to those computed via the TDSE, as shown in Figure 1.10.

The main advantage of (1.23a) is that it enables quick calculations of streaked photoelectron spectra, avoiding lengthy TDSE simulations. However, as current desktop computers can perform fully three-dimensional single-electron TDSE simulations in a matter of minutes, why is the speed advantage afforded by this master equation so important? In the following section I will detail an algorithm that characterizes attosecond pulses by performing repeated and automated evaluations of (1.23a). In contrast to the iCrap procedure presented in Section 1.4, this algorithm is able to *fully* characterize the temporal profile of the attosecond pulse from a streaking spectrogram.

1.6 The Attosecond FROG

In a seminal paper from 2005 [134], Y. Mairesse and F. Quéré proposed to process a set of streaked photoelectron spectra, henceforth referred to as an *attosecond streaking spectrogram*, with the *Frequency Resolved Optical Gating* (FROG) algorithm [105, 197, 195]—a robust [65] technique widely used by the ultrafast optics community [115, 185, 11, 87, 217, 4, 26, 116] for characterizing the field of optical pulses—as a means to extract the full temporal profile of the attosecond pulse field $F_X(t)$.

The first step of the FROG technique consists in spectrally resolving a nonlinear cross-correlation signal between two time-delayed optical pulses, thus measuring a *FROG spectrogram*

$$I(\omega, \tau) = \left| \int_{-\infty}^{\infty} P(t) G(t + \tau) e^{i\omega t} dt \right|^2, \quad (1.24)$$

which is just the spectrum of a cross-correlation signal between a pulse $P(t)$ and a time-delayed gate $G(t + \tau)$.

For the second part of the FROG measurement, an inverse problem is solved to obtain the phases and amplitudes of the complex pulse $P(t)$ and gate $G(t)$ functions from the spectrogram $I(\omega, \tau)$. This phase retrieval is the subject of the current section. A solution to this phase retrieval problem exists because $I(\omega, \tau)$ is a two-dimensional object, and therefore contains more than enough information to recover a pair of one-dimensional complex objects. Thus, a pair $\{P(t), G(t)\}$ can be found that yields the measured spectrogram through the relation (1.24).

This particular two-dimensional phase retrieval problem cannot in general be solved analytically, so one must resort to optimization techniques to find a numerical solution for the pair $\{P(t), G(t)\}$. Fortunately, by the time the attosecond streak camera [96] appeared, some very efficient and robust optimization algorithms [196, 105, 104, 102] for dealing with this particular class of phase retrieval problems were already developed based on previous work done in the field of image processing [61, 62].

Of these algorithms, the most widely used for the purpose of FROG retrieval are the so-called *generalized projections* (GP) algorithms [122, 181, 43]. Within the context of FROG, the GP algorithm consists in applying alternating constraints to a pair of signals $\{P(t), G(t)\}$ between the time and frequency domains. As such, the FROG algorithm must perform repeated evaluations of the Fourier transform integral (1.24), which is done efficiently using the *Fast Fourier Transform* (FFT). A more detailed description of the FROG retrieval algorithm is postponed to the following section.

Now, in order to use a FROG algorithm to analyze an attosecond streaking measurement, the master equation (1.23a) describing the streaked spectra must therefore be put into the form given by (1.24). In particular, it has to be represented as a proper Fourier transform integral, which requires a couple of additional approximations to (1.23a). so that we can use the FFT. This

Let's assume a typical streaking geometry where the NIR and XUV fields are linearly polarized in the same direction, which also happens to be the observation direction of photoelectrons. This makes all quantities scalar: in particular, $d(\mathbf{p} + \mathbf{A}_L(t)) = d(p + A_L(t))$ and $\mathbf{p} \cdot \mathbf{A}_L(t) = pA_L(t)$. The master equation (1.23a) then simplifies to

$$I(p, \tau) = \left| \int_{-\infty}^{\infty} F_X(t) d(p + A_L(t + \tau)) e^{i\phi_L(t+\tau, p)} e^{i(p^2/2 + W)t} dt \right|^2, \quad (1.25a)$$

$$\phi_L(t + \tau, p) = - \int_{t+\tau}^{\infty} \left(pA_L(t') + \frac{1}{2}A_L^2(t') \right) dt'. \quad (1.25b)$$

Indeed, initial inspection of (1.25a) reveals that $I(p, \tau)$ somewhat resembles a Fourier transform. In fact, when the laser field is turned off, $e^{i\phi_L(t, p)} = 1$, and we see that $I(p, \tau)$ is simply proportional to a Fourier transform spectrum of the attosecond pulse: $I(p, \tau) = |d(p)\mathcal{F}[F_X(t)](p^2/2 - W)|^2$.

However, when the NIR field is turned on, the integral on the RHS of (1.25a) is not quite a FROG spectrogram. To put (1.25a) into the form (1.24), we need to eliminate the momentum dependence from the factors $d(p + A_L(t))$ and $e^{i\phi_L(t, p)}$ ¹³; this cannot be

¹³Actually, if $d(p + A_L(t))$ and $e^{i\phi_L(t, p)}$ could both be separated into pairs of purely time-dependent and

achieved without making a couple of additional approximations to (1.25a).

First, the photoionization cross-section of certain inert gases is sufficiently constant over the bandwidth of current attosecond pulses obtained through spectral filtering, such that the transition dipole matrix element $d(p + A_L(t + \tau))$ can be safely ignored altogether¹⁴. The second approximation consists in substituting the final momentum p with the central momentum of the streaked spectrum $p_S = p_C - A_L(\tau)$, where p_C is just the central momentum of the unstreaked photoelectron spectrum. Why don't we call this last one the *central momentum approximation* (CMA). With these additional amendments, (1.23a) further simplifies to

$$I(p, \tau) \approx \left| \int_{-\infty}^{\infty} E_X(t) e^{i\phi_L(t+\tau)} e^{i(p^2/2+W)t} dt \right|^2, \quad (1.26a)$$

$$\phi_L(t + \tau) \approx - \int_{t+\tau}^{\infty} \left(p_C A_L(t') - \frac{1}{2} A_L^2(t') \right) dt', \quad (1.26b)$$

The streaked photoelectron spectrum in the form (1.26a) is now a proper Fourier transform integral, which can be efficiently evaluated using the FFT. Moreover, it is of the form (1.24), and therefore can be processed with the FROG algorithm.

In the following sections, I will present a more detailed outline of the FROG retrieval algorithm, and establish its accuracy in the context of attosecond streaking with a couple of examples. I then showcase two implementations of FROG algorithms: the PCGPA and the LSGPA (these initialisms will be spelled out later). The PCGPA [101] was the implementation originally considered by Y. Mairesse and F. Quéré in 2005, and is currently the most widely used in attosecond science for the FROG reconstruction of attosecond pulses from streaking measurements. The second implementation is the LSGPA [72], which I developed during the course of these studies, and tailored for the specific purpose of processing streaking measurements of isolated attosecond pulses. In the following, we'll have a look at the inner workings of both the PCGPA and the LSGPA, I'll and compare their performance with an example.

1.6.1 FROG Reconstruction

The main idea behind FROG retrieval, based on a generalized projections (GP) algorithm, is to iteratively impose a set of constraints between two domains on the pulse $P(t)$ and the

momentum-dependent factors, e.g. $d(p + A_L(t)) = f_t(t)f_p(p)$ and $e^{i\phi_L(t,p)} = g_t(t)g_p(p)$, then the quantity $I(p, \tau)(f_p(p)g_p(p))^{-1}$ would be a true FROG spectrogram.

¹⁴It is important to note here that we just want to characterize an attosecond pulse. Therefore, any system with well-behaved properties, e.g. possessing a nearly uniform spectral response, will do. On the other hand, if these XUV pulses are used to probe some physical system, then its bound-free dipole response cannot be neglected. Later, in Section 2.1, we'll see that the presence of $d(p + A_L(t + \tau))$ in (1.23a) actually enables the characterization of a quantity related to the free electron wave packet, which is not quite a replica of the attosecond pulse for a system with a spectral non-uniform dipole response. The information about the electron wave packet can be obtained using the exact same algorithm I describe here!

gate $G(t)$. These constraints can be briefly stated as: (i) $P(t)$ and $G(t)$ must produce a spectrogram that matches the measured one, and (ii) $P(t)$ and $G(t)$ are required to produce that spectrogram via relation (1.24). GP algorithms employ an iterative and deterministic procedure to enforce these two constraints. The general outline of these algorithms now follows.

A complex spectrogram $\tilde{S}(\omega, \tau)$ is first computed from some initial guess $\{P(t), G(t)\}$:

$$\tilde{S}(\omega, \tau) = |\tilde{S}(\omega, \tau)|e^{i\tilde{\varphi}(\omega, \tau)} = \int_{-\infty}^{\infty} P(t)G(t)e^{i\omega t} dt. \quad (1.27)$$

Then, only the phase $\tilde{\varphi}(\omega, \tau)$ of $\tilde{S}(\omega, \tau)$ is retained, while its modulus is replaced with that corresponding to the measured spectrogram $I(\omega, \tau)$:

$$\tilde{S}(\omega, \tau) \rightarrow \tilde{S}'(\omega, \tau) = \sqrt{I(\omega, \tau)}e^{i\tilde{\varphi}(\omega, \tau)}. \quad (1.28)$$

This substitution, performed in the frequency domain, constitutes the first constraint imposed upon $P(t)$ and $G(t)$. For the second constraint, we require the time-domain representation of $\tilde{S}'(\omega, \tau)$, i.e.

$$S'(t, \tau) = \frac{1}{2\pi} \int_{-\infty}^{\infty} \tilde{S}'(\omega, \tau)e^{-i\omega t} d\omega, \quad (1.29)$$

to be the cross-correlation signal $P(t)G(t+\tau)$. This second constraint, enforced in the time domain, an optimal pair $\{P'(t), G'(t)\}$ must be found such that $P(t)G(t+\tau) \sim S'(t, \tau)$ for all delays τ . Following this optimization step, the newly-obtained $P'(t)$ and $G'(t)$ are then used as guesses for the next iteration of the algorithm, by grinding through (1.27-1.29). Wash, rinse and repeat for the subsequent iterations until convergence has been reached, at which point the final pair $\{P^{(f)}(t), G^{(f)}(t)\}$ yields the measured spectrogram $I(\omega, \tau)$ via the relation (1.24).

This pair is *almost* unique for a given spectrogram. Obviously, a change in the CEP's of $P(t)$ or $G(t)$, or an overall shift in time $\{P(t) \rightarrow P(t + \Delta t), G(t) \rightarrow G(t + \Delta t)\}$, do not affect the spectrogram. Consequently, neither the common absolute timing of $P(t)$ and $G(t)$ nor their individual CEP's can be deduced from the spectrogram. Moreover, the central frequency and normalization of $P(t)$ and $G(t)$ is ambiguous since the transformation $\{P(t) \rightarrow \lambda P(t)e^{i\omega_0 t}, G(t) \rightarrow \lambda^{-1}G(t)e^{-i\omega_0 t}\}$, for any frequency ω_0 and normalization factor λ , does not alter the spectrogram.

In ultrafast optics, this last ambiguity is typically removed because the signal $P(t)G(t+\tau)$ arises from a nonlinear optical effect, such that $G(t)$ is simply related to $P(t)$; e.g. $G(t) = P(t)$ when the second-harmonic is used, while $G(t) = P^2(t)$ corresponds a third-harmonic FROG measurement. Knowing the explicit relation between $P(t)$ and $G(t)$, there is no room for an ambiguity in the central frequency or the normalization of the retrieved pulse. However, comparing (1.24) with (1.26a), we see that the attosecond pulse $P(t) = E_X(t)$ is generally not related to the streaking gate

$$G(t) = e^{-i \int_t^{\infty} (p_C A_L(t') - \frac{1}{2} A_L^2(t')) dt'}, \quad (1.30)$$

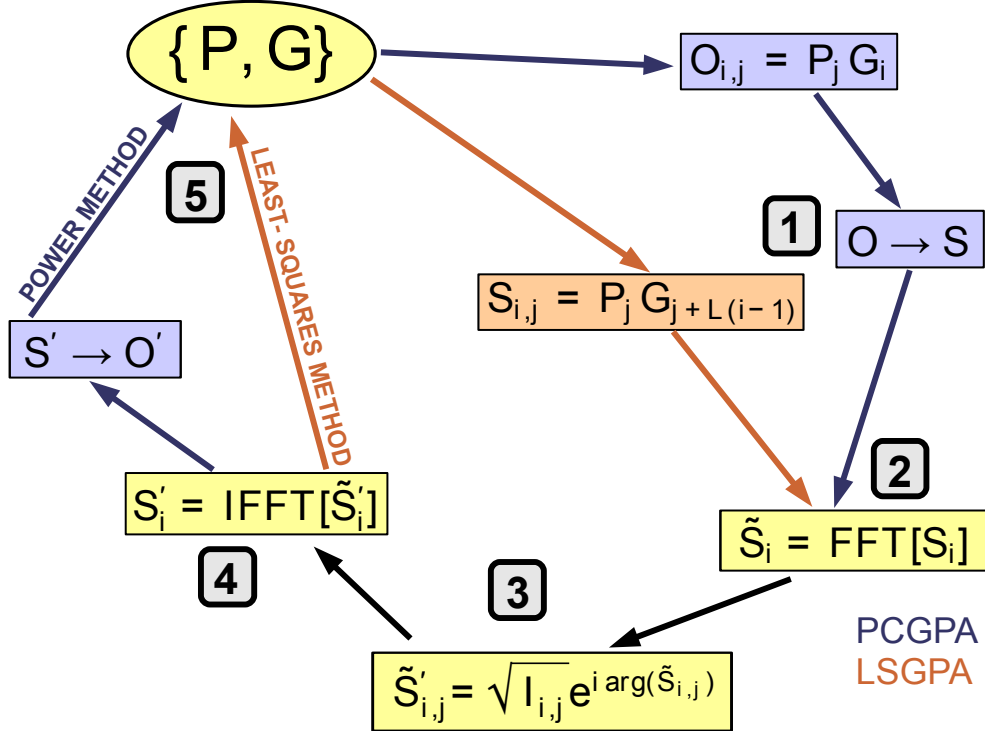


Figure 1.11: This diagram displays the steps involved in an iteration of the PCGPA and the LSGPA. The steps specific to the LSGPA are coloured in orange, the steps specific to the PCGPA are coloured in blue, and those shared by both algorithms are in yellow. From the current estimate of the pulse and gate pair $\{P^{(k)}, G^{(k)}\}$, a signal matrix is constructed (step 1) either via an outer-product matrix (PCGPA) or directly from the pulse and gate (LSGPA). The columns of the signal matrix are then Fourier transformed (step 2), their spectral intensity is then forced to be that of the measured FROG spectrogram $S^{(FROG)}$ (step 3), after which the columns are inverse Fourier transformed back into the time domain (step 4). A new pulse and gate pair $\{P^{(k+1)}, G^{(k+1)}\}$ is then extracted from the resulting signal matrix S' (step 5) either through the power method (PCGPA) or a least-squares minimization (LSGPA).

Even though in this case the laser field generated the attosecond pulse, the relation between these two fields is so complicated that it might as well be ignored! In brief, the attosecond streaking technique can resolve the attosecond pulse only up to a constant frequency, a constant phase, an absolute time and an overall normalization factor.

Now, the pair $\{P(t), G(t)\}$ that FROG retrieves from an attosecond streaking spectrogram can be interpreted as $\{E_X(t), e^{i\phi_L(t)}\}$ only if we can trust the mountain of approximations used to simplify the formal TDSE solution (1.17), giving the final FROG expression (1.26a). To proceed further, and justify the subsequent sections, we must first establish the reliability of all these approximations put together.

To this end, I present the results of a couple of numerical experiments that illustrate the reliability of the attosecond FROG reconstruction. For each example, I first compute an *ab initio* streaking spectrogram by numerically propagating the TDSE, and then use a FROG retrieval algorithm to reconstruct the original attosecond and NIR fields. Following these quality checks, we can then delve into the glorious algorithmic details of the PCGPA and LSGPA algorithms, in sections 1.6.1 and 1.6.2.

FROG Retrieval of an Isolated Attosecond Pulse

In this example, I demonstrate the FROG characterization of an isolated attosecond pulse that is asymmetric in time and embodies some fine temporal structure. The attosecond pulse has a FWHM duration of ~ 120 as with a photon energy of 180 eV. Ionization takes place in the presence of a 3 fs (FWHM) NIR streaking field with a peak intensity of 20 TW/cm^2 and a central wavelength of 800 nm. A simulated attosecond streaking spectrogram, composed of 201 spectra for XUV-NIR delays ranging from -5 fs to $+5$ fs, is shown in Figure 1.12-a. The spectra are computed by numerically solving the TDSE for a single electron moving in a soft-core potential; the ionization energy of the system is $W \approx 59$ eV. The TDSE is propagated using a spectral method with symmetric operator splitting between kinetic and potential energy. The only approximation used in this simulation is the dipole approximation, where the spatial dependence of both the NIR and XUV fields is altogether neglected.

The results of the application of the FROG algorithm to process the TDSE spectrogram are shown in Figures 1.12-b, c and d. Panels (c) and (d) show the reconstructed attosecond pulse in the temporal and spectral domains, respectively. The intensity and phase profiles are well characterized, although the phase is a little off. This is likely due to the energy-dependent response $d(p)$ of the system to single-photon ionization, which is ignored in the present treatment for the attosecond FROG reconstruction.

Figure 1.12-b shows the reconstructed vector potential of the NIR streaking field. The vector potential is obtained by taking the time derivative of the phase $\phi_L(t)$ (1.26b), given by

$$\dot{\phi}_L(t) = p_C A_L(t) - \frac{1}{2} A_L^2(t). \quad (1.31)$$

This quadratic equation can be solved for $A_L(t)$ at each moment t , and thereby yields the *complete* waveform of the NIR field, without any ambiguities whatsoever.

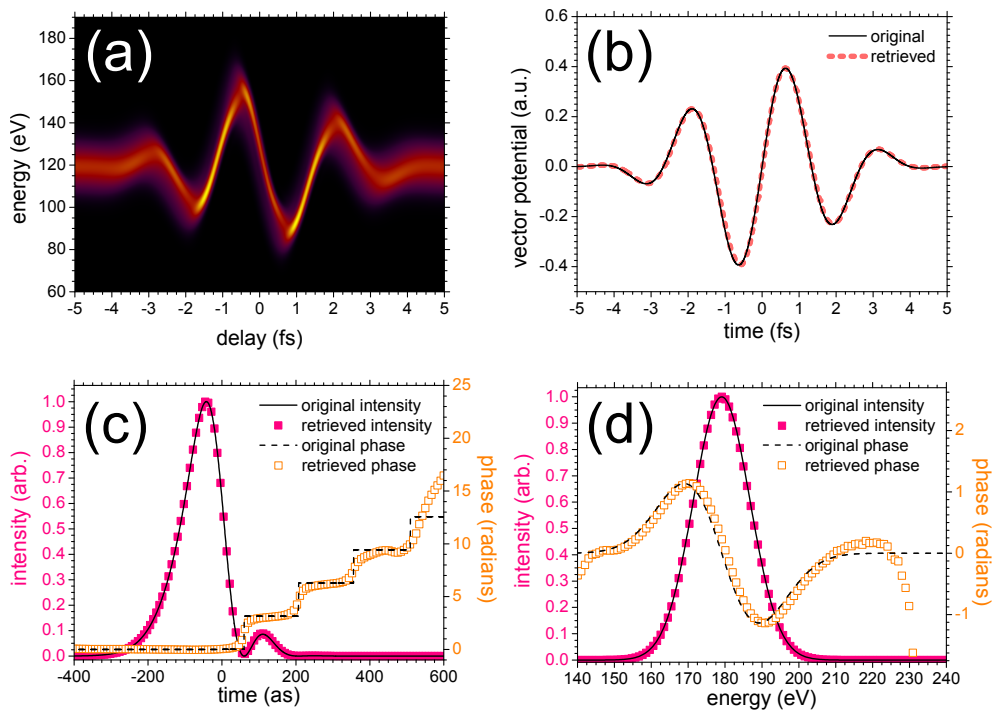


Figure 1.12: An *ab initio* spectrogram numerically evaluated from the TDSE (a) is processed with our attosecond FROG reconstruction algorithm. We are able to characterize the NIR pulse (b) and the complex amplitude of the attosecond pulse (c); the Fourier domain representation of the attosecond pulse is shown in (d).

FROG Retrieval of a Sequence of Two Attosecond Pulses

While typical attosecond experiments strive to obtain a perfectly isolated attosecond pulse, practical limitations of the temporal gating or spectral filtering methods result in a sequence of two or more attosecond pulses, due to recollision events engendered by adjacent laser half-cycles. Currently available ultrashort laser pulses ensure that at most two half-cycles of the laser field produce significant attosecond bursts [85].

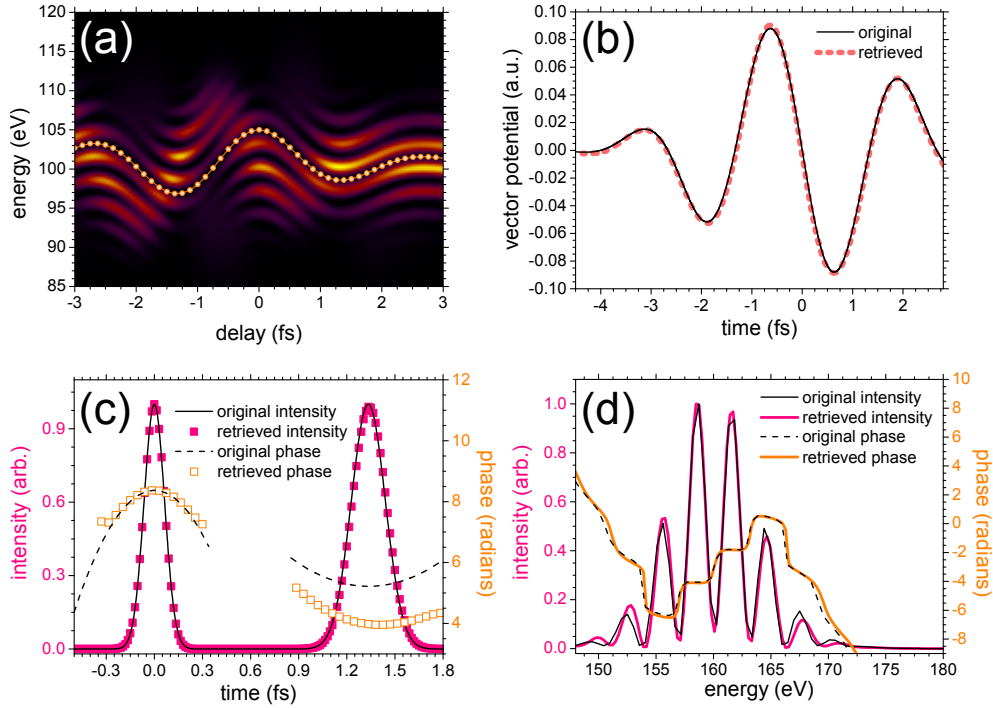


Figure 1.13: The original spectrogram (a) is computed by solving the TDSE (1.14), the dotted line represents the fringe position evaluated analytically as $\varsigma(\tau_S)/\Delta_X$, where $\varsigma(\tau_S)$ is given by (1.33). Panel (b) shows the original and reconstructed vector potential of the NIR field, while the attosecond double pulse structure is shown in the time domain (c) and in the frequency (energy) domain (d).

As an example of a streaking measurement performed with a sequence of two attosecond pulses, I model the streaking field as a 3.0 fs FWHM laser pulse with a peak intensity of 1.0 TW/cm^2 and a central wavelength of 800 nm. The XUV field consists of a sequence of two Gaussian pulses of equal peak intensities, but with durations (and group-delay dispersions) of 150 as (-1974 as^2) and 250 as (3937 as^2). Both pulses are given phases with linear chirp, and both are centered at an energy of 100 eV beyond the ionization energy $W \approx 59 \text{ eV}$. The spectrogram, shown in Figure 1.13-a, is computed by numerically solving the TDSE (1.14) assuming the same Hamiltonian as that used for the previous FROG reconstruction. The spectrogram shown in Figure 1.13-a displays a particular fringe pattern that oscillates somewhat like the streaking field. This fringe pattern is due to the

self-interference of the electron ejected over two distinct attosecond time intervals. Since there is no way to know which of the two attosecond pulses released the electron, the photoelectron contributions from the two attosecond pulses add coherently and produce an interference pattern when spectrally resolved interfere at the detector. This effect is akin to a double-slit experiment [130]. Only, the slits are opened in time instead of space. The change of this fringe pattern as a function of the XUV-NIR delay can be explained by considering the difference in phase between two electron trajectories, each launched by one of the two attosecond pulses, at different moments in time in the NIR field.

This interference presents a fringe spacing that is inversely proportional to the time between the attosecond pulses. Thus, it consists of spectral fringes separated by twice the laser frequency, similar to a photoelectron spectrum measured using the RABITT technique. However, unlike the RABITT spectrum—which relies on an *intensity* modulation of the fringes by the NIR field—in this case the NIR field changes the *position* of the fringe pattern! This is how the two-way interference between electron trajectories, launched at different moments in time into the NIR field, manifests itself when generated by a sequence of only two attosecond pulses instead of a longer train of pulses.

The position of the fringes is given by the phase difference $\Delta\varsigma = \phi_L(t_1, p_1) - \phi_L(t_2, p_2)$ associated to electron trajectories launched at momentum t_1 and t_2 with momenta p_1 and p_2 , respectively, where

$$\phi_L(t, p_C) = - \int_t^\infty \left(p_C A_L(t') - \frac{1}{2} A_L^2(t') \right) dt' \quad (1.32)$$

is just the Volkov phase: the additional phase given by the NIR field to the photoelectron, launched by an attosecond pulse at time t with initial momentum p_C , as described by the CVA (1.22) within the CMA. The relative phase $\Delta\varsigma$, which sets the position of the fringes in the spectrogram, is akin to the relative action between the two electron trajectories launched at moments t_1 and t_2 .

If one of the attosecond pulses is centered at the XUV-NIR time delay τ , and the other one at time $\tau + \Delta t_X$, then for a given time interval Δt_X separating the pulses, the phase difference $\Delta\varsigma$ is a function of the time delay τ between the XUV and NIR fields. Considering that $|A_L(t)| \ll p_C$ (the vector potential is much smaller than the electron momenta in typical attosecond streaking measurements), then $A_L^2(t)$ can be neglected, the relative phase is approximately

$$\Delta\varsigma(\tau) \approx p_2 B_L(\tau + \Delta t_X) - p_1 B_L(\tau), \text{ with } \frac{dB_L(t)}{dt} = A_L(t), \quad (1.33)$$

where I consider that the two attosecond pulses can have different central energies, so the electron can be launched at time τ with momentum p_1 or at time $\tau + \Delta t_X$ with momentum p_2 . The dotted line plotted on top of the spectrogram in Figure 1.13-a is a plot of the fringe position $\Delta\varsigma(\tau)/\Delta t_X$, as given by (1.33), with respect to the XUV-NIR delay τ .

The results of the FROG reconstruction of the sequence of two attosecond pulses are shown in Figures 1.13-b, c and d. The reason why the streaking field is so weak

(1.0 TW/cm^2) is to preserve the CMA's validity. I must point out here that the CMA—which substitutes $p \rightarrow p_C - A_L(\tau)$ —is much more restrictive when used to model a spectrogram composed of a double attosecond pulse.

For a sequence of two attosecond pulses, the streaking field shifts the spectral components of the two electron wave packets—generated at different moments in time by each attosecond pulse—by different amounts. If the streaking field is too strong, then the CMA makes little sense: For certain delays τ , the attosecond pulses overlap with very different values of the vector potentials, $A_L(\tau)$ and $A_L(\tau + \Delta t_X)$. Since the CMA assumes that the electron encounters one and only one value of the vector potential $A_L(\tau)$ for a given delay τ , the CMA is not such a good approximation for describing streaking with a sequence of two attosecond pulses. Nevertheless, if the streaking field is sufficiently weak, then we may say that the final electron momentum p is roughly equal to the initial momentum p_C for all of the delays τ , in which case the CMA is once again a reasonable approximation.

In light of this issue, I chose a rather weak streaking field for this example. Consequently, the spectrogram shown in Figure 1.13-a exhibits hardly any spectral shift, and the streaking effect mainly shows up as a change in the interference pattern. Judging from the quality of the retrieved XUV and NIR fields, the CMA seems to be valid in this case.

Aside from the CMA, the FROG retrieval again ignores $d(p)$, the non-uniform spectral response of the system to single-photon ionization. As a result, the retrieved spectrum is noticeably distorted compared to the original one, as shown in Figure 1.13-d. Specifically, since the photoionization cross section decreases with energy, the retrieved spectrum overestimates the power at lower energies and underestimates it at higher energies. In addition, the retrieved spectral modulation rate is slightly off, which may be due to the energy-dependence of the phase of the dipole matrix element $d(p)$.

These small “mistakes”¹⁵ do not appear to greatly hamper the characterization of the attosecond pulses in time. Their retrieved durations are off by only $\sim 0.4\%$ and their dispersions are recovered to within $\sim 5\%$. As well, their relative timing is overestimated by a mere $\sim 0.5\%$, their relative intensity retrieved to within $\sim 1\%$ while a small mistake of $\sim 0.25 \text{ eV}$ is made in their relative energy. However, the relative phase between them was not properly characterized—their relative CEP is overestimated by as much as ~ 1.26 radians.

Therefore, we conclude that although the FROG technique cannot recover the relative phase between two attosecond pulses in a sequence [72], it otherwise performs admirably. Having established the general validity of FROG reconstruction, as applied to attosecond streaking measurements, we can now take a closer look at the two main FROG algorithms—both based on generalized projections (GP)—that are used by the attosecond science community.

¹⁵When $d(p)$ is not ignored in the formalism, the attosecond FROG algorithm actually characterizes a quantity related to the photoelectron wave packet, as will be described in Section 2.2. Therefore, what are presented here as deviations in the retrieved attosecond pulses are not mistakes, but are actually physical!

1.6.2 The PCGPA

One of the most reliable and efficient of these GP algorithms is the *Principal Components Generalized Projections Algorithm* (PCGPA), schematically represented in Figure 1.11. The PCGPA represents the pulse and gate as N -component vectors, with components given by

$$P_i = P(t_i), G_i = G(t_i), 1 \leq i \leq N. \quad (1.34)$$

From these vectors, a matrix can then be formed from the outer product of \mathbf{P} and \mathbf{G} ,

$$O = \begin{pmatrix} P_1 G_1 & P_1 G_2 & \dots & P_1 G_{N-1} & P_1 G_N \\ P_2 G_1 & P_2 G_2 & \dots & P_2 G_{N-1} & P_2 G_N \\ \vdots & \vdots & \ddots & \vdots & \vdots \\ P_{N-1} G_1 & P_{N-1} G_2 & \dots & P_{N-1} G_{N-1} & P_{N-1} G_N \\ P_N G_1 & P_N G_2 & \dots & P_N G_{N-1} & P_N G_N \end{pmatrix}. \quad (1.35)$$

Then, a signal matrix S is obtained by circularly shifting the rows of the outer-product matrix:

$$S = \begin{pmatrix} P_1 G_1 & P_1 G_2 & \dots & P_1 G_{N-1} & P_1 G_N \\ P_2 G_2 & P_2 G_3 & \dots & P_2 G_N & P_2 G_1 \\ \vdots & \vdots & \ddots & \vdots & \vdots \\ P_{N-1} G_{N-1} & P_{N-1} G_N & \dots & P_{N-1} G_{N-3} & P_{N-1} G_{N-2} \\ P_N G_N & P_N G_1 & \dots & P_N G_{N-2} & P_N G_{N-1} \end{pmatrix}. \quad (1.36)$$

This reversible row-shifting operation results in a matrix S whose columns are grid-representations of the cross-correlation signal $P(t)G(t+\tau)$. Of course, in doing so we have assumed periodic boundary conditions on $G(t)$. This is a valid assumption when the gate is localized in time, i.e. a pulse, but this is not so for the gate (1.30) used in attosecond streaking, whose modulus is non-zero for all time. Fourier-transforming the columns of S thus produces a complex FROG spectrogram, as indicated by step 2 in Figure 1.11 for the iterative GP procedure.

For the time-domain constraint (step 5 in Figure 1.11), where an optimal pulse and gate are extracted from the signal matrix S , the PCGPA makes use of a special property of the outer-product matrix O : this matrix has only one non-zero eigenvalue, associated to one single left-eigenvector \mathbf{P} , and one single right-eigenvector \mathbf{G} .

After applying the frequency-domain constraint (1.28), the resulting matrix O' is no longer an outer-product matrix as given by (1.35). That is, it actually possesses several non-zero eigenvalues and eigenvectors. Still, the left and right eigenvectors of O' with the largest eigenvalue (in absolute value) give the largest contribution to this matrix and can therefore be taken as the pulse and gate pair to be used for the next iteration of the PCGPA. This pair of vectors, $\{\mathbf{P}, \mathbf{G}\}$, can be obtained efficiently using just a few (p)

iterations the power method,

$$\mathbf{P}^{(k+1)} = (OO^\dagger)^p \mathbf{P}^{(k)}, \quad (1.37a)$$

$$\mathbf{G}^{(k+1)} = (O^\dagger O)^p \mathbf{G}^{(k)}. \quad (1.37b)$$

The PCGPA is a very robust algorithm, and has been used in a wide range of FROG applications [103]. As previously mentioned, it is also the algorithm that was considered in the first proposal for the FROG reconstruction of attosecond pulses from streaking measurements [134], and has since been in use throughout the attosecond science community [168, 194, 1, 78], notably for the characterization of the record-breaking attosecond pulses generated by G. Sansone *et al.* in 2006 [168]. Unfortunately, the PCGPA has a couple of disadvantages.

First, the signal matrix S , as given by (1.36), assumes that the gate can be represented with periodic boundaries. If $G(t)$ is a pulse, which is often the case in the conventional FROG of ultrafast optics, then the assumption of periodic boundaries holds since the value and derivatives of $G(t)$ are all null at the boundaries. However, the gate used for streaking, as given by (1.30), has a unit modulus and is therefore infinitely extended in time. Furthermore, the streaking gate $G(t)$ is certainly not periodic if the NIR laser field is an ultrashort pulse.

The second and most important shortcoming of the PCGPA is the fact that it requires a strict sampling relationship between the delay and frequency axes of the spectrogram. Specifically, if the spectrogram occupies a total frequency range of $\Delta\omega$, then the PCGPA assumes that the delay step $\delta\tau$ satisfies

$$\delta\tau\Delta\omega = 2\pi. \quad (1.38)$$

Streaking measurements with very short attosecond pulses require a strong streaking field in order to significantly alter the photoelectron's momentum distribution in a very short period of time. Since a strong streaking field induces a large spectral shift, an attosecond streaking spectrogram potentially occupies a very large range of energies—much larger than the photoelectron original, field-free bandwidth.

For example, a streaking measurement of a ~ 80 as XUV pulse might require a total energy range of $\Delta\omega \gtrsim 80$ eV to capture the entire spectrogram [85]. In order to satisfy the sampling condition (1.38), the spectrogram has to be measured with a delay step no larger than $\delta\tau \sim 50$ as. Such a short delay step is experimentally impractical, because the full spectrogram needs to be recorded quickly enough, so as to minimize the drift of experimental parameters. For this reason, attosecond streaking spectrograms are measured with a delay step larger than that required by (1.38), and must therefore be re-sampled (e.g. interpolated) along the delay axis prior to being processed with the PCGPA.

Re-sampling the spectrogram with respect to the delay axis essentially amounts to inserting “fake” spectra in between the originally measured ones. If the features of a spectrogram change sufficiently smoothly with respect to the XUV-NIR delay, then these artificial spectra may accurately represent what would have been measured if a finer delay

step were used. But as we'll see, this is not generally the case, especially for spectrograms recorded with a strong streaking field or when the attosecond field consists of a train of two pulses.

1.6.3 The LSGPA

To alleviate the main shortcomings of the PCGPA, I invented a different FROG algorithm for processing attosecond streaking spectrograms. This algorithm, which I term the *Least-Squares Generalized Projections Algorithm* (LSGPA), ensures a more reliable reconstruction of very short (< 100 as) attosecond pulses by eliminating the assumption of periodic boundary conditions on the gate $G(t)$, as well as the need to interpolate the attosecond streaking spectrogram along the delay axis. The LSGPA is therefore more suitable for reconstructing shorter attosecond pulses, as well as a sequence of two attosecond pulses. To wit, the LSGPA was used for the attosecond FROG reconstructions shown in Figures 1.12 and 1.13.

The LSGPA defines the signal matrix S with the elements $S_{i,j} = P_j G_{j+(i-1)L}$, or more explicitly as

$$S = \begin{pmatrix} P_1 G_1 & P_1 G_{1+L} & \cdots & P_1 G_{1+(N_\tau-2)L} & P_1 G_{1+(N_\tau-1)L} \\ P_2 G_2 & P_2 G_{2+L} & \cdots & P_2 G_{2+(N_\tau-2)L} & P_2 G_{2+(N_\tau-1)L} \\ \vdots & \vdots & \ddots & \vdots & \vdots \\ P_{N-1} G_{N-1+L} & P_{N-1} G_N & \cdots & P_{N-1} G_{N-1+(N_\tau-2)L} & P_{N-1} G_{N-1+(N_\tau-1)L} \\ P_N G_N & P_N G_{N+L} & \cdots & P_N G_{N+(N_\tau-2)L} & P_N G_{N+(N_\tau-1)L} \end{pmatrix}, \quad (1.39)$$

where N_τ is the number of columns in the spectrogram. Figure 1.14 shows a schematic of this new version of the signal matrix. Essentially, the spectrogram is built from spectra computed by shifting the pulse vector along the gate vector by a certain number $L \geq 1$ of time-sample increments. There are two main advantages in defining S this way. First of all, there is no need to assume that the gate vector \mathbf{G} has periodic boundaries, owing to the fact that it is formally represented over a temporal window $\Delta t_G = \Delta t_P + L\Delta\tau$ which is larger than the spectrogram's delay range $\Delta\tau$ and the pulse's temporal range Δt_P . As a positive side effect of this representation, the gate can be reconstructed over a larger temporal window than that of the spectrogram, because the first few spectra located at extremal delays contain contributions from the gate that lie outside the delay range $\Delta\tau$.

The second and most important feature of (1.39) is the explicit inclusion of the free integer parameter L , which defines the time interval between adjacent spectra, i.e. the spectrogram's delay step. For $L = 1$, we recover the sampling condition (1.38) of the PCGPA, which assumes the spectrogram's delay step $\delta\tau$ is the same as δt , the time sample used to represent $P(t)$ and $G(t)$, which is inversely related to the total bandwidth of the spectrogram. As mentioned, this time sample is typically much smaller than $\delta\tau$ for attosecond streaking spectrograms, which means that the spectrogram's delay step $\delta\tau$ has to be adjusted (by interpolating it along the delay axis) before it can be processed with the PCGPA.

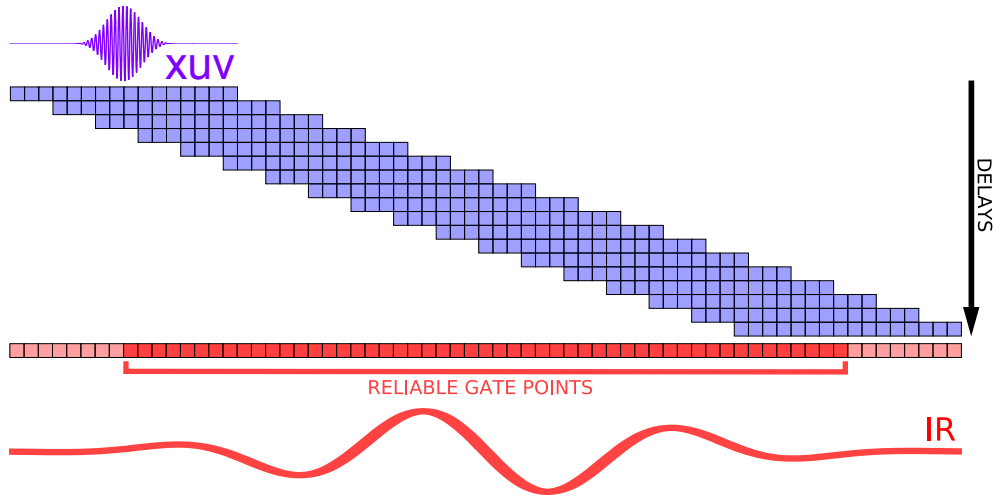


Figure 1.14: In the LSGPA, the signal matrix is computed by moving the discrete XUV pulse over the discrete streaking gate (1.30) consecutively by a finite number of time increments L . If the XUV pulse is short and centered in time, then the values of the gate located outside the delay range of the spectrogram (represented by the lighter red squares on the gate vector) never overlap with significant parts of the pulse. These extremal gate points are not faithfully recorded in the signal matrix, and thus should be ignored when using (1.42a) to extract the pulse from the signal matrix (step 5 of the LSGPA).

However, by adding the additional free parameter $L \geq 1$, I formally allow the delay step $\delta\tau$ to be larger than the time sample δt . In doing so, I achieve a much less stringent sampling condition between the spectrogram's delay step $\delta\tau$ and its total bandwidth $\Delta\omega$:

$$\delta\tau\Delta\omega = 2\pi L. \quad (1.40)$$

In fact, this weaker sampling requirement obviates the need to interpolate the spectrogram along the delay axis because it can be satisfied simply by choosing a large enough integer value for L , and then accordingly adjusting the spectral range $\Delta\omega$ without touching the spectrogram's delay step $\Delta\tau$. Thus, (1.40) can be satisfied by just zero-padding and re-sampling the individual spectra for some $\delta\tau$ and some $L \in \mathbb{N}$.

Zero-padding the spectra is certainly not a problem provided they don't possess any components outside of the recorded spectral range. Interpolating the spectra is also acceptable provided they were originally sampled at the Nyquist rate, so as to capture all the relevant spectral features. So basically, the freedom to choose L allows us to preserve the original delay step $\delta\tau$, thus avoiding the need to add fake spectra to the spectrogram.

The definition (1.39) of the signal matrix actually kills *three* birds with one stone:

- refraining from “polluting” the streaking spectrogram with artificial spectra, and instead including the large delay step into the formalism, makes the FROG reconstruction more reliable and robust;

- avoiding to needlessly increase the size of the spectrogram can drastically accelerate the FROG reconstruction's speed of execution;
- since the LSGPA computes the signal matrix directly from the pulse and gate, two of the PCGPA's algorithmic steps, denoted as $O \rightarrow S$ and $S \rightarrow O$ in Figure 1.11, are now irrelevant, further accelerating the execution speed of the FROG reconstruction.

Now, by adopting this new definition of the signal matrix, the PCGPA's elegant formalism—which exploits the outer-product matrix O and its eigenvectors \mathbf{P} and \mathbf{G} —must be replaced. In particular, the LSGPA employs a different scheme for extracting the pulse and gate pair from the signal matrix (step 5 in Figure 1.11) after applying the frequency-domain constraint (step 3).

To accomplish this minimization step, the LSGPA uses a strategy based on least-squares minimization. First, I begin by defining a figure of merit

$$M = \sum_{i=1}^{N_\tau} \sum_{j=1}^N |P_j G_{j+L(i-1)} - S_{i,j}|^2, \quad (1.41)$$

representing the “distance” between the signal matrix S obtained after application of the spectral constraint, and an “ideal” signal matrix which results from a unique pulse and gate pair $\{\mathbf{P}, \mathbf{G}\}$. As \mathbf{P} and \mathbf{G} are parameterized with respect to their points on a temporal lattice, a least-squares minimization of M (1.41) with respect to these parameters, $\{P_j, G_k\}$ leads to the following coupled set of equations:

$$P_j = \frac{\sum_m S_{m,j} G_{j+L(m-1)}^*}{\sum_m |G_{j+L(m-1)}|^2} \quad (1.42a)$$

$$G_k = \frac{\sum_n S_{n,k-L(n-1)} P_{k-L(n-1)}^*}{\sum_n |P_{k-L(n-1)}|^2}. \quad (1.42b)$$

Solving this coupled set of equations for \mathbf{P} and \mathbf{G} cannot be done analytically, but iterative approximations, analogous to the PCGPA's power method (1.37b) and (1.37a), are sufficient. Specifically, an approximate solution can be obtained iteratively by inserting the previous gate into (1.42a), and then using that pulse in (1.42b). Applying this procedure a number of times produces a pulse and gate pair that roughly minimizes the figure of merit M given by (1.41). In fact, the pair $\{\mathbf{P}, \mathbf{G}\}$ thus found may actually be quite a poor approximation to the true solution of the equations (1.42a) and (1.42b). Nevertheless, the key point here is that the spectrogram computed from this newly found pulse and gate pair is *closer* to the measured one than the spectrogram of the previous iteration, so that successive iterations lead us closer to the correct result.

In practice, the summations over m in (1.42a) are not done over all points of the gate \mathbf{G} . Indeed, some of those points are unreliable and should be ignored, particularly those located near the edges of the gate vector, which never overlap with significant parts of the pulse. Since the signal matrix provides reliable information about the gate only where it

overlaps with sufficiently intense portions of the pulse, information about these extremal gate points is absent from the signal matrix, and therefore also the spectrogram. These values of the gate vector \mathbf{G} , shown as the lighter read blocks along the gate vector in Figure 1.14, are unreliable and should be ignored when calculating the pulse from (1.42a). Given that the attosecond pulse is centered in time, and typically occupies just a small fraction of the vector \mathbf{P} , the unreliable gate points are the first $N_P/2$ and last $N_P/2$ samples of \mathbf{G} .

Moreover, before applying (1.42a), the gate vector \mathbf{G} must be “smoothed”. This is because, according to (1.42b), each point of \mathbf{G} is calculated from only a subset of points in \mathbf{P} , while each point of \mathbf{P} is computed from the same subset of points in \mathbf{G} . All in all, L subsets of the pulse and gate vectors are calculated independently from equations (1.42a) and (1.42b). These subsets represent downsampled versions of the pulse \mathbf{P} and gate \mathbf{G} , with a downsampling factor of L .

In other words, the full pulse and gate obtained through (1.42a) and (1.42b) are multiplexed from these independent downsampled versions. For $L > 1$, this creates artifacts which are manifested as slight oscillations in the time series \mathbf{P} and \mathbf{G} , with a period equal to the delay step.

Since the streaking gate’s phase and modulus oscillate at the period NIR of the field, which is much longer than the delay step, these fine artificial oscillations must be suppressed—using various possible smoothing techniques, e.g. adjacent averaging, low-pass filtering, Savitzky-Golay smoothing—before computing the next pulse from (1.42a). This prior smoothing of \mathbf{G} effectively couples the multiplexed downsampled versions of the pulse and gate. Without this smoothing, the iteration procedure described by (1.42a) and (1.42b) generally fails.

1.6.4 A Comparison Between the LSGPA and the PCGPA

I now present an example which shows the failure of the PCGPA, due mainly to its restrictive sampling constraint (1.38). I consider the XUV field to be composed of a sequence of two attosecond pulses, since the previous analysis has shown the attosecond FROG reconstruction to be slightly less robust in this case.

Since temporal gating and spectral filtering techniques are optimized for one particular half-cycle, one of the attosecond pulses is more intense than the other one. Let’s call the weaker one the *satellite* pulse, and the stronger one the *main* pulse. The two attosecond pulses are separated by a half-period (~ 1.25 fs) of the NIR field, and have a 3 : 2 peak intensity ratio. The main pulse has a duration of 85 as while the satellite measures only 76.5 as; both are assigned phases with chirp, as shown in Figure 1.15-d. The NIR laser pulse, used for streaking, is modeled as a chirped Gaussian pulse with a FWHM duration of 4 fs, a peak intensity of ~ 24 TW/cm², a central wavelength of 750 nm and a uniform GDD of 2 fs².

The fringe pattern in the spectrogram, resulting from the spectral interference of photoelectrons released by the two attosecond pulses, must be properly resolved if both pulses are to be reconstructed from the spectrogram. Any defection of the fringe pattern will corrupt the relative phase, relative intensity and relative timing between the retrieved pulses,

as will be shown in further detail in Section 1.7.1.

For this example, we wish to directly compare the performance of the PCGPA and LSGPA algorithms, and avoid any extra complications arising from the various approximations made to the formal TDSE expression (1.17). Thus, the original spectrogram is computed using the FROG expression (1.26a).

The spectrogram, shown in Figure 1.15-a is spectrally resolved with 256 energy samples, at a resolution of ~ 0.64 eV, and temporally resolved with 65 delay samples taken at intervals $\delta\tau = 100$ as. This delay step is rather coarse compared to the attosecond pulse durations, and quite realistic. Under such stringent conditions, the particular algorithm used to process the spectrogram actually affects the accuracy of the reconstructed attosecond pulses.

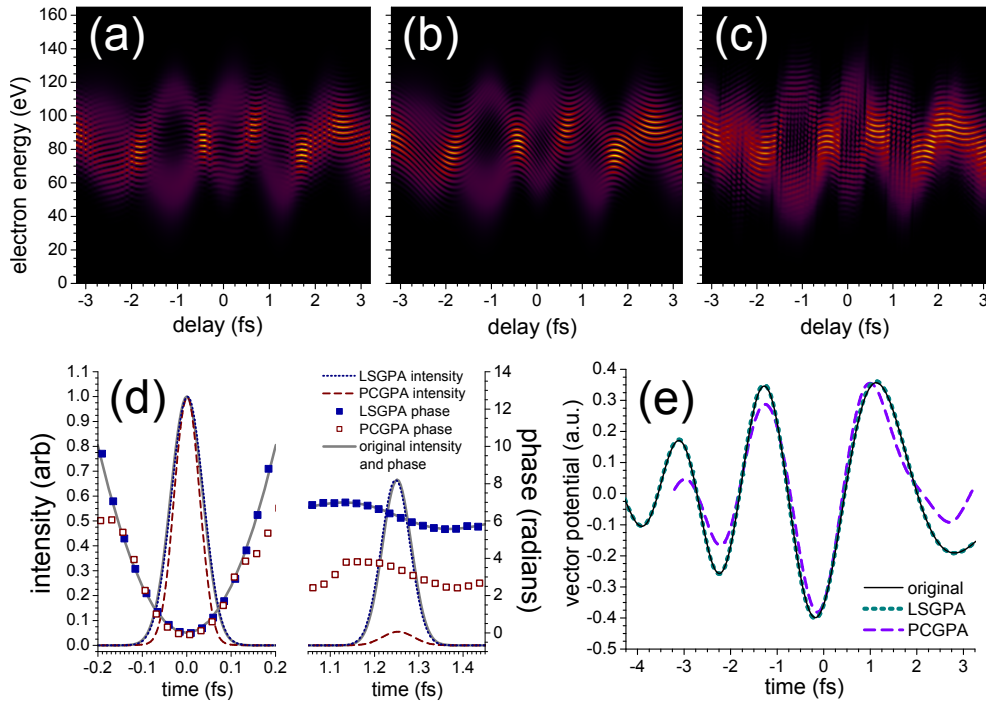


Figure 1.15: The original spectrogram (a) is computed from (1.26a) and (1.26b). It contains a fringe pattern, due to the spectral interference between the two attosecond pulses, which is coarsely sampled with the 100 as delay step. Nevertheless, it contains enough information for the LSGPA to retrieve the full fringe pattern (b). On the other hand, since the PCGPA requires the original spectrogram to be interpolated along the delay axis, it cannot properly reconstruct the fringe pattern, and produces a spectrogram with artifacts (c). Panel (d) shows the attosecond pulses reconstructed by the PCGPA and the LSGPA, as compared to the original one. Panel (e) shows the NIR vector potential reconstructed by the PCGPA and the LSGPA, compared with the original one.

As shown in Figures 1.15-d and 1.15-e, the PCGPA is unable to “understand” the fringe pattern and reproduce the correct spectrogram because the original one had to be

interpolated from 65 up to 256 samples along the delay axis in order to satisfy the sampling relation (1.38). This effectively means that three quarters of the spectrogram processed by the PCGPA consisted of fake spectra! Unsurprisingly, it could not accurately characterize both of the attosecond pulses and the NIR field.

The final spectrogram output by the PCGPA, Figure 1.15-c, displays a checkerboard pattern in the areas where the spectral components of the satellite pulse should appear, and vastly underestimates the power contained in the satellite pulse. Moreover, it also underestimates the main pulse's duration by 20%. These two mistakes are likely related, and might be caused by the PCGPA assigning spectral components of the satellite to the main pulse, thereby artificially increasing the main pulse's bandwidth, and decreasing its duration. Additionally, the vector potential retrieved by the PCGPA is erroneous.

In contrast to the PCGPA, the LSGPA only has to process the original 65 spectra. These 65 spectra contain enough information to characterize both attosecond pulses as well as the NIR field. Figure 1.15-b displays the *full* spectrogram reconstructed by the LSGPA, which contains the spectra that *would have been measured* between the delay steps of the original one, i.e. if a 25 as delay step was used¹⁶. The success of the LSGPA is evidenced by the perfect match between the retrieved and reconstructed fields, as shown in Figures 1.15-d and 1.15-e.

I must emphasize that this example was just meant to show the algorithmic advantages of the LSGPA over the PCGPA—the original spectrogram shown in Figure 1.15-a was computed using the central momentum approximation (CMA), and assumed the transition dipole matrix element $d(p) = 1$. Although I have already established, through TDSE simulations (cf. Figures 1.12 and 1.13), that the CMA is a reliable approximation and that ignoring $d(p)$ does not greatly affect the attosecond pulse retrieval, these examples were based on an *ideal* attosecond streaking measurement—one that contains no uncertainties in the NIR and XUV pulse parameters, nor in the system that is photoionized. In the next section, I examine the effects of various uncertainties that are present in real attosecond streaking experiments, and assess the tolerance of the FROG algorithm against them.

1.7 The Robustness of Attosecond Streaking Measurements

FROG reconstruction is based on the premise that the streaking measurement is performed with a single, unique pair of XUV and NIR fields. Therefore, FROG does not account for shot-to-shot fluctuations in the XUV and NIR parameters, nor does it consider any spatial effects, as none are built into the formalism and algorithms described in the previous

¹⁶Because the LSGPA retrieves \mathbf{P} and \mathbf{G} with a time sample of $\delta t = \delta\tau/L$, a “full” spectrogram can be recalculated from the final (retrieved) pulse and gate via the signal matrix $S_{i,j} = P_j G_{j+(i-1)L}$, assuming $L = 1$. This *full* reconstructed spectrogram, which contains L times more spectra and has a delay sample of $\delta\tau = \delta t$, displays the spectra that lie *in between* those of original spectrogram. Clearly, no type of interpolation can reproduce the full spectrogram in Figure 1.15-b from the original spectrogram in Figure 1.15-a.

sections. Namely, it assumes the streaking measurement is performed on a spatially homogeneous interaction region, and that the spatial XUV [69, 68] and NIR beam profiles are constant. To reach this idealization, one would need to perform a single-shot streaking measurement on a spatially well-confined population of identical systems, e.g. a Bose-Einstein condensate... Actually, even *that* wouldn't work because the ejected electrons would suffer from enormous space-charge effects which are also not included in our model!

In reality, a more rigorous description of the streaking measurement should consider an *ensemble* of NIR and XUV fields¹⁷, to model the various uncertainties present in a realistic streaking experiment. Unfortunately, such a theoretical description is (currently) incompatible with the efficient FROG algorithms described above. Therefore, in this section, I'll show to which extent FROG can be used to analyze a streaking spectrogram which is formed by an ensemble of attosecond XUV pulses with different pulse parameters.

I only consider uncertainties in the XUV pulse parameters because the streaked photoelectron spectra are much more sensitive to XUV parameters than to the NIR ones for typical streaking measurements. My underlying assumption here is that if you can generate harmonics, gate the harmonics to isolate an attosecond pulse, and then perform a streaking measurement with attosecond and NIR fields synchronized on the attosecond time scale, then the stability of your laser pulse is likely not an issue as far as the streaking measurement is concerned!

Furthermore, I do not attempt to model any specific experimental defects, because there are countless ways in which the spectrogram can be affected by experimental imperfections. Instead, I adopt a slightly more abstract but systematic approach, and identify several key parameters of the attosecond pulse that determine the basic properties of the streaking spectrogram. Uncertainties in these parameters may arise from various experimental effects.

I describe the effect of the uncertainty in each in these attosecond pulse parameters on the streaking spectrogram by considering these parameters independently, and assuming that there is some *uncertainty* associated with each of them. I treat all these uncertainties on equal footing. For each parameter, I consider an ensemble of attosecond pulses where only the chosen parameter is varied. A streaking spectrogram is evaluated, using the FROG expression (1.26a), for each of the attosecond pulses in the ensemble. Averaging these spectrograms over the ensemble¹⁸ then gives a spectrogram that embodies the uncertainty.

¹⁷Actually, a yet more general theory would model uncertainty not in the XUV field, but in the photoelectron wave packet. For instance, if a perfectly known attosecond XUV field ejects an electron from the conduction band of a metal [28], then there is an uncertainty in the photoelectron wave packet's central energy because the electron could have been emitted from any energy level within the conduction band. Or, if a perfectly known attosecond pulse ejects an electron from different layers in a solid, then there will be a timing uncertainty in the onset of the streaking effect, which in practice is equivalent to a timing uncertainty of the photoelectron wave packet itself. In these two examples, there is uncertainty in the photoelectron wave packet while the field of the attosecond pulse is completely known with certainty. Nevertheless, a more detailed discussion of photoelectron wave packets is reserved for the next chapter. For the remainder of this one, let's continue to work within the frame of characterizing attosecond pulses; which, in any case, you'd never want to do by streaking a photoelectron emitted from a solid!

¹⁸For simplicity, I assume a uniform distribution for each of the attosecond pulse parameters.

I assess and interpret the influence of these uncertainties on the FROG reconstruction, by processing these averaged spectrograms using the LSGPA.

I consider two relevant scenarios: (i) streaking with an isolated attosecond pulse, and (ii) streaking with a train of two attosecond pulses. For the first scenario, i.e. that of an isolated attosecond pulse, I find that mainly three pulse parameters affect the spectrogram: the central energy of the attosecond pulse, its bandwidth and its GDD. Uncertainties in these three quantities affect the overall shape and definition of the streaking spectrogram. For the second scenario, I focus on the relative parameters between the two attosecond pulses: their relative phase, their relative intensity and their relative timing. Uncertainties these relative pulse parameters affect the fringe pattern of the spectrogram, and thus our ability to properly characterize the satellite pulse. Lastly, for both scenarios the overall timing of the attosecond pulse with respect to the NIR streaking field will also be considered.

1.7.1 Streaking with a Single Isolated Attosecond Pulse

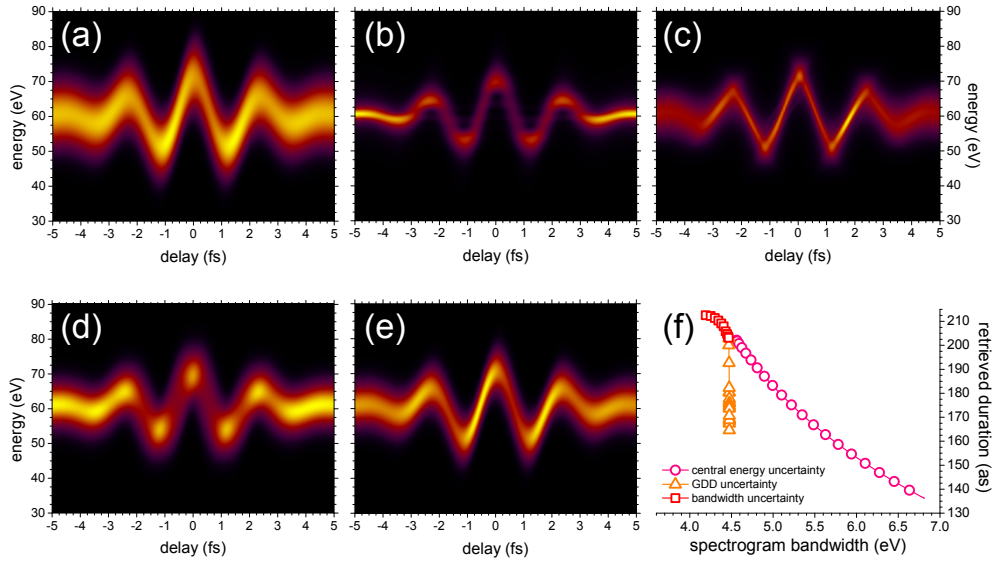


Figure 1.16: These spectrograms show the signatures of uncertainties in key attosecond pulse parameters. They correspond to uncertainties of (a) 15 eV in central energy, (b) 17.5 eV in bandwidth, (c) 100 000 as² in GDD and (d) 900 as in timing (with respect to the NIR streaking field), while (e) shows the original spectrogram without any uncertainties. Panel (f) shows the retrieved XUV pulse duration as a function of the spectrogram's mean bandwidth $\bar{\delta} = \sum_{k=1}^{N_\tau} \sqrt{\langle \varepsilon^2 \rangle_k - \langle \varepsilon \rangle_k^2}$, for uncertainties in bandwidth, central energy and GDD, where $\langle A \rangle_k$ denotes the mean of A over the k -th streaked spectrum.

The uncertainties pertaining to isolated attosecond pulses each leave their own signature on the measured spectrogram, as illustrated in Figures 1.16-a, b, c and d (in comparison with the pure spectrogram shown in Figure 1.16-e). The overall effect of the uncertainties for a single pulse is a smearing and distortion of the spectrogram, and in some cases

(especially apparent in Figures 1.16-a and 1.16-d) a loss of the spectral broadening and narrowing effect at zero-crossings of the vector potential—which is crucial for determining the attosecond pulse’s chirp.

For an isolated pulse, the smearing of the spectrogram results in an overestimation of the bandwidth, and therefore an underestimation of the pulse duration. Figure 1.16-f is a plot of the pulse duration retrieved by the attosecond FROG algorithm as a function of the bandwidth $\bar{\delta}$ of the spectrogram (that contains the uncertainty). I define the spectrogram bandwidth as the average standard deviation of the streaked spectra:

$$\bar{\delta} = \sum_{k=1}^{N_\tau} \sqrt{\langle \varepsilon^2 \rangle_k - \langle \varepsilon \rangle_k^2}, \quad (1.43)$$

where N_τ is the number of streaked spectra. For each of the parameters considered, Figure 1.16-f suggests that the retrieved pulse duration is smaller when the spectrogram is more smeared out. Therefore, a major effect of the uncertainties pertaining to a single pulse is an error in the retrieved pulse duration.

To study the uncertainties for a single isolated attosecond pulse, the XUV and NIR fields are modeled as Gaussians according to

$$F_X^{(1)}(t) = \exp \left(-\ln(4) \left(\frac{t - t_X}{\tau_X} \right)^2 + i \left(\varepsilon_X(t - t_X) + \frac{1}{2} \beta_X(t - t_X)^2 \right) \right) \quad (1.44)$$

$$A_L(t) = A_0 \exp \left(-\ln(4) \left(\frac{t}{\tau_L} \right)^2 \right) \cos(\omega_L t). \quad (1.45)$$

The values of the NIR pulse parameters are $\tau_L \approx 3.3$ fs, $\omega_L \approx 2.616$ rad/fs (corresponding to a wavelength of 720 nm) and $A_0 \approx -0.1878$ a.u. (corresponding to a peak intensity of 5 TW/cm²). The central values of the XUV parameters, i.e. in the absence of any uncertainty, are $\varepsilon_X = 60$ eV, $\tau_X = 200$ as and $\beta_X = 40 \times 10^2$ as⁻² (corresponding to a GDD $\gamma_X \approx 6340$ as²), giving a FWHM bandwidth $\delta_X \approx 10.5$ eV. The attosecond pulse is temporally centered at $t_X = 0$.

These are typical parameters used in attosecond streaking experiments¹⁹. Assuming these central parameter values, I investigate the role of uncertainties in central energy ε_X , bandwidth δ_X and GDD γ_X , as well as in the absolute timing t_X of the attosecond pulse. Each of these uncertainties, whose signatures are displayed in Figure 1.16, adds its unique fingerprint on the spectrogram. In the case of an isolated attosecond pulse, they mainly affect the overall bandwidth of the spectrogram, which correlates to the retrieved duration, as shown in Figure 1.16-f.

Uncertainty in the Central Energy

Let’s first consider variations in the central energy ε_X of the attosecond pulse. Changes in the central energy ε_X might occur due to variations in the laser intensity, which affect

¹⁹They were cutting-edge a few years ago. However, since record 80 as pulses were produced back in 2008, pulses shorter than 100 as are now routinely produced in leading attosecond laboratories

the kinetic energy of the recolliding electrons [125, 36, 123] (and hence the cutoff of the harmonic spectrum).

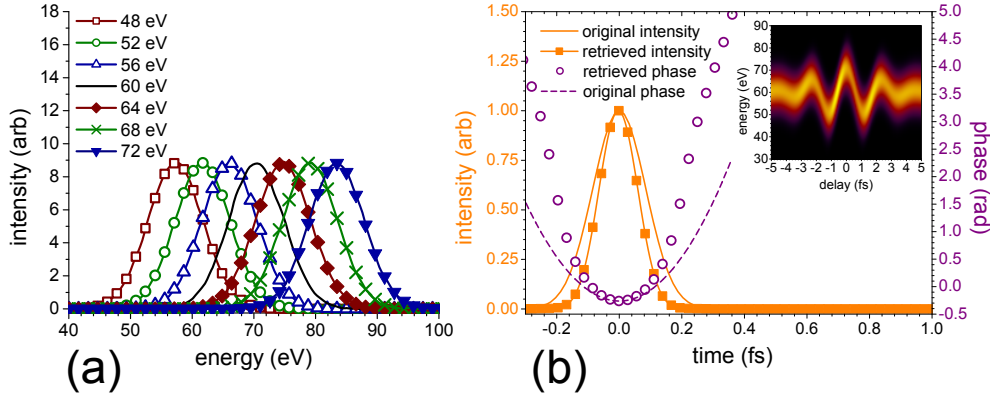


Figure 1.17: (a) Streaked spectra taken at the peak of the vector potential (delay $\tau = 0$) for different central energies; (b) attosecond pulse retrieved by the attosecond FROG algorithm for a central energy uncertainty of 15 eV.

The spatial chirp of the laser beam might also result in variations of the central energy, due to the strong dependence of the ponderomotive energy on wavelength. Figure 1.17-a shows streaked spectra centered at different energies, taken at an XUV-NIR delay $\tau = 0$, showing that ε_X mainly just positions the spectrogram along the energy axis.

The incoherent sum of these streaked spectra clearly produces an artificially broader spectrum, which smears the spectrogram along the energy axis. As a result, the retrieval algorithm overestimates the bandwidth, leading to an underestimation of the pulse duration. The pulse retrieved by the attosecond FROG algorithm is significantly shorter (28%) than the original one, and its temporal phase is somewhat distorted, the chirp being overestimated by 155%.

Uncertainty in the Bandwidth

An uncertainty in the XUV bandwidth δ_X can happen due to overall changes in the laser waveform, particularly the intensity, and can also result from spatial variations in the cutoff energy. The attosecond pulse's bandwidth directly correlates with the bandwidth of the spectrogram, but has little impact on the *averaged* spectrogram. Figure 1.18-a shows plots of streaked spectra taken at a delay $\tau = -T_L/4 \approx -0.600$ fs, where the vector potential is zero but changes approximately linearly in time. In this case, spectral narrowing is most pronounced, as described by (1.11).

In these simulations, I assume a rather large bandwidth uncertainty, corresponding to pulses with durations ranging from 186 as to 3.3 fs. Despite such large bandwidth variations, the quality of the resulting spectrogram is sufficient for an accurate FROG reconstruction, yielding errors in pulse duration and temporal chirp of 11% and 9% respectively. Figure 1.18-b shows that the retrieved temporal phase diverges from the original one where

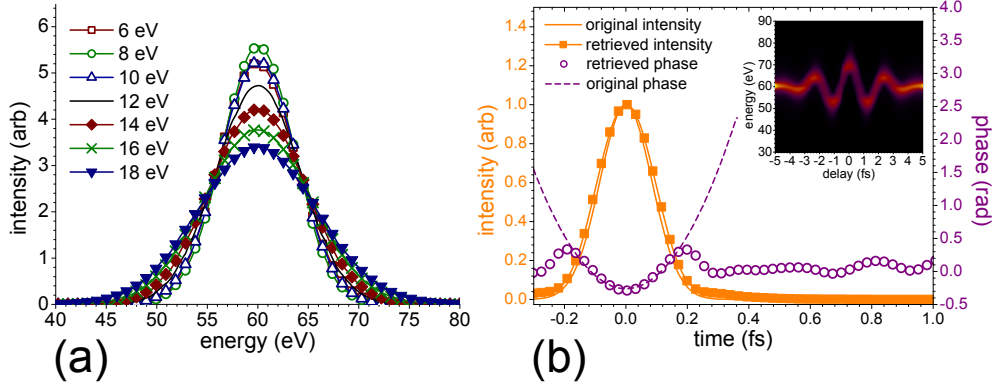


Figure 1.18: (a) Streaked spectra taken at the zero of the vector potential (delay $\tau = -600$ as) for different bandwidths of the attosecond pulse, with $\gamma_X = -6240 \text{ as}^2$; (b) Retrieved attosecond pulse for a bandwidth uncertainty of 17.47 eV.

the intensity is small. This is also the case in most of the other retrievals, and is caused by the fact that the retrieved phase becomes ambiguous at lower intensities [195].

Uncertainty in the Group-Delay Dispersion

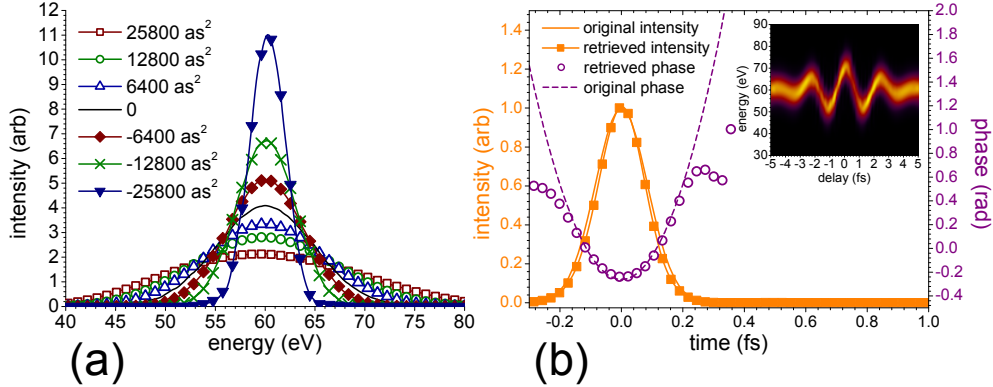


Figure 1.19: (a) Streaked spectra taken at the zero of the vector potential (delay $\tau = -600$ as) for different values of GDD with $\delta_X = 10.5 \text{ eV}$; (b) Retrieved attosecond pulse for a GDD uncertainty of 100 000 as^2 .

The group delay dispersion γ_X of the attosecond pulse is an inherent property of the harmonic generation process [106], which has been shown by measurements [85] to be accurately described by the three step model [36]. The GDD is directly determined by the laser waveform that generates the harmonics. Thus, any changes in the laser field over its spatial profile or from shot to shot, will affect the chirp of the attosecond XUV emission, and hence that of the streaked photoelectron.

Figure 1.19-a shows streaked spectra taken at the zero-crossing of the vector potential, i.e. at the same delay τ as in Figure 1.18. Just like the bandwidth uncertainty, uncertainty in the GDD γ_X has hardly any effect on the streaking measurement: different GDD's will merely change the spectral width, but not the center. Even with an unrealistically large GDD uncertainty of $100\,000\text{ as}^2$, the FROG algorithm was able to recover the correct pulse duration and temporal chirp to within 10% and 21% respectively. Figure 1.19-b shows a slight artifact in the temporal phase at $\sim 0.37\text{ as}$. Again, this is due to the low intensity in that region where the phase is more ambiguous.

Uncertainty in the Timing of an Isolated Attosecond Pulse

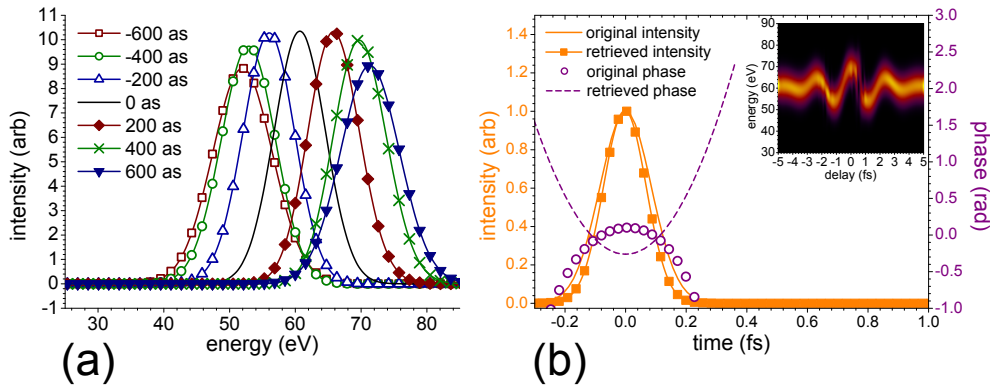


Figure 1.20: (a) Streaked spectra taken at the zero of the vector potential (delay $\tau = -600\text{ as}$) for different timings of the attosecond pulse; (b) Retrieved attosecond pulse for a timing uncertainty of 900 as .

Between the initial moment of harmonic generation and the refocusing on the streaking target, the laser and XUV beams are decoupled in order to induce a delay between them. In some experimental setups [110, 83], the two beams remain collinear. In others [63], the beams might follow a different geometrical path, for example, to convert the NIR field to its third or fifth harmonic. Experimental instabilities may cause jitter between the NIR and XUV beams leading to an uncertainty in t_X . In addition to jitter, the spatio-temporal profile of the XUV beam [69, 68] can also affect the timing precision of the attosecond pulse, whose center in time might depend on the radial position away from the central XUV beam axis.

The moment t_X when the attosecond pulse ejects the electron determines when the electron begins to be streaked, and will in turn determine the position of the spectrogram with respect to the delay axis. This delay uncertainty will therefore introduce an additional smearing effect on the spectrogram, occurring horizontally along the delay axis.

In the simple case of a purely isolated attosecond pulse, this smearing will cause a bandwidth overestimation, and can be responsible for an underestimation of the attosecond pulse's duration. This smearing effect is most pronounced at delays corresponding to the

zero-crossings of the vector potential, where most of the information pertaining to the attosecond chirp is found. For these delays, t_X mainly affects the central energy of the streaked spectra, as shown in Figure 1.20-a. On the other hand, near the peaks of the vector potential the spectral shift is approximately constant to lowest-order, and so the uncertainty in t_X has a minimal effect there.

Figure 1.20-b shows that, for a timing uncertainty of 900 as, the retrieved pulse is 13% shorter than the original one, and the algorithm completely fails to retrieve its chirp due to the smearing of the spectra at the zero-crossings of the vector potential.

In this section, I have presented effects resulting from uncertainties in the pulse parameters of an isolated attosecond pulse. The reconstruction of a single pulse to be generally robust, and mainly suffers when there is a significant amount of *vertical* smearing of the spectrogram—which can occur due to variations in the central energy; or when the relative timing between the NIR and XUV pulses varies—resulting in a *horizontal* smearing of the spectrogram. These effects artificially increasing the bandwidth of the spectrogram, and consequently lead to an underestimation of the retrieved pulse duration. I have also verified the role of uncertainties in the GDD and bandwidth, and found that they have a minimal impact on the spectrogram and the retrieved wave packet. Even when these parameters change by unrealistically large amounts, the attosecond pulse can still be correctly recovered.

1.7.2 Streaking with a Sequence of Two Attosecond Pulses

A streaking spectrogram recorded with a sequence of two coherent attosecond pulses contains a spectral interference pattern. This interference pattern contains all the information about the *relative* properties between the pulses: e.g. their relative phase $\Delta\varphi_X$, their relative timing Δt_X and their relative intensity ΔI_X .

Thus, the spectral fringes are mainly defined by the parameters relative between the two attosecond pulses:

- the fringe position is proportional to the relative phase between the two pulses;
- the fringe spacing is inversely proportional to the time difference between the pulses;
- the fringe visibility (or contrast) is related to the relative intensity between the pulses.

As we will see, the fringe pattern is sensitive to changes in the relative pulse parameters $\Delta\varphi_X$, Δt_X and ΔI_X , and its smearing affects the retrieval of the satellite pulse (defined as the smaller of the two pulses). The signatures of the uncertainties related to double pulses are shown in Figure 1.21. The main effect of uncertainties in $\Delta\varphi_X$, Δt_X and ΔI_X is a smearing and loss of visibility in the fringe pattern.

The quality of the fringe pattern is directly correlated to the accuracy of the satellite pulse's reconstruction. Figure 1.21-f plots the relative intensity of the reconstructed satellite pulse as a function of the fringe contrast of the ensemble-averaged spectrogram, for uncertainties in $\Delta\varphi_X$, Δt_X and ΔI_X . Each curve shows that the intensity of the retrieved

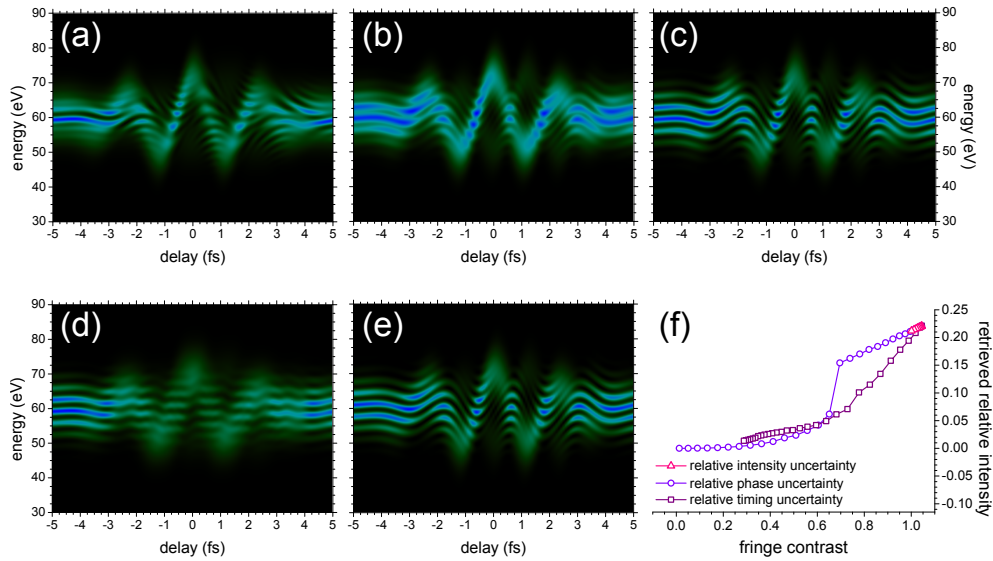


Figure 1.21: Simulated spectrograms for uncertainties in various parameters for a double attosecond pulse: (a) 1.2 fs uncertainty in the relative timing; (b) uncertainty of $3\pi/2$ in the relative phase; (c) 50% uncertainty in the relative intensity; (d) 900 as timing uncertainty; (e) no uncertainty; (f) shows a plot of the retrieved relative intensity between the two pulses versus the fringe contrast in the spectrogram fed to the LSGPA FROG algorithm, for different amounts of uncertainty in the relative phase, timing and intensity between the pulses.

satellite pulse is correlated to the fringe contrast: A reduced fringe contrast leads to an underestimation of the satellite pulse.

While, the uncertainties in relative phase $\Delta\varphi_X$ and relative intensity ΔI_X between the pulses affect the fringe pattern in a similar manner (they reduce the overall fringe contrast), the effect of an uncertainty in the relative timing Δt_X is more complicated, as will be discussed later on.

For the streaking simulations with a double-pulse attosecond field, I model the total attosecond field as

$$F_X^{(2)}(t) = F_X^{(1)}(t) + \sqrt{\Delta I_X} \exp(i\Delta\varphi_X) F_X^{(1)}(t + \Delta t_X), \quad (1.46)$$

where the single pulse field $F_X^{(1)}$ is defined in (1.44), and $\Delta I_X = 0.25$, $\Delta\varphi_X = \pi/2$ and $\Delta t_X = \pi/\omega_L \approx 1.2$ fs, i.e. half a period of the NIR field. The NIR streaking field is the same one used in the previous section, and is thus given by (1.45).

Uncertainty in the Relative Intensity

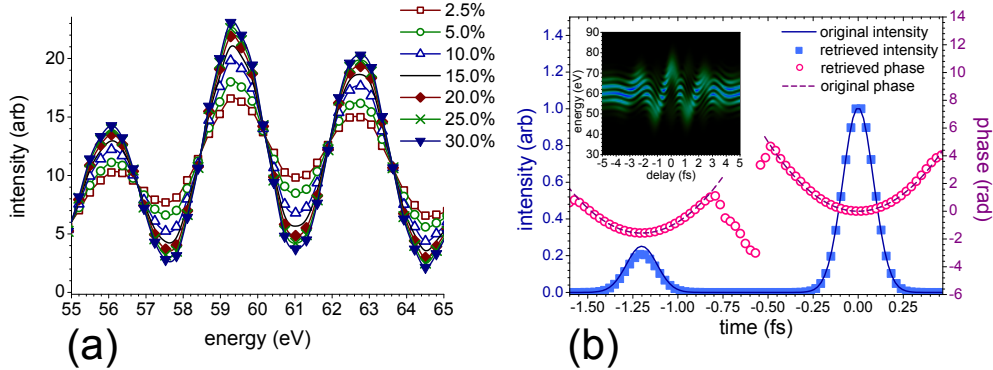


Figure 1.22: (a) Spectra taken at a large XUV-NIR delay $\tau = -5$ fs, where the NIR field is roughly zero, for different values of the relative intensity between the attosecond pulses; (b) Retrieved attosecond pulses for an uncertainty of 50% in the relative intensity.

Since the rate of strong-field ionization is a highly nonlinear function of the electric field [5], the relative contributions to harmonic generation by adjacent half-cycles of the driving field, within a certain spectral range, depend on the parameters of the driving laser pulse (e.g. peak intensity, CEP, chirp). This is especially true for an ultrashort ($\lesssim 3$ fs) driving field [10]. This immediately affects the relative intensity ΔI_X between two consecutive attosecond bursts.

The relative intensity between the attosecond pulses simply changes the fringe modulation depth in the spectrogram: the more the pulses are similar in power, the more the fringe pattern is modulated. Although the modulation depth depends ΔI_X , the positions do not, as shown Figure 1.22-a. This is the case for all XUV-NIR delays τ . Thus, averaging over different values of relative intensity hardly changes the spectrogram, apart from a very

minor loss in fringe visibility as shown in Figure 1.21-c. Even for a large uncertainty of 50% in ΔI_X , the retrieved pulses closely match the original ones, as evidenced in Figure 1.22-b; the satellite being slightly underestimated by $\sim 17\%$, but otherwise properly characterized.

Uncertainty in the Relative Phase

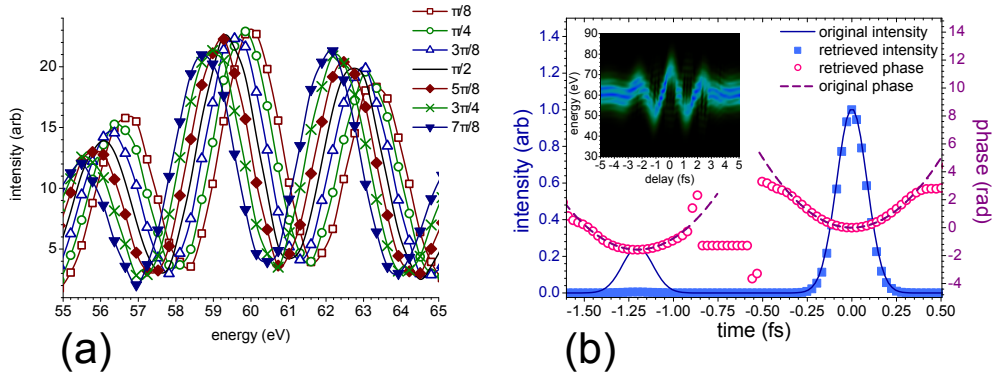


Figure 1.23: (a) Spectra taken at a large XUV-NIR delay $\tau = -5$ fs, where the NIR field is roughly zero, for different values of the relative phase between the attosecond pulses; (b) Retrieved attosecond pulses for an uncertainty of $3\pi/2$ in the phase.

The CEP of attosecond pulses is determined by the laser field that generates the high-order harmonics. It is related to the amount of action accumulated by the recolliding electron during its excursion into the continuum, from the time of its birth until its recollision time. The action the electron accumulates—which depends on the strength, period and overall shape of the laser half-cycle that drives the electron back to the parent ion—gets directly transferred to the phase of the attosecond burst. The CEP of an isolated attosecond pulse has no effect on the streaking spectrogram, and currently does not play a significant role in attosecond science, although a recent theoretical study [149] has been made in this regard. However, the *relative* CEP $\Delta\varphi_X$ between two attosecond pulses in a sequence determines the overall position (along the energy axis) of the interference pattern in the streaking spectrogram.

Thus, the fringe pattern—specifically, its position along the energy axis—carries the information pertaining to the relative CEP (relative phase) between the two attosecond pulses. This relative phase is generally non-zero due to the fact that, for an ultra short driving laser pulse, adjacent half-cycles will not convey the same amount of action to the electron as it is driven back to recollision, thereby producing attosecond bursts of radiation with different phases. The relative phase is therefore sensitive to the laser waveform, and a simple change in laser intensity or laser CEP, for example, will result in a different value of $\Delta\varphi_X$, and will therefore shift the fringe pattern along the energy axis.

As shown in Figure 1.23-a, which plots unstreaked spectra computed for different values of the relative phase, changing $\Delta\varphi_X$ just shifts the fringes along the energy axis, while the delay-dependent behavior of the fringe positions as described by $\Delta\varsigma(\tau)$ (1.33) remains

otherwise unaffected by $\Delta\varphi_X$. Therefore, the net effect of an uncertainty in the relative phase $\Delta\varphi_X$ is just a uniform loss of fringe contrast over the whole spectrogram, as shown in Figure 1.21-b.

Assuming an uncertainty of $3\pi/2$ in the relative phase, Figure 1.23-b shows that the power contained in the reconstructed satellite pulse is underestimated. However, since the fringe pattern only loses contrast but remains otherwise undistorted by the uncertainty, the characterization of the satellite pulse is otherwise accurate: its duration and temporal chirp are correctly retrieved to within 4% and 13%, respectively.

Moreover, the relative phase between the pulses is correctly retrieved, owing to the fact that the fringe pattern that results from ensemble averaging is not shifted with respect to the original one²⁰. On the other hand, if the relative phase is completely unknown, then the fringe pattern disappears, and the satellite is completely unrecoverable. Despite the underestimation of the power in the satellite, the main pulse is still correctly retrieved.

Uncertainty in the Relative Timing

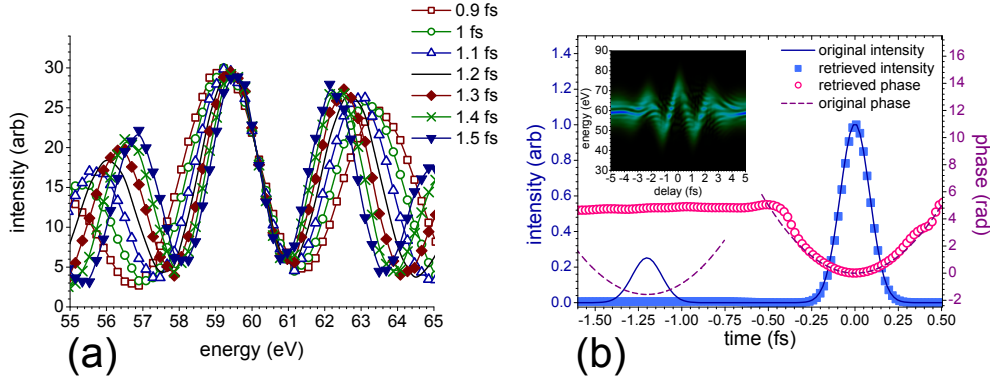


Figure 1.24: (a) Spectra taken at a large XUV-NIR delay $\tau = -5$ fs, where the NIR field is roughly zero, for different values of the relative timing between the attosecond pulses; (b) Retrieved attosecond pulses for an uncertainty of 1.2 fs in the relative timing.

The relative timing Δt_X between the attosecond pulses affects the fringe pattern in a more subtle manner. In addition to the fringe positions, Δt_X affects the spacing of the fringes as well. More generally, it determines the overall delay-dependence of the fringe pattern in the spectrogram, as illustrated in Figure 1.25. Panels (a), (b) and (c) show spectrograms evaluated for three different values of Δt_X (0.9 fs, 1.2 fs and 1.5 fs, respectively). A dotted line is plotted over each spectrogram to indicate the fringe position $\Delta\varsigma/\Delta t_X$ as given by (1.33). These curves are plotted together in Figure 1.25-d, which also shows the center of the streaked spectra— $\varepsilon_S \approx -pA_L(t) + A_L^2(t)/2$ —for comparison. Note

²⁰This finding is actually irrelevant because the spectrograms in this section are simulated using (1.26a). We know, from the analysis of an *ab initio* spectrogram, shown in Figure 1.13, that the relative phase between attosecond pulses cannot be recovered, even without any uncertainties whatsoever.

that for certain delays, where the spectral shift is minimal, the different values of Δt_X yield similar fringe positions. For these delays, the smearing of the fringe pattern should be minimal. This effect has been experimentally observed in [85], where fringes in the spectrogram appear more strongly near the zero-crossings of the vector potential, and disappear when the spectral shift is large.

Integrating over different values of the relative timing Δt_X distorts the fringe pattern in a rather complicated manner, as shown by comparing the spectrogram in Figure 1.21-a to the undistorted one in Figure 1.21-e. As a result of ensemble averaging, the modulation depth of the fringes quickly decreases with the uncertainty in Δt_X (e.g. the relative timing jitter between the pulses), and the fringe spacing is no longer uniform over the spectrogram. Figure 1.24-a, which shows a set of unstreaked spectra calculated for different values of the relative timing, further illustrates that the fringes are quite sensitive to the relative timing. Without the streaking field, only the fringe spacing changes with Δt_X . However, when the streaking field is turned on, the fringe spacing as well as the fringe positions depend on Δt_X , which further deteriorates the fringe pattern, especially for XUV-NIR delays where the spectral shift is the largest.

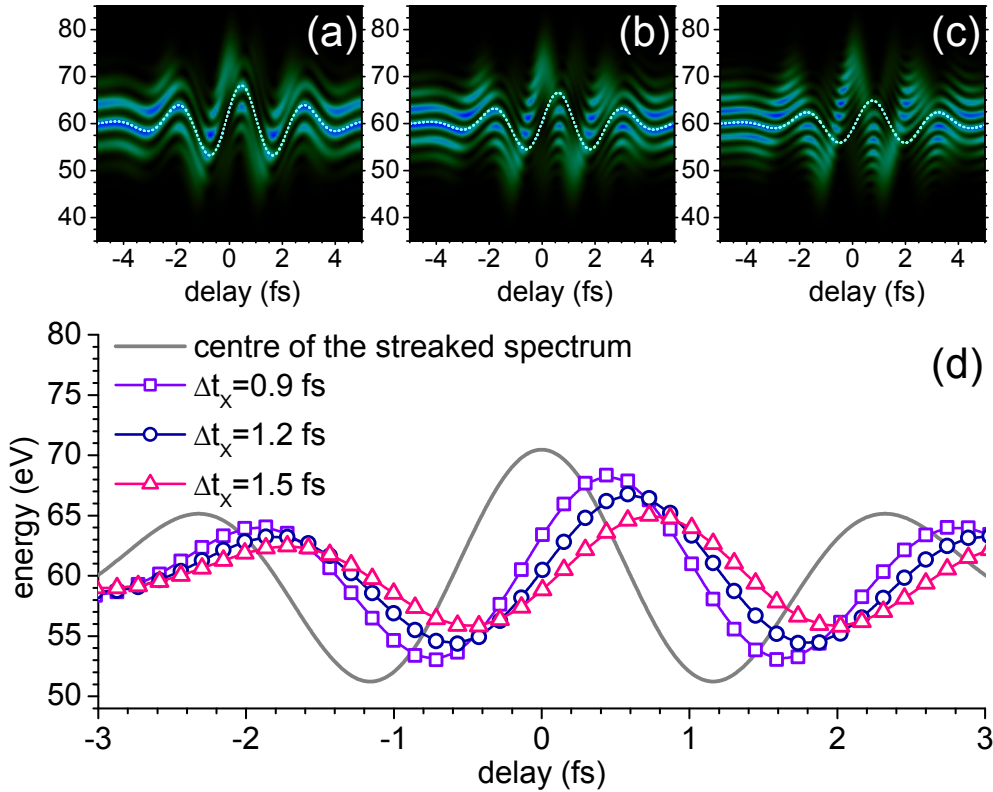


Figure 1.25: Panels (a), (b) and (c) show spectrograms evaluated for relative timings of $\Delta t_X = 0.9$ fs, 1.2 fs and 1.5 fs respectively, the dotted lines represent the fringe positions evaluated using relation (1.33); in panel (d), the center of the streaked spectra, given by (1.6), is plotted together with the fringe positions as a function of XUV-NIR delay τ .

With an uncertainty of 1.2 fs in the relative timing, the retrieval algorithm fails to properly recover the satellite pulse, whereas the main pulse still seems to be accurately characterized (its duration is off by only 6 as) as shown in Figure 1.24-b. Interestingly, the duration of the retrieved satellite is longer than the original, by an amount that is correlated with the uncertainty in the relative timing between the pulses. This suggests that information about the relative timing uncertainty is still somehow embedded in the averaged spectrogram.

Uncertainty in the Timing of a Sequence of Two Attosecond Pulses

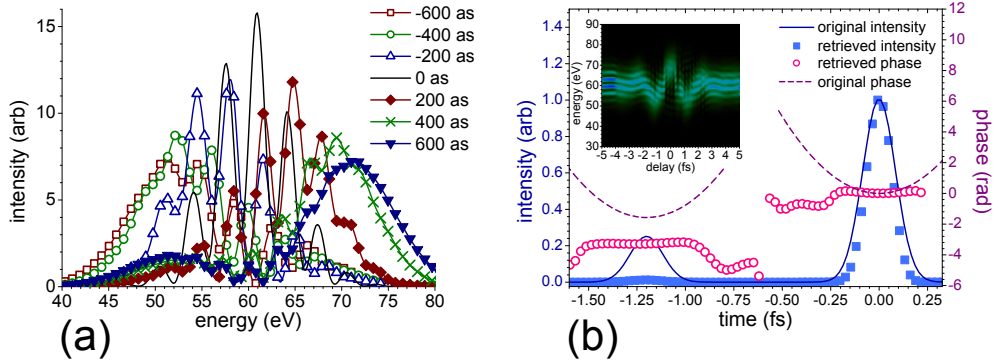


Figure 1.26: (a) Streaked spectra taken at the zero of the vector potential (delay $\tau = -600$ as) for different timings of the attosecond pulse sequence; (b) Retrieved attosecond pulses for a timing uncertainty of 900 as.

Uncertainty in the overall timing t_X of the sequence of attosecond pulses with respect to the NIR field also negatively impacts the fringe pattern, as shown in Figure 1.21-d. When the two attosecond pulses are separated by a half-period of the laser pulse, the fringe pattern varies rapidly near the extrema of the vector potential, and is roughly constant at the zero-crossings. Therefore, an uncertainty in t_X smears the fringes mostly at the delays where the largest spectral shifts occur, and they are better preserved for XUV-NIR delays corresponding to the zero-crossings of the laser's vector potential. Still, Figure 1.26-a shows that spectra taken at the zero-crossing of the vector potential can vary significantly if t_X takes on sufficiently large values away from the mean.

Figure 1.26-b shows that an uncertainty of 900 as in the overall timing t_X prevents the reconstruction of the satellite pulse, and also hampers the characterization of the main pulse. Due to the smearing of the fringes, the power contained in the satellite is greatly underestimated, and the relative phase between the two pulses is not correctly recovered. Also, as a result of the bandwidth overestimation—due to the smearing effects previously described for an uncertainty in t_X in the case of a single attosecond pulse—the main pulse's duration is underestimated by 18% and its retrieved temporal chirp is off by 68%.

As we've seen in this section, the FROG reconstruction is greatly affected by any uncertainties that can smear the fringe pattern in the streaking spectrogram. This is because

the fringe pattern is highly sensitive to various uncertainties in relative parameters between the pulses—particularly in the relative phase $\Delta\varphi_X$ and relative timing Δt_X between the pulses, as well as in the overall timing t_X of the attosecond pulse sequence. On the other hand, the uncertainty in the relative intensity ΔI_X hardly affects the fringe pattern, and therefore the FROG reconstruction. As a result of these effects, the accurate FROG reconstruction of two attosecond pulses in a sequence is generally not possible. Nonetheless, the presence of a small satellite does not hinder the accurate retrieval of the main pulse.

Currently, there are no general methods that can analyze spectrograms which are significantly distorted by uncertainties. However, our results indicate that spectrograms contain enough information to identify, and maybe even quantify the most important uncertainties. For instance, Figures 1.16 and 1.21 show that the main uncertainties in the attosecond pulse parameters each give their own fingerprint on the measured spectrogram. This calls for the development of new analysis techniques based on more realistic models of attosecond streaking measurements.

Chapter 2

Measuring Attosecond Electron Wave Parcels

Up to now, we have been concerned with the characterization of attosecond pulses from streaking measurements on systems whose spectral response $d(p)$ to photoionization is approximately uniform with respect to momentum p , such that $d(p)$ can be ignored and the photoelectron can be viewed as a replica of the attosecond pulse $F_X(t)$. Under these circumstances, measuring the photoelectron replica is tantamount to measuring the attosecond pulse. But then, when the spectral response is not uniform, such that the outgoing electron cannot be viewed as a 1 : 1 replica of the attosecond pulse, what exactly is being measured?

In Section 2.1 of this chapter, we will see that the FROG analysis of attosecond streaking measurements actually provides information about the electron wave packet, including its phase, and can be used as a means to measure and time-resolve the phase of transition dipole matrix elements. In Section 2.2, I consider a situation where the CVA breaks down and FROG cannot be used. In this case, I show that information about the electron wave packet can still be accessed via laser-dressed photoionization measurements, by introducing a new model based on laser-dressed electron trajectories to describe the outgoing electron.

2.1 The FROG Characterization of an Attosecond Electron Wave Parcel from a Streaking Measurement

The term “electron replica” has been thrown around quite often in the attosecond science community during the past few years [35, 97, 107, 171, 37, 216, 57], particularly since the attosecond streak camera came to the forefront [96, 110] as one of the main techniques to be used in attosecond metrology. This “electron replica”, or “electron wave packet”, was loosely defined in [134] as $w(t) = d(p)F_X(t)$, and then it was immediately swept under the rug. The expression $d(p)F_X(t)$ was ostensibly deduced directly from the master equation (1.23a) with the streaking field turned off ($\mathbf{A}_L(t) = 0$). Such a designation of the wave packet, as the quantity reconstructed by FROG, is not satisfactory because it is a function of both momentum and time.

Since the FROG recovers a quantity that depends explicitly only on time, and which is independent of the laser field $A_L(t)$, the “wave packet” reconstructed by FROG should also have these properties: it should be strictly time-dependent, while also embodying the non-uniform spectral response $d(p)$ of the system undergoing photoionization.

In the current section, I first present a rigorous description of a quantity that possesses these aforementioned properties. This quantity is related to the electron wave packet—I call it a *wave parcel*. I show, using numerical and analytical arguments, that the wave parcel is the quantity that FROG actually reconstructs from an attosecond streaking measurement.

To begin, let’s first consider the general case of a free electron wave packet that is formed, somehow, at some initial time t_0 . Such a wave packet can be represented as a superposition of positive-energy eigenstates $|\phi_{\mathbf{p}}\rangle$ of a Hamiltonian $H_0 = p^2/2 + V(\mathbf{r})$ (with eigenvalues ε):

$$|\psi(t_0)\rangle = \int d^3p \langle\phi_{\mathbf{p}}|\psi(t_0)\rangle |\phi_{\mathbf{p}}\rangle. \quad (2.1)$$

Let’s now limit ourselves to a purely energy-resolved measurement, where the direction of $\hat{\mathbf{\Omega}}$ observation $\mathbf{p}/|\mathbf{p}| = \hat{\mathbf{\Omega}} = \sin\theta(\cos\phi\hat{\mathbf{x}} + \sin\phi\hat{\mathbf{y}}) + \cos\theta\hat{\mathbf{z}}$ is fixed. Then we may label the positive-energy eigenstates as $|\phi_{\varepsilon,\hat{\mathbf{\Omega}}}\rangle$, and the coefficients $\langle\phi_{\varepsilon,\hat{\mathbf{\Omega}}}|\psi(t_0)\rangle$ give the probability amplitude of measuring the electron with energy $\varepsilon = |\mathbf{p}|^2/2$ at the detector, placed in the direction $\hat{\mathbf{\Omega}}$ infinitely far from the interaction region. Having fixed the direction of observation, we may now represent the wave packet as

$$|\psi(t_0)\rangle = \int_0^\infty d\varepsilon e^{-i\varepsilon t_0} \langle\phi_{\varepsilon,\hat{\mathbf{\Omega}}}|\psi(t_0)\rangle |\phi_{\varepsilon,\hat{\mathbf{\Omega}}}\rangle, \quad (2.2)$$

which evolves, according to the TDSE, to the state

$$|\psi(t_f)\rangle = \int_0^\infty d\varepsilon e^{-i\varepsilon t_f} \langle\phi_{\varepsilon,\hat{\mathbf{\Omega}}}|\psi(t_0)\rangle |\phi_{\varepsilon,\hat{\mathbf{\Omega}}}\rangle \quad (2.3)$$

at some later time t_f . In the position representation, (2.3) describes the usual quantum-mechanical dispersion of the wave packet due to Heisenberg’s uncertainty principle. It is clear from this expression that $\tilde{\varpi}(\varepsilon) = e^{i\varepsilon t_f} \langle\phi_{\varepsilon,\hat{\mathbf{\Omega}}}|\psi(t_f)\rangle$ is independent of the final observation time t_f . I call the one-sided inverse Fourier transform of $\tilde{\varpi}(\varepsilon)$,

$$\varpi(t) = \frac{1}{2\pi} \int_0^\infty \langle\varepsilon, \hat{\mathbf{\Omega}}|\psi(t_f)\rangle e^{-i\varepsilon(t-t_f)} d\varepsilon, \quad (2.4)$$

the *wave parcel*. The wave parcel $\varpi(t)$ embodies the properties of the wave packet $\langle\varepsilon, \hat{\mathbf{\Omega}}|\psi(t_f)\rangle$, but does not depend on the final time of measurement t_f ¹.

Up to this point, the definition of the wave parcel is general, in the sense that no assumption has been made about the wave packet’s origin. We have simply defined the wave parcel in relation to a free electron wave packet (a wave packet that contains projections

¹The wave parcel doesn’t spread as a function of time, just as you hope for your mail parcel.

only onto positive-energy eigenstates), ignoring how it was formed. Let's now be more specific, and consider the electron wave packet to be formed by an attosecond pulse $F_X(t)$, and measured at some final time t_f . Such a wave packet is given, up to a constant phase, by

$$\langle \phi_{\varepsilon, \hat{\Omega}}^{(-)} | \psi(t_f) \rangle = e^{-i\varepsilon t_f} D(\varepsilon, \hat{\Omega}) \int_{-\infty}^{t_f} F_X(t) e^{i(\varepsilon+W)t} dt, \quad (2.5)$$

where W is the ionization energy of the system, and the transition dipole matrix element $D(\varepsilon, \hat{\Omega}) = \langle \phi_{\varepsilon, \hat{\Omega}}^{(-)} | \mathbf{r} \cdot \hat{\mathbf{n}}_X | \psi_0 \rangle$ describes a bound-free dipole transition from an initial bound state $|\psi_0\rangle$ to a final state $\langle \phi_{\varepsilon, \hat{\Omega}}^{(-)}|$ —an incoming-type positive-energy scattering state of the field-free Hamiltonian $H_0 = p^2/2 + V(\mathbf{r})$ with eigenvalue ε . The scattering state $|\phi_{\varepsilon, \hat{\Omega}}^{(-)}\rangle$ turns into a plane wave, $\langle \mathbf{r} | \varepsilon, \hat{\Omega} \rangle = e^{i\sqrt{2\varepsilon}\hat{\Omega}\cdot\mathbf{r}}$ as $|\mathbf{r}| \rightarrow \infty$ (cf. Section 1.5 and Appendix A.1). Because the electron is described by a free wave packet, i.e. one that contains projections only on positive-energy states, the probability of finding it in some vicinity near the interaction region decreases with time. Therefore, $\left| \langle \phi_{\varepsilon, \hat{\Omega}}^{(-)} | \psi(t_f) \rangle \right| \rightarrow \left| \langle \varepsilon, \hat{\Omega} | \psi(t_f) \rangle \right|$ as $t_f \rightarrow \infty$. In other words, provided that t_f is large enough, projecting $|\psi(t_f)\rangle$ onto plane waves or onto scattering states gives the same result.

Expression (2.5) describes the probability amplitude of measuring a photoelectron with momentum \mathbf{p} at the detector, assumed to be infinitely far from the interaction region. It follows from (1.17) by assuming that the XUV field does not drive free-free transitions ($F_X(t) \langle \phi_{\varepsilon, \hat{\Omega}}^{(-)} | \mathbf{r} \cdot \hat{\mathbf{n}}_X | \phi_{\varepsilon', \hat{\Omega}'}^{(-)} \rangle \approx 0$), which is a very good approximation for current attosecond pulse intensities and photon energies.

Now, because the attosecond pulse is compact in time, at some moment $t_f = t_0$ the value of the integral in (2.5) stops depending on the upper bound of integration. At this point t_0 , we can say that the wave packet is *completely formed* by the attosecond pulse, since the only remaining time dependence in (2.5) is trivial: it is due to the exponential pre-factor $e^{-i\varepsilon t_f}$ which describes the spatial spread of the wave packet.

From (2.4) and (2.5), the wave parcel in the case of single-photon ionization can be written as

$$\varpi(t) = \frac{1}{2\pi} \int_0^\infty D(\varepsilon, \hat{\Omega}) \tilde{F}_X(\varepsilon + W) e^{-i\varepsilon t} d\varepsilon, \quad (2.6)$$

where $\tilde{F}_X(\varepsilon + W)$ is the Fourier transform of the XUV field, evaluated at an energy shifted by the ionization potential W . The wave parcel $\varpi(t)$ given by (2.6) includes the properties of the attosecond pulse as well as the effect of $D(\varepsilon, \hat{\Omega})$, the dipole response of the system, yet it depends explicitly only on time. As we will see in the following example, it turns out that $\varpi(t)$ is precisely the quantity that is recovered from the FROG analysis of an attosecond streaking spectrogram.

Consider a streaking measurement performed with a bandwidth-limited Gaussian XUV pulse, centered at a photon energy of 140 eV and with a FWHM bandwidth of 15 eV,

yielding a FWHM duration of ~ 123 as. The streaking field is a 3 fs FWHM laser pulse with a central wavelength of 800 nm and a peak intensity of 25 TW/cm^2 . I assume the NIR and XUV fields to be linearly polarized in the direction of electron observation, so that $\mathbf{p} = p = \sqrt{2\varepsilon}$, $\mathbf{A}_L(t) = A_L(t)$ and $D(\varepsilon, \hat{\Omega}) = D(\varepsilon)$. The attosecond pulse ejects an electron in the presence of a NIR streaking field, from a system with an ionization energy $W \approx 59 \text{ eV}$ and a non-uniform dipole response. The matrix elements $d(p) = D(\varepsilon)$ for this system (plotted in Figure 2.1-b) are defined by

$$d(p) = (p - p_1)^2/p^3 - i(p - p_2)p^2, \quad (2.7)$$

with $p_1 = 2.974 \text{ a.u.}$ ($\sim 120 \text{ eV}$) and $p_2 = 2.474 \text{ a.u.}$ ($\sim 83 \text{ eV}$).

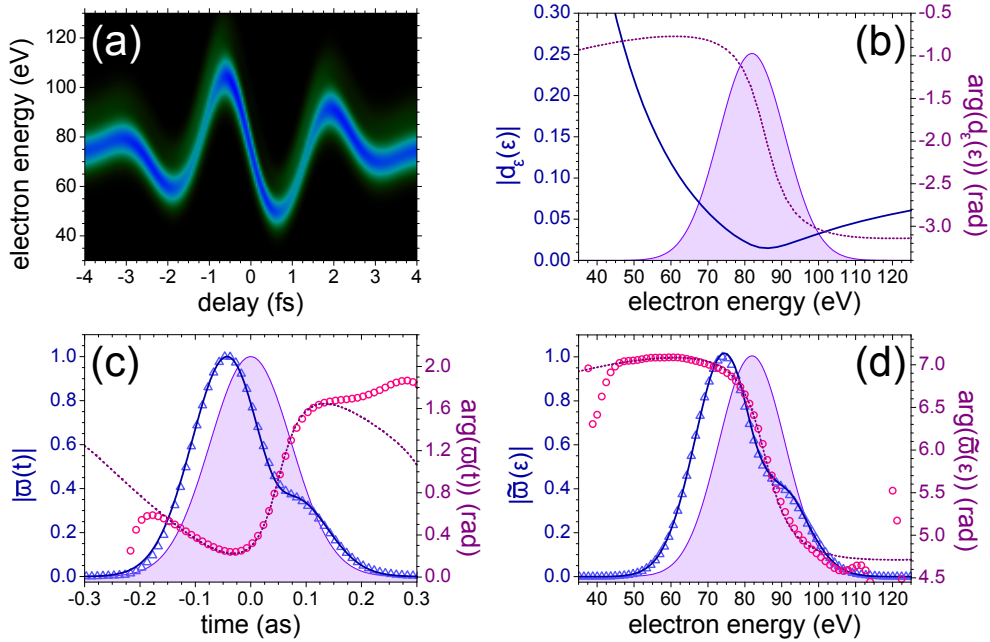


Figure 2.1: Panel (a) shows a spectrogram evaluated within the CVA (1.23a) using transition dipole matrix elements plotted in panel (b). The modulus $|D(\varepsilon)|$ (solid line) and phase $\arg(D(\varepsilon))$ (dotted line) of the transition dipole matrix elements are plotted as a function of electron energy $\varepsilon = p^2/2$ ($D(\varepsilon) = d(p)$). In panels (c) and (d), the modulus (solid lines) and phase (dotted lines) of the exact wave parcel are plotted together with the modulus (triangles) and phase (circles) of the retrieved wave parcel, in the time domain (c) and in the spectral domain (d). The shaded area in panel (c) shows the temporal envelope of the attosecond pulse, while the shaded areas in panels (b) and (d) show the attosecond pulse's Fourier transform (for positive frequencies), shifted by the ionization energy W . According to (2.5), the wave packet results from a modulation of the XUV spectrum by the transition dipole matrix elements.

The streaking spectrogram, shown in Figure 2.1-a, is computed within the CVA (1.23a) using the matrix elements (2.7), plotted in Figure 2.1-b. Although the attosecond pulse is

not chirped, the spectrogram shows a significant amount of broadening and narrowing of streaked spectra at adjacent zero-crossings of the vector potential.

Naturally, the FROG algorithm interprets this effect as chirp, and recovers a temporal profile that is not bandwidth-limited (the retrieved temporal phase is plotted with circles in Figure 2.1-c). Moreover, it recovers a temporal envelope (plotted as triangles in Figure 2.1-c) which is clearly different from the attosecond pulse's Gaussian profile. The retrieved temporal profile is actually that of the wave parcel $\varpi(t)$, whose modulus and phase are plotted with solid and dotted lines, respectively, in Figure 2.1-c. The wave parcel is calculated straightforwardly using relation (2.6).

As shown in Figure 2.1-d, the complex spectral response of the system is directly imprinted on the outgoing electron. Since the spectral amplitude of the wave parcel is just the XUV spectral amplitude modulated by $|D(\varepsilon)|$, and because the XUV spectrum is bandwidth-limited, the spectral phase of $\tilde{\varpi}(\varepsilon)$ is the same as the phase of the matrix elements $D(\varepsilon)$.

To understand why FROG manages to characterize such a fundamental physical quantity as the wave parcel², we now take a closer look at the role of the transition dipole matrix element³ $d(p + A_L(t + \tau))$. Recall that the template for a FROG spectrogram is

$$I(\omega, \tau) = \left| \int_{-\infty}^{\infty} P(t) G(t + \tau) e^{i\omega t} dt \right|^2, \quad (2.8)$$

while the Coulomb-Volkov approximation reads

$$I(p, \tau) = \left| \int_{-\infty}^{\infty} F_X(t) d(p + A_L(t + \tau)) e^{i\phi_L(t+\tau, p)} e^{i(p^2/2 + W)t} dt \right|^2, \quad (2.9a)$$

$$\phi_L(t + \tau, p) = - \int_{t+\tau}^{\infty} \left(p A_L(t') + \frac{1}{2} A_L^2(t') \right) dt'. \quad (2.9b)$$

In our initial attempt to interpret (2.9a) as a FROG spectrogram following the prescription given by (2.8), we completely neglected $d(p + A_L(t + \tau))$ and applied the central-momentum approximation (CMA), which consist of substituting $p \rightarrow p_C - A_L(\tau)$ (p_C being the central momentum of the unstreaked spectrum). As a result, we ended up with expression (1.26a), where the XUV and NIR fields are factored into pulse $P(t) = F_X(t)$ and gate $G(t) = e^{i\phi_L(t)}$ contributions, respectively.

To incorporate $d(p + A_L(t + \tau))$ into the FROG formalism, we note that it explicitly depends on the NIR field through $A_L(t)$. Therefore, it is tempting to just keep the pulse as the XUV field, $P_1(t) = F_X(t)$, and include this dipole matrix element into a “corrected” gate function

$$G_1(t) = d(p + A_L(t)) e^{-i \int_t^{\infty} (p A_L(t') + \frac{1}{2} A_L^2(t') dt')}. \quad (2.10)$$

²The FROG algorithm could have just as well yielded a quantity that resembles the attosecond pulse, but which is otherwise physically irrelevant.

³For this analysis, let's keep the simple experimental geometry described above: NIR and XUV fields are linearly polarized in the direction of observation. Therefore, $d(\mathbf{p} + \mathbf{A}_L(t + \tau)) = d(p + A_L(t + \tau))$, and $\mathbf{p} \cdot \mathbf{A}_L(t) = p A_L(t)$.

However, we know that the FROG algorithm, when applied to a streaking spectrogram, does not factor the pulse and gate in this manner. This suggests that, instead of the factorization $P_1(t)G_1(t+\tau)$, there is a more appropriate factorization $P_2(t)G_2(t+\tau)$ of the integrand into functions $P_2(t)$ and $G_2(t)$, both of which exhibit a weaker dependence on momentum p , and thereby render the CMA ($p \rightarrow p_S = p_C - A_L(\tau)$) less harmful. Thus, we seek a better pair of functions $P_2(t)$ and $G_2(t)$.

Instead of just tacking $d(p + A_L(t + \tau))$ onto the Volkov phase factor as is done in (2.10) in order to produce the gate $G_1(t)$, the effect of the dipole response can be treated more subtly. First, we can use (2.6) to represent $F_X(t)$ in terms of the wave parcel, leading to

$$I(p, \tau) = \left| \int_{-\infty}^{\infty} \left(\frac{1}{2\pi} \int_0^{\infty} \tilde{\omega}(\varepsilon') \left(\frac{d(p')}{d(p_i)} \right)^{-1} e^{-i\varepsilon' t} d\varepsilon' \right) e^{i\phi_L(t+\tau, p)} e^{i(p^2/2+W)t} dt \right|^2, \quad (2.11a)$$

$$\text{where } p_i = p + A_L(t + \tau) \quad (2.11b)$$

is the initial momentum of the electron and $p' = \sqrt{2\varepsilon'}$. Since the Fourier-space wave parcel $\tilde{\omega}(\varepsilon')$ represents the photoelectron's energy content *prior* to the onset of streaking, it is appropriate to expand the transition dipole matrix element $d(p')$ into a Taylor series about the initial momentum p_i , such that the ratio of matrix elements can be written as

$$\frac{d(p')}{d(p_i)} = \sum_{n=0}^{\infty} \frac{1}{n!} \frac{d^{(n)}(p_i)}{d(p_i)} (p' - p_i)^n = 1 + \frac{d'(p_i)}{d(p_i)} (p' - p_i) + \frac{1}{2} \frac{d''(p_i)}{d(p_i)} (p' - p_i)^2 + \dots \quad (2.12)$$

If $d(p)$ is sufficiently well-behaved within the wave parcel's bandwidth, then (2.12) shows that, to leading order, the ratio $d(p')/d(p_i)$ is constant, i.e. it does not depend on the initial momentum p_i . In writing out the Taylor series expansion (2.12), we have not yet made use of the CMA: this expansion is performed about the initial momentum variable $p_i = p + A_L(t + \tau)$. We find that the leading-order term in the series exhibits no dependence on p_i *prior to* applying the CMA.

In truncating the series (2.12) after the first term, we neglect higher-order dependence on p_i , but we don't altogether neglect the momentum-dependence of $d(p_i)$: it is contained in the wave parcel components $\tilde{\omega}(\varepsilon')$. In contrast, applying the CMA directly to $d(p_i) = d(p + A_L(t + \tau))$ is much more harmful, as it completely neglects any momentum dependence of the transition dipole matrix element.

Keeping only the first term of (2.12), (2.11a) can be approximated as

$$I(p, \tau) \approx \left| \int_{-\infty}^{\infty} \varpi(t) e^{i\phi_L(t+\tau, p)} e^{i(p^2/2+W)t} dt \right|^2, \quad (2.13)$$

which is a FROG spectrogram with a factorization $P_2(t)G_2(t + \tau)$, where the pulse and gate functions are now

$$P_2(t) = \varpi(t) \quad (2.14a)$$

$$G_2(t) = e^{-i \int_t^{\infty} (p A_L(t') + \frac{1}{2} A_L^2(t')) dt'}. \quad (2.14b)$$

Although the gate $G_2(t)$ in this version of the attosecond streaking spectrogram is exactly the same as the one previously used for the FROG reconstruction of attosecond pulses, its modulus is found to be constant ($|G_2(t)| = 1$) without actually ignoring the momentum dependence of the dipole response $d(p)$, which is implicitly contained in the wave parcel $\varpi(t)$. Since the integrand of (2.13) does not depend explicitly on $d(p)$, it is more robust than (2.9a) against the CMA. In other words, the non-uniform dipole response $d(p)$ is still preserved after applying the CMA to (2.13).

This finding [212] has significant implications for the attosecond streaking technique. Namely, it means that attosecond streaking can be used to monitor, with attosecond temporal resolution, the energy-dependant *phase* of transition dipole matrix elements of a quantum system undergoing dynamics. This can be achieved, for instance, in a time-resolved measurement using three pulses.

A pump pulse is first used to launch ultrafast dynamics in some system, which is then probed by the combined field of an attosecond XUV pulse and a femtosecond NIR pulse; the former one used to photoionize the system and the latter one to streak the outgoing photoelectron wave packet. Thus, for each pump-probe delay τ_P (representing the delay between the attosecond pulse and the pump pulse), a streaking spectrogram is recorded and then processed to obtain the wave parcel $\varpi(t; \tau_P)$, which obviously depends on the time τ_P when it was ejected. If the attosecond pulse field $F_X(t)$ is simultaneously characterized, e.g. by performing a streaking measurement in parallel on a system with a nearly constant $d(p)$ (such as a rare-gas atom), then the instantaneous transition dipole matrix elements $d(p; \tau_P)$ may be extracted from the system undergoing ultrafast dynamics, using the relation (2.6).

In this section, we've seen how the wave parcel, which embodies key information about an electron wave packet, can be characterized via the FROG analysis of an attosecond streaking measurement. However, the attosecond FROG relies on the validity of the CVA (1.23a). In the next section, I will consider a situation where the wave packet is re-scattered in the presence of a NIR field as it exits a spatially extended system. In this case, the CVA breaks down and so FROG analysis cannot be applied to recover the wave parcel. Nevertheless, it turns out that the wave parcel—a dispersion-compensated version of the electron wave packet—is still a useful concept to explain this phenomenon.

2.2 Laser-Dressed Scattering of an Attosecond Electron Wave Packet

In this section, I theoretically study how a laser field affects the scattering of an attosecond electron wave packet as it travels inside a spatially extended system. Experimentally, this can be realized by ionizing a localized electronic state of a molecule with an attosecond extreme-ultraviolet (XUV) pulse. As it exits the molecule, the photoelectron will be scattered by other atoms in the molecule before heading to the detector.

The scattering of a photoelectron within a molecule has recently attracted a significant amount attention on its own: in addition to the Cohen-Fano oscillations [32], ionization

from a localized core orbital of CO also produces a modulation in the momentum-resolved cross-sections [218] arising from the interference between trajectories taken by the outgoing electron, referred to as *intra-molecular scattering*. The interference pattern produced at the detector can be interpreted as a holographic image [118], and can be used to retrieve the molecular structure seen by the outgoing electron. In this section, I show that a near-infrared (NIR) laser wave form, temporally synchronized to the collision event, can be used to control the paths taken by the outgoing photoelectron, which can be observed in the interference of the laser-dressed photoelectron spectrum.

Up to now, we have been concerned with attosecond streaking experiments performed on an atom, which is spatially localized. For such a system, the Coulomb-Volkov approximation (CVA) works well, because the laser field barely distorts the ionic potential⁴ and the field-free scattering states form a suitable basis of final states used in the evaluation of bound-free transition dipole matrix elements.

On the other hand, if the system is too large, field-free continuum states $|\phi_{\mathbf{p}}^{(-)}\rangle$ can no longer be used to represent the photoelectron's laser-driven motion in the potential. Since the CVA relies on these field-free continuum states, it cannot explain the scattering of the outgoing electron by the ionic potential in the presence of the laser field. And because of the failure of the CVA, the FROG algorithm cannot be used to characterize the photoelectron wave packet. To fill the void caused by this failure, I introduce a new model that explains the laser-dressed photoionization of such a spatially extended system, by considering billiard ball trajectories taken by the outgoing electron. This “billiard ball” model explains the main effects of laser-dressed photoelectron scattering, observed as changes in the measured photoelectron spectrum due to the laser field.

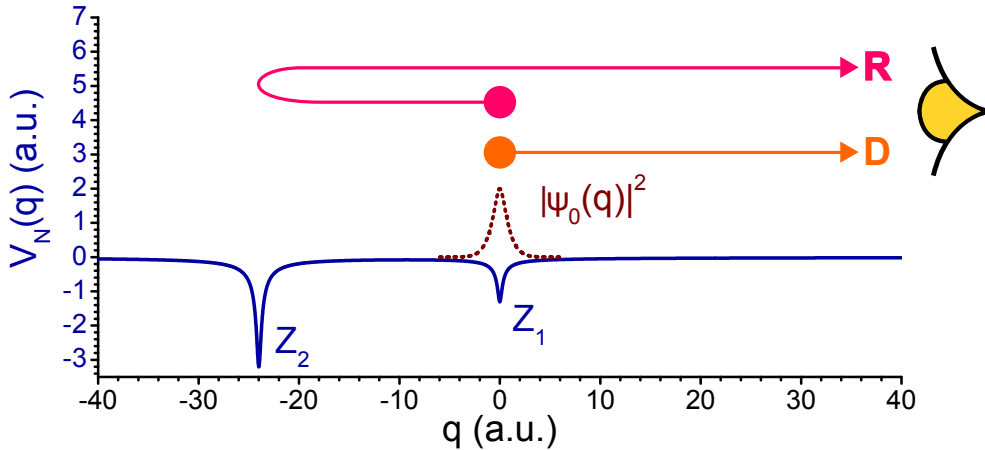


Figure 2.2: The ionic potential (solid line) dips at positions $q = 0$ and $q = -24$ a.u. The initial state (dotted line) is localized at $q = 0$. The outgoing electron can follow two trajectories, labeled with “R” and “D”.

⁴In the length gauge, and within the dipole approximation, the NIR laser field $F_L(t)$ adds an interaction term $\mathbf{F}_L(t) \cdot \mathbf{r}$ to the Hamiltonian, which is just a potential with a constant gradient.

Let's consider a one-dimensional model system, akin to a nanometer-scale Fabry-Pérot etalon for the free electron wave packet, as shown in Figure 2.2. The system is composed of two potential wells chosen such that the electron is initially localized in one of them. The initial (bound) state $|\psi_0\rangle$ is the first excited state of the double-well system (ionization potential $W \approx 12.17$ eV). The Hamiltonian of the electron interacting with the potentials and the electromagnetic radiation, assuming the dipole approximation, is

$$H = \frac{p^2}{2} + V_N(q) + \left(F_L(t) + F_X(t) \right) q, \quad (2.15a)$$

$$V_N(q) = \frac{1}{Z_1 + Z_2} \left(-\frac{Z_1}{\sqrt{q^2 + a^2}} - \frac{Z_2}{\sqrt{(q - q_r)^2 + a^2}} \right) \quad (2.15b)$$

with $a \approx 0.2236$ a.u., $q_r = -24$ a.u., $Z_1 = 2$ a.u. and $Z_2 = 5$ a.u. p is the electron's momentum, $V_N(q)$ is the potential due to the nuclei, with nuclear charges Z_1 and Z_2 . $F_L(t)$ and $F_X(t)$ represent the electric fields of the NIR laser and attosecond XUV pulses, respectively. They are given explicitly by

$$F_X(t) = 10^{-5} \int_{-\infty}^{\infty} G_{\kappa, \theta}(\omega - W) \cos(\omega t) d\omega, \quad (2.16a)$$

$$F_L(t) = -\frac{d}{dt} \left(\frac{F_0}{\omega_L} \cos^4 \left(\frac{\pi t}{2\tau_L} \right) \sin(\omega_L t) \right), \quad |t| \leq \tau_L, \quad (2.16b)$$

while $F_L = 0$ for $|t| > \tau_L$. The XUV spectrum is $G_{\kappa, \theta}(\omega - W)$, the Gamma distribution with mean $\kappa\theta$ and variance $\kappa\theta^2$. The Gamma distribution is chosen here because it is one of those distributions that is identically zero for frequencies below a certain value, $\omega = W$ in this case, which avoids populating Rydberg states. The parameters κ and θ produce an XUV spectrum peaked at an energy $\omega_X = 80$ eV + $W = 92.2$ eV, with a FWHM bandwidth $\delta\omega_X \approx 32.4$ eV, yielding a 55.4 as pulse. Throughout this study, the attosecond XUV pulse always temporally overlaps with the center of the laser pulse, at the extremum of $F_L(t)$.

For the NIR field, τ_L and ω_L are chosen to produce a laser pulse with a full-width at half-maximum (FWHM) duration of 3 fs and a central wavelength of 800 nm; F_0 is the laser field's peak amplitude. The laser electric field $F_L(t)$, which I refer as the *control field*, is therefore a cosine pulse. The laser field amplitude F_0 is the variable parameter in the present study. It influences the trajectories taken by the electron as it exits the system.

Recall that in the absence of a laser field, $F_0 = 0$, the solution of the time-dependent Schrödinger equation (TDSE) is given by (2.5). In this section I use physical transition dipole matrix elements $d(p) = \langle \phi_p^{(-)} | q | \psi_0 \rangle$, evaluated between the initial (bound) eigenstate $|\psi_0\rangle$ and positive-energy eigenstates $\langle \phi_p^{(-)} |$, both eigenstates of the field-free Hamiltonian $H_0 = p^2/2 + V_N(q)$. The bound state $|\psi_0\rangle$ is obtained by solving the spatially-discretized time-independent Schrödinger equation (TISE) $\langle q | H_0 | \psi_0 \rangle = E_0 \langle q | \psi_0 \rangle$, while the states $\langle \phi_p^{(-)} |$ are solutions to the 1D Lippmann-Schwinger (LSE) equation with an advanced Green's function:

$$\langle q | \phi_p \rangle = e^{ipq} - \frac{2i}{|p|} \int_{-\infty}^{\infty} e^{-i|p(q-q')|} V_N(q') \phi_p(q') dq'. \quad (2.17)$$

The LSE is equivalent to the TISE, but is more suitable for calculating positive-energy eigenstates with physical asymptotics, including the correct scattering phase shifts. I solve the LSE iteratively, by computing the Born series until it converges.

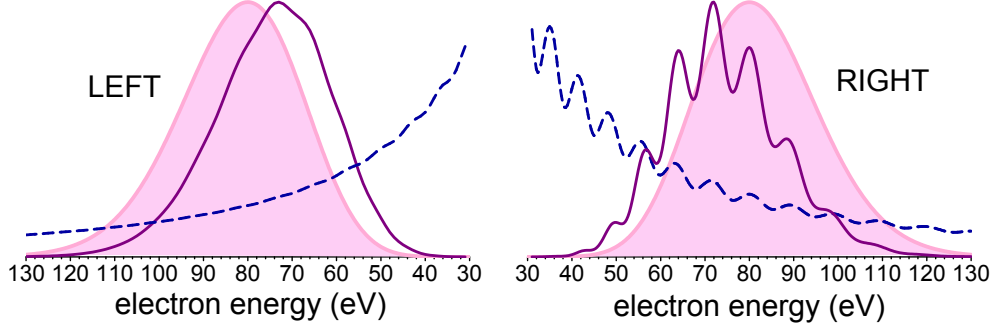


Figure 2.3: The solid lines represent the momentum spectra for the left-going and right-going photoelectron wave packets evaluated from (2.5), using transition dipole matrix elements $d(p)$ (dashed lines) obtained by solving (2.17). The shaded areas represent the XUV spectrum $|G_{\kappa,\theta}(\varepsilon)|^2$ as a function of electron energy ε .

Now, for the system under present scrutiny (Figure 2.2), laser-dressed scattering is clearly more pronounced on the right-going wave packet⁵, as shown in Figure 2.3. It manifests itself as a modulation of the photoelectron spectrum for positive momenta (detected on the right). This modulation, in momentum space, corresponds to a characteristic length of ≈ 49.3 a.u., which is about twice the internuclear spacing. Quantum-mechanically, this modulation is explained by the fact that the matrix elements $d(p)$ oscillate significantly for positive momenta, detected on the right side, while they are quite smooth for negative momenta, detected on the left side. Expression (2.5) says that the photoelectron spectrum is just the XUV spectrum translated by the ionization energy and modulated by the dipole response $d(p)$. Therefore, the outgoing wave packets naturally embody the dipole response $d(p)$.

In the presence of a NIR laser field, there is a standard amendment to (2.5), which can describe laser-dressed single-photon ionization. It is the Coulomb-Volkov approximation (CVA) [52, 117], as previously studied in Section 1.5 and 2.1. The CVA is used to account for the action of the laser field on the ejected electron; it reads

$$\langle p | \psi_{\text{CVA}}(t_f) \rangle = e^{-\frac{i}{2} p^2 t_f} \int_{-\infty}^{t_f} F_X(t) d(p + A_L(t)) e^{i(-\frac{1}{2} \int_t^{t_f} (p + A_L(t'))^2 dt' + Wt)} dt, \quad (2.18)$$

where $A_L(t)$ is the vector potential of the NIR laser field. As discussed in Section 1.5, the Coulomb-Volkov approximation relies on a couple of intuitive arguments. First, an

⁵The left-going wave packet displays a very weak, but visible amount of spectral modulation. The modulation on the left-going wave packet is a result of a higher-order scattering event which is not drawn in Figure 2.2. It's when the electron, which starts at the potential Z_1 , bounces off Z_2 , and then Z_1 again before heading on to the detector on the left.

electron trajectory ending with a momentum p , e.g. at the detector, must have been launched with an energy $(p + A_L(t))^2/2$ at the moment of ionization t . Therefore, $\langle\phi_p|$ should back-propagate to $\langle\phi_{p+A(t)}|$ at the moment of ionization, which is why the matrix element $d(p + A_L(t))$ is used in (2.18). Second, the electron's evolution under the laser field is accounted for by the Volkov phase, given by the integral in the exponential of (2.18), which is the quantum phase acquired by a free electron in an electromagnetic field.

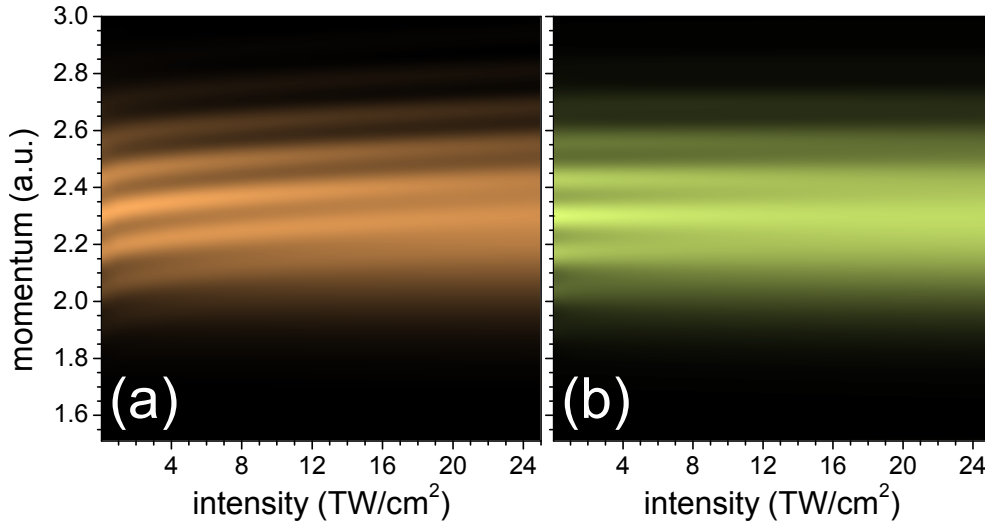


Figure 2.4: Panel (a) shows laser-dressed photoelectron spectra evaluated numerically from the TISE and (b) from the CVA, for a range of intensities of the control field. The CVA does predict a fringe pattern, but fails to account for its change under the control field.

The CVA (2.18) is known to adequately describe laser-dressed photoionization of atoms [52]. However, it cannot properly describe laser-dressed photoionization if the system is too large. In Figure 2.4, a series of laser-dressed photoelectron spectra computed by numerically solving the TDSE (panel a) are compared to those obtained by evaluating the CVA expression (2.18) for different values of the control field's intensity (panel b). Since the attosecond XUV pulse is centered at $t = 0$, where the vector potential of the NIR field is zero according to (2.16b), no momentum shift is expected for the outgoing electron. Nevertheless, the TDSE predicts a noticeable shift of the interference pattern towards larger momenta as a function of the control field's strength. This effect is not accounted for by the CVA. Now since the CVA is a semi-classical modification of the quasi-exact expression (2.5), this would appear to preclude an intuitive classical interpretation of laser-dressed photoelectron scattering based on the simple trajectories shown in Figure 2.2.

However, I won't abandon the classical approach just yet. Instead, I'll present an intuitive theoretical model based on trajectories [178, 93] to describe laser-dressed photoelectron scattering. As will be clear from the subsequent analysis, this quasi-classical model quantitatively accounts for the effects of the laser field on the spectral interference.

In order to gain a deeper understanding of the dynamics of the electron as it exits the system, let's take a closer look at the final positive-energy components of the electron's

wave function. It is useful to think of the propagated state $|\psi(t_f)\rangle$ as being composed of a sum of two parts, corresponding to two ensembles of trajectories taken by the outgoing electron: those for which the electron heads directly to the detector, and those which make it re-scatter off the adjacent nucleus before going to the detector. For the subsequent analysis, I further simplify this picture into a rather classical one, by considering strictly two trajectories: a *direct* trajectory and a *reflected* trajectory, which will be described below.

It's possible to separate the contributions of these two trajectories from the total positive-energy wave packet by applying a simple unitary transformation corresponding to the back-propagation of a free particle:

$$|w(t_f)\rangle = \exp\left(\frac{i}{2}p^2t_f\right) |\psi(t_f)\rangle. \quad (2.19)$$

The projection of $|w(t_f)\rangle$ in configuration space allows to define a quantity which I call

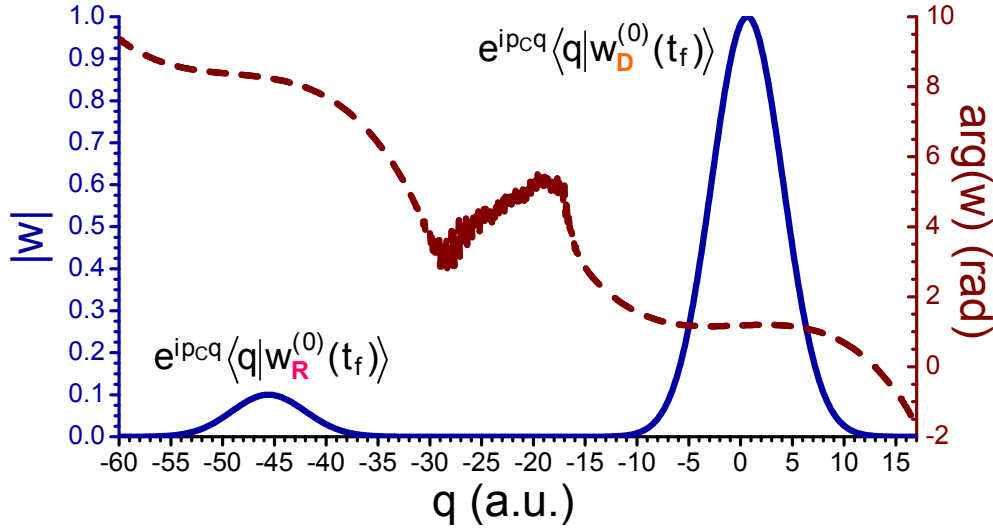


Figure 2.5: The amplitude (solid line) and phase (dashed line) of the wave parcel shows two separate contributions $|w_R^{(0)}(t_f)\rangle$ and $|w_D^{(0)}(t_f)\rangle$. The wave parcel is evaluated in the absence of the control field, as indicated by the superscript “(0)”. I removed the central momentum p_C from the wave parcel to better visualize the phases of the direct and reflected components. Once projected into real space, the wave parcels $w_D^{(0)}(t_f, q)$ and $w_R^{(0)}(t_f, q)$ are located at the *apparent* starting points of the electron trajectories.

the *wave parcel* in position space,

$$w(t_f, q) = \frac{1}{2\pi} \int_{-\infty}^{\infty} \langle p|\psi(t_f)\rangle e^{\frac{i}{2}p^2t_f} e^{ipq} dp; \quad (2.20)$$

the states $\langle p|$ are just free-particle eigenstates. This position-space wave parcel is very closely related to the time-domain wave parcel $w(t)$ introduced in the last section. In fact,

$w(t)$ is just given by

$$\varpi(t) = \frac{1}{2\pi} \int_{-\infty}^{\infty} \left(\int_{-\infty}^{\infty} w(t_f, q) e^{-ipq} dq \right) \Theta(\pm p) e^{-\frac{i}{2}p^2 t} p dp, \quad (2.21)$$

where $\Theta(\pm p)$ is the Heaviside step function and the “ \pm ” sign specifies a direction of observation: left (“ $-$ ”) or right (“ $+$ ”). In three dimensions, $\Theta(\pm p)$ would be replaced by an orientational delta function, e.g. $\delta(\sin \theta - \sin \theta_0) \delta(\phi - \phi_0)$, to select the part of the wave packet propagating in azimuthal and polar directions ϕ_0 and θ_0 , respectively. From this point on, I will refer to $w(t_f, q)$ simply as the wave parcel.

The field-free wave parcel $w^{(0)}(t_f, q)$, i.e. with the control field turned off, is plotted in Figure 2.5. It has been evaluated with the control field turned off ($F_0 = 0$), as indicated by the superscript “(0)”. The wave parcel clearly consists of two parts. It has a large hump, denoted by $\langle q | w_D^{(0)}(t_f) \rangle$ in Figure 2.5, centered about the origin, and a smaller hump $\langle q | w_R^{(0)}(t_f) \rangle$ centered at ~ -45.6 a.u. As will be clear from the subsequent analysis, the large and small humps correspond, respectively, to the direct and reflected trajectories taken by the outgoing electron.

Since the wave parcel is obtained by propagating the final positive-energy wave function backward in time as a free particle, the position of the wave parcel represents the *apparent* starting point of the electron from the perspective of an observer measuring the electron at the final time t_f , assuming free-particle motion and therefore ignorant of any prior dynamics. This apparent starting position is analogous to a *delay* of the wave parcel. Undoing the unitary transformation to the individual wave parcel components thus gives the direct and reflected parts of the wave function at the end of the propagation, i.e. $|\psi_{R,D}(t_f)\rangle = \exp\left(-\frac{i}{2}p^2 t_f\right) |w_{R,D}(t_f)\rangle$.

Here, we also note an important property of the wave parcel. For t_f sufficiently large, the positive-energy part of the wave function essentially propagates as a free particle, rendering the associated wave parcel time independent,

$$\lim_{t_f \rightarrow \infty} \frac{d}{dt} |w(t_f)\rangle = 0. \quad (2.22)$$

Thus, I henceforth drop the time argument of the wave parcel because the electron is assumed to be measured long after its interaction with the fields and the ionic potential, so that its wave parcel $|w\rangle$ no longer depends on the time of measurement t_f .

For the system under consideration, the net momentum shift of the direct trajectory is negligible since the ionization takes place at a zero-crossing of the control field’s vector potential. The interesting physics occurs during the re-scattering event, experienced by the smaller hump of the wave parcel (the reflected wave parcel). Figure 2.6 shows the parameters of the reflected wave parcel as a function of the intensity of the control field. Since photoionization takes place under a positive laser field—i.e. one that adds a *positive* slope to the potential $V_N(q)$ —the re-scattered electron is initially accelerated toward the adjacent potential. Since the re-scattering probability decreases with larger incident momentum, the probability associated to the reflected wave parcel naturally decreases with

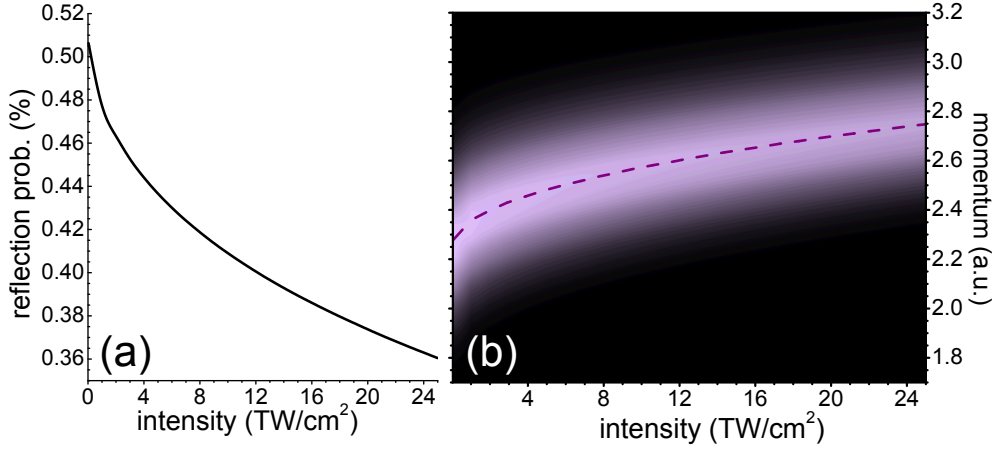


Figure 2.6: In panel (a), the reflection probability is plotted against the control field intensity, while panel (b) shows the momentum spectra of the reflected wave parcel, along with the classically-expected final momentum of the reflected trajectory (dashed line).

the control field strength, as displayed in Figure 2.6-a. Furthermore, the momentum spectra of the reflected wave parcel, shown in Figure 2.6-b, are progressively shifted to larger momenta for increasing strengths of the control field.

It turns out that this last effect, the dependence of the reflected momentum on the laser field, is well explained by classical mechanics. The dashed line plotted in Figure 2.6-b represents final momenta computed by classically propagating an electron along the reflected trajectory. This, in combination with the fact that the wave parcel contains only two contributions as shown in Figure 2.5, suggests that the propagation of the outgoing electron can be described by considering two classical electron trajectories in a laser field.

In the following, I conduct calculations of both the reflected (R) and direct (D) trajectories by launching them at the center of the initial potential (Z_1), at $x_{R,D}(0) = 0$, with initial velocities

$$v_j(0) = \pm \sqrt{\left(v_j^{(0)}(t_f)\right)^2 + 2\left(V_N(x_j^{(0)}(t_f)) - V_N(0)\right)}, \quad (2.23)$$

where the subscript j stands for the direct (D) or reflected (R) trajectory, and the final positions $x_j^{(0)}(t_f) = \langle \psi_j^{(0)}(t_f) | q | \psi_j^{(0)}(t_f) \rangle$ and velocities $v_j^{(0)}(t_f) = \langle \psi_j^{(0)}(t_f) | p | \psi_j^{(0)}(t_f) \rangle$ are extracted from the *field-free* reflected wave packets $|\psi_j^{(0)}(t_f)\rangle$. The “ \pm ” sign in (2.23) indicates that direct trajectories are launched to the right (“+”) while reflected trajectories are launched to the left (“−”). The re-scattered electron thus initially travels to the left, toward the adjacent potential (Z_2). Once inside the scattering potential, at $x_R = -24$ a.u., the electron abruptly reverses its direction as if it elastically bounces off a wall, leading it back towards the detector. In the absence of the control field, the reflected electron crosses the initial potential $Z_1 \sim 480$ as later. When the control field is turned on, this delay changes by ± 20 as for the field intensities considered herein.

The change in the fringe pattern as a function of the control field strength can also be explained by this classical approach. Just as the CVA (2.18) explains laser-dressed spectra by amending the field-free expression (2.5) to account for the action of the laser field, I explain the laser-dressed spectra by adjusting the field-free wave parcel using the classically evaluated direct and reflected trajectories in the laser field.

The classical simulations produce the analogues of the phases $\Delta S_{R,D}^{(L)}$, momenta $p_{R,D}^{(L)}$ and positions $q_{R,D}^{(L)}$ of the direct (D) and reflected (R) wave parcels. These three quantities set, respectively, the position, the bias and the spacing of the interference pattern in the photoelectron spectrum, and are deduced from the classical trajectories according to the following relations:

$$q_j^{(L)} = x_j(t_f) - v_j(t_f)t_f, \quad p_j^{(L)} = v_j(t_f), \quad (2.24a)$$

$$\Delta S_j^{(L)} = \int_0^{t_f} L(x_j(t), v_j(t), t) dt - \frac{1}{2}v_j^2(t_f)t_f, \quad (2.24b)$$

and $L(x_j(t), v_j(t), t)$ denotes the Lagrangian evaluated along the reflected or direct trajectory, parameterized by $x_j(t)$ and $v_j(t)$. Again, the index $j \in \{R, D\}$ refers to the direct (D) or reflected (R) trajectory. Since the wave parcel is obtained by back-propagating the wave packet as a free particle, the classical parameters $\Delta S_j^{(L)}$, $p_j^{(L)}$, and $q_j^{(L)}$ also include the effects of free-particle back-propagation.

Using these classical quantities, the laser-dressed photoelectron spectra are accounted for by modifying the field-free direct and reflected wave parcels, $w_D^{(0)}(q)$ and $w_R^{(0)}(q)$ respectively. The laser dressed wave parcels $w_{R,D}^{(L)}(q)$ are obtained according to the prescription

$$w_j^{(L)}(q) = w_j^{(0)} \left(q - q_j^{(L)} + q_j^{(0)} \right) e^{i \left((p_j^{(L)} - p_j^{(0)}) (q - q_j^{(L)}) + \Delta S_j^{(L)} - \Delta S_j^{(0)} \right)}, \quad (2.25)$$

where $q_j^{(0)}$ and $p_j^{(0)}$ are respectively the positions and momenta of the field-free wave parcels, given by (2.24a). As indicated by this transformation, the field-free wave parcel is first centered at position $q_j^{(L)}$, evaluated from the classical trajectory. Its momentum and phase offset are then set in position space with the classically evaluated parameters $p_j^{(L)}$ and $\Delta S_j^{(L)}$, respectively. Thus, the transformation (2.25) makes use of purely classical information to account for the control field. This classical information is sufficient to explain the effect of the control field on the fringes in the photoelectron spectra, as shown in Figure 2.7. Indeed, the spectra evaluated using the classical model represent a marked improvement to those erroneously predicted by the CVA (cf. Figure 2.4).

For a given laser field strength, the fringe patterns are reproduced over a wide range of momenta, despite the fact that only a single initial momentum was used for each classical trajectory. The classical simulations neglect two purely quantum-mechanical effects: the influence of the control field on the reflection probability and the phase acquired upon reflection (i.e. the scattering phase shift for the backward direction). Consequently, the position and contrast of the spectral fringes predicted from our model is slightly off at larger

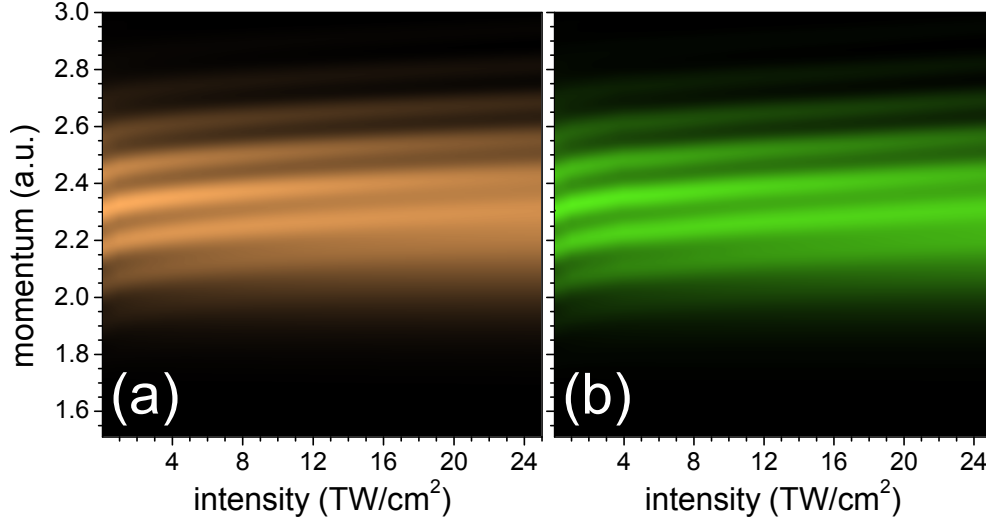


Figure 2.7: The classically-adjusted laser-dressed photoelectron spectra, shown in panel (b), based on the transformation (2.25), reproduce the correct fringe patterns predicted by the TDSE (a). It is the difference in the back-propagated action ΔS , between the reflected and direct trajectories, that sets the position of the fringes. The classically-adjusted spectra shown in panel (b) above are to be compared to those evaluated from the CVA (Figure 2.4-b).

control field strengths. These purely quantum mechanical effects cannot be explained by the classical model.

In order to clearly illustrate the key physics and to make the relevant effects more discernible, a rather large system was considered. Such a system might be a dissociating diatomic molecule, a dimer, an excimer, or a nano-structure composed of two spatially separated entities. Our analysis also applies to smaller systems. A smaller system would result in a broader spectral modulation, requiring a larger XUV bandwidth to capture enough fringes; or equivalently stated, it would require a shorter attosecond pulse so that the wave parcel is made up of two spatially distinct portions $w_D(q)$ and $w_R(q)$. The classical approach presented here applies more generally. For instance, in the case of a delocalized initial state, the starting points of the classical trajectories should be located near the peaks of the initial state, with all first-order re-scattering events considered for each trajectory.

In this section, we have seen that an external NIR laser field controls the re-scattering of an electron, which can be observed by measuring the photoelectron spectrum for different NIR field intensities. The NIR field mainly affects three parameters of the re-scattered wave packet: it changes its momentum, its action and its apparent starting position, the latter of which corresponds to a *delay* when considered in the time domain. On the other hand, for moderate intensities the control field hardly affects the scattering phase shift of the re-scattered electron, although the probability of re-scattering was found to be affected by the strength of the control field. This might provide a means to generate and control a spatially and temporally confined electric current on a single atom by launching a free

electron wave packet with an attosecond pulse in the presence of a controlled NIR wave form.

As evidenced in this study, the semi-classical Coulomb-Volkov approximation cannot describe these effects, and indeed breaks down for such a spatially extended system. In order to uphold a physically intuitive picture of laser-dressed scattering, I presented a new “billiard ball” model, based on classical trajectories, that quantitatively explains the influence of the NIR control field on the photoelectron interference pattern. The classical model presented here is generalizable to larger systems, and thus constitutes a powerful tool for interpreting this new kind of spectroscopic measurement, where a spatially extended system is monitored or characterized using its own outgoing electron.

Conclusion

I hope I gave you a taste of the power of attosecond electron spectroscopy. To summarize this thesis, I began with a brief overview of the key experimental and theoretical developments in strong-field physics that led to the generation of coherent attosecond XUV radiation. I then briefly explained how this XUV radiation is temporally or spectrally filtered in order to obtain an isolated attosecond pulse, and described methods used to characterize these attosecond pulses, and gave particular emphasis on the attosecond streaking measurement, which was the main focus of this work. To this existing body of knowledge, I added several contributions.

First, I introduced a formalism based on trajectories that treats the main effects that are observed in an attosecond streaking measurement—the shift and broadening of photoelectron spectra due to the near-infrared streaking field. I used this classical trajectory formalism as a basis for a robust and efficient method, which I call iCrap, to extract the chirp of an attosecond pulse [71].

Following this classical treatment of attosecond streaking, I presented a more quantum mechanical formalism. Based on this quantum formalism, I invented an algorithm to characterize the full temporal profile of an attosecond pulse. This algorithm, which I call the LSGPA, is tailored specifically for the analysis of streaking measurements [72]. I conducted a thorough assessment of the robustness of this algorithm against various uncertainties that rear their heads in realistic experiments [70]. Through this analysis, I found that the LSGPA is best suited for characterizing an isolated attosecond pulse—a pulse that is confined to within a half-cycle of the streaking field. This algorithm was used for characterizing the record-breaking 80 as pulses generated in 2008 by E. Goulielmakis *et al.* [85], and also to uncover a yet unexplained delay of 20 as between photoemissions from the $2s$ and $2p$ sub-shells of neon, found by M. Schultze *et al.* in 2010 [172].

While attosecond streaking was originally meant to characterize the field of attosecond pulses, further inspections with the LSGPA by V. S. Yakovlev *et al.* [212] revealed that it actually characterizes a quantity that is a dispersion-compensated version of the photoelectron wave packet, which I called the wave parcel. With the wave packet now in my cross hairs, I decided to conduct further investigations into wave packet dynamics when photoionizing a spatially extended system in the presence of a near-infrared laser field. I found that the wave packet embodies the electron trajectories passing through different parts of the system. Using this information, I came up with a billiard ball model, based on electron trajectories, that describes the scattering dynamics of an attosecond photoelectron

wave packet in the presence of a near-infrared control field [74].

This thesis treated just a few of the numerous facets of attosecond science. Indeed, this burgeoning field is currently branching out in several directions—notably, in the study of ultra-fast dynamics in solids and molecules. It is also currently being extended to the regime of relativistic light-matter interactions, which aims to push pulse durations down to the zeptosecond scale! Indeed, at the current pace of this technology’s development, it is difficult to predict how attosecond science will play out.

Appendix A

Energy-Resolved Photoelectron Angular Distributions

Although the contents of this thesis suggest I was living in Flatland throughout my degree, I did have the chance to play around in more spatial dimensions. Angle and energy resolved measurements [160, 112, 113]—based on such advanced techniques as cold-target recoil ion momentum spectroscopy (COLTRIMS) [202, 201, 47] and velocity-map imaging (VMI) [30, 146]—have the power to greatly enrich the information acquired via attosecond streaking, particularly in regards to systems with an anisotropic geometry, such as small molecules [41, 132, 206, 33], medium-size molecules [73], large molecules [128], clusters [145] and solids [109, 40, 215]. Therefore, I naturally had to have a look at angle-resolved photoionization.

In this appendix, I describe how positive-energy eigenstates of a single-electron Hamiltonian may be computed by solving the Lippmann-Schwinger equation (LSE) [141]. As previously detailed in Section 1.5, positive-energy eigenstates are required in order to calculate photoionization cross-sections. We previously dealt with the LSE in Section 2.2, which was used to compute positive-energy eigenstates of a one-dimensional system. Here, I consider a generalization of the LSE to three spatial dimensions, and for long-range potentials.

Although no original research came from this project, which is why it didn't make it into the main body of the thesis and is instead relegated to an appendix, the time I spent working out some of the technical details of this problem should definitely not go to waste! As many of these technicalities are spread throughout the literature, I had to sift through quite a few articles and textbooks to find everything I needed. In addition to the quantum mechanics textbooks of K. Gottfried and T. M. Yan [82], J. J. Sakurai [165] and B. H. Bransden and C. J. Joachain [20], I found the articles of R. R. Lucchese and V. McKoy [157, 187, 132, 129] to be particularly illuminating in this respect. Nevertheless, I decided to group all these pieces of information into this appendix, in the hope that the invaluable knowledge I acquired during this endeavor will be of use to someone else who would like to evaluate single-electron scattering states and single-photon ionization cross-sections of anisotropic systems.

A.1 The Coupled-Wave Lippmann-Schwinger Equation

To provide a bit more context for the LSE, let's consider a Hamiltonian $H = H_0 + V(\mathbf{r})$, which is defined in terms of an unperturbed Hamiltonian H_0 , and a perturbation $V(\mathbf{r})$ which disappears as $|\mathbf{r}| = r \rightarrow \infty$. Let's assume the Hamiltonian H_0 has known eigenstates $|\phi_0\rangle$ and eigenvalues ε , such that

$$H_0|\phi_0\rangle = \varepsilon|\phi_0\rangle. \quad (\text{A.1})$$

Since positive-energy states form a continuum, for each energy $\varepsilon > 0$ the full Hamiltonian H possesses an eigenstate $|\phi\rangle$ with an energy ε that coincides with that of the eigenstate $|\phi_0\rangle$ of H_0 . In other words, for any energy $\varepsilon > 0$, there exists a state $|\phi\rangle$ that solves the time-independant Schrödinger equation (TISE)

$$(H_0 + V(\mathbf{r}))|\phi\rangle = \varepsilon|\phi\rangle. \quad (\text{A.2})$$

Given knowledge of the states $|\phi_0\rangle$, we seek the state $|\phi\rangle$ that solves (A.2). We may formally solve this TISE by writing $|\phi\rangle$ as

$$|\phi^{(\pm)}\rangle = |\phi_0\rangle + \lim_{\epsilon \rightarrow 0} \left(\frac{V(\mathbf{r})}{\varepsilon - H_0 \pm i\epsilon} \right) |\phi^{(\pm)}\rangle, \quad (\text{A.3})$$

where (A.2) is recovered by multiplying (A.3) with $\varepsilon - H_0 \pm i\epsilon$ on both sides. An unphysical imaginary energy $i\epsilon$ had to be added to avoid the obvious singularity. This imaginary part is then removed by taking the limit $\epsilon \rightarrow 0$. Although $i\epsilon$ is unphysical, the “ \pm ” sign actually has physical implications for the solution, as we will see.

Let's now reduce the level of abstraction by letting $H_0 = p^2/2$, the free-particle Hamiltonian, and choose the plane wave basis, which is a complete representation of functions on \mathbb{R}^3 . The states $|\phi_0\rangle$ can then be taken as the plane wave states $|\mathbf{p}\rangle$, which are simultaneous eigenstates of the p_x , p_y and p_z operators, with energy $\varepsilon = |\mathbf{p}|^2/2 = p^2/2$. By projecting to the left on $\langle \mathbf{r}|$, and inserting the closure relation $\int d^3r' |\mathbf{r}'\rangle \langle \mathbf{r}'|$ in the second term on the RHS, expression (A.3) can be written in the position basis as

$$\phi_{\mathbf{p}}^{(\pm)}(\mathbf{r}) = \frac{e^{i\mathbf{p}\cdot\mathbf{r}}}{(2\pi)^{3/2}} + \int d^3r' G^{(0)}(|\mathbf{r} - \mathbf{r}'|) V(\mathbf{r}') \phi_{\mathbf{p}}^{(\pm)}(\mathbf{r}'), \quad (\text{A.4a})$$

$$\text{where } G_0^{(\pm)}(|\mathbf{r} - \mathbf{r}'|) = \lim_{\epsilon \rightarrow 0} \left(\langle \mathbf{r}| (p^2/2 - H_0 \pm i\epsilon)^{-1} |\mathbf{r}'\rangle \right) = -\frac{1}{2\pi} \frac{e^{\pm ip|\mathbf{r} - \mathbf{r}'|}}{|\mathbf{r} - \mathbf{r}'|} \quad (\text{A.4b})$$

is the free-particle Green's function. This is the Lippmann-Schwinger equation in 3D (3D-LSE). Solving it produces a positive-energy eigenstate $\phi_{\mathbf{p}}^{(\pm)}(\mathbf{r}) = \langle \mathbf{r}|\phi_{\mathbf{p}}^{(\pm)}\rangle$ of the full Hamiltonian H , labeled with all three momentum components $\mathbf{p} = (p_x, p_y, p_z)$ since we adopted the plane wave basis for solutions of H_0 .

The solution $\phi_{\mathbf{p}}^{(\pm)}(\mathbf{r})$ is composed of two parts. The first term on the RHS of (A.4a), a plane wave in this case, describes the asymptotic behavior of $\phi_{\mathbf{p}}^{(\pm)}(\mathbf{r})$ as $r \rightarrow \infty$ (recall that

$V(\mathbf{r}) \rightarrow 0$ as $r \rightarrow \infty$), while the second term describes the effect of $V(\mathbf{r})$. As the formalism presented so far is purely time-independent, (A.4a) describes a steady-state process: the *scattering* of a plane wave by a potential $V(\mathbf{r})$, where the scattered part is given by the second term on the RHS of (A.4a), while the first term embodies the asymptotical behavior of the solution¹.

Once time-dependence is considered—by multiplying both sides of (A.4a) with $e^{-i\epsilon t}$ —the implication of the choice afforded by the “ \pm ” sign becomes obvious: it determines whether the scattered wave travels outward (“+”) or inward (“−”). More specifically, choosing the (“+”) sign produces the outgoing scattering solution $\phi_{\mathbf{p}}^{(+)}(\mathbf{r})$, describing the (causal) scattering of a plane wave with momentum \mathbf{p} incident upon the target potential $V(\mathbf{r})$. Choosing the (“−”) sign yields an incoming scattering state $\phi_{\mathbf{p}}^{(-)}(\mathbf{r})$ that asymptotically becomes a plane wave with momentum \mathbf{p} infinitely far from the target. As discussed in Section 1.5, the treatment of photoionization requires incoming-type scattering states, so we further restrict our discussion to the solutions $\phi_{\mathbf{p}}^{(-)}(\mathbf{r})$.

For calculating these positive-energy solutions, solving (A.4a) directly is not the most efficient approach. Firstly, this three-dimensional integral equation presents a singularity whenever $\mathbf{r} = \mathbf{r}'$, i.e. for each spatial position \mathbf{r} of the solution $\phi_{\mathbf{p}}^{(-)}(\mathbf{r})$, it is necessary to integrate over a singularity at $\mathbf{r}' = \mathbf{r}$. Moreover, since we are after *angle-resolved* cross-sections, we require the evaluation of a solution $\phi_{\mathbf{p}}^{(-)}(\mathbf{r})$ for all directions of observation $\hat{\mathbf{p}} = \mathbf{p}/|\mathbf{p}|$, which amounts to a very large number of solutions to compute if a fine angular resolution is required. So instead of solving (A.4a) as in [100], we can obtain a solution for all directions simultaneously by expanding $\phi_{\mathbf{p}}^{(-)}(\mathbf{r})$ into partial waves with respect to its asymptotical propagation direction $\hat{\mathbf{p}}$:

$$\phi_{\mathbf{p}}^{(-)}(\mathbf{r}) = \sum_{l=0}^{\infty} \sum_{m=-l}^l \phi_{plm}^{(-)}(\mathbf{r}) Y_{l,m}^*(\hat{\mathbf{p}}), \quad (\text{A.5})$$

where $Y_{l,m}(\hat{\mathbf{p}})$ is a spherical harmonic evaluated in the direction of observation $\hat{\mathbf{p}}$ of the photoelectron. The partial wave expansion (A.5) just decomposes the plane wave, measured infinitely far from the region of interaction, into spherical waves. Thanks to the linearity of the 3D-LSE (A.4a), the scattering of a plane wave can be understood as a superposition of spherical wave scattering processes. Thus, the spherical scattering waves $\phi_{plm}^{(-)}(\mathbf{r})$ also satisfy 3D-LSE’s in their own right,

$$\phi_{plm}^{(-)}(\mathbf{r}) = \sqrt{\frac{2}{\pi}} i^l j_l(pr) Y_{l,m}(\hat{\mathbf{r}}) + \int d^3r' G_0^{(-)}(|\mathbf{r} - \mathbf{r}'|) V(\mathbf{r}') \phi_{plm}^{(-)}(\mathbf{r}'), \quad (\text{A.6})$$

¹Herein lies the key advantage of working with the Lippmann-Schwinger equation instead of the TISE. Because I chose $H_0 = p^2/2$, I had the freedom to make the solution to the LSE behave like a plane wave asymptotically, i.e. by choosing $\langle \mathbf{r} | \phi_0 \rangle$ as a plane wave. Knowing that free spherical waves are also eigenfunctions of $H_0 = p^2/2$, I could have just as well taken $\langle \mathbf{r} | \phi_0 \rangle$ as a free spherical wave, in which case the LSE would describe the scattering of a spherical wave by $V(\mathbf{r})$. Alternatively, I could have also included part of the scattering potential $V(\mathbf{r})$ into H_0 , which would change the expression of the first term $\langle \mathbf{r} | \phi^{(\pm)} \rangle$ and therefore necessarily the second term. This last strategy is particularly useful in solving the LSE for a long-range ($-Z/r$) scattering potential.

where $j_l(pr)$ is a spherical Bessel function of the first kind, of order l , and $Y_{l,m}(\hat{\mathbf{r}})$ is a spherical harmonic evaluated in the spatial direction $\hat{\mathbf{r}} = \mathbf{r}/|\mathbf{r}|$. Alternatively, expression (A.6) can be obtained by inserting the closure relation in the second term on the RHS of (A.3), using angular momentum resolved states $|plm\rangle$ instead of momentum resolved states $|\mathbf{p}\rangle$. Thus, the scattering of a plane wave $(2\pi)^{-3/2}e^{i\mathbf{p}\cdot\mathbf{r}}$ has been decomposed into a superposition of scattering problems involving free spherical waves $\sqrt{2/\pi}i^l j_l(pr)Y_{l,m}(\hat{\mathbf{r}})$. In contrast to the wave functions $\phi_{\mathbf{p}}^{(-)}(\mathbf{r})$, which possess a well defined momentum at infinity, the wave functions $\phi_{plm}^{(-)}(\mathbf{r})$ possess a well-defined *angular* momentum at infinity.

Obviously, this partial wave expansion about the direction of observation $\hat{\mathbf{p}}$ is not enough, because the 3D-LSE (A.6) is still has a three-dimensional integral equation that contains an infinite number of singularities at spatial points $\mathbf{r} = \mathbf{r}'$. To make things a little more tractable, let's also expand the scattering potential $V(\mathbf{r})$, the free-particle Green's function $G_0^{(-)}(|\mathbf{r} - \mathbf{r}'|)$, as well as the spherical scattering wave $\phi_{plm}^{(-)}(\mathbf{r})$, into partial waves:

$$V(\mathbf{r}) = \sum_{l=0}^{\infty} \sum_{m=-l}^l v_{l,m}(r) Y_{l,m}(\hat{\mathbf{r}}) \quad (\text{A.7a})$$

$$G_0^{(-)}(|\mathbf{r} - \mathbf{r}'|) = 2ip \sum_{l=0}^{\infty} \sum_{m=-l}^l j_l(pr_{<}) h_l^*(pr_{>}) Y_{l,m}^*(\hat{\mathbf{r}}') Y_{l,m}(\hat{\mathbf{r}}), \quad (\text{A.7b})$$

$$\phi_{plm}^{(-)}(\mathbf{r}) = \sum_{l'=0}^{\infty} \sum_{m'=-l'}^{l'} \chi_{l',m'}^{plm}(r) Y_{l',m'}(\hat{\mathbf{r}}), \quad (\text{A.7c})$$

with $r_{<} = \min(r, r')$ and $r_{>} = \max(r, r')$,

where $h_{\kappa}(\rho) = j_{\kappa}(\rho) + iy_{\kappa}(\rho)$ is a spherical Hankel function of order κ , defined in terms of a spherical Bessel function of the first kind $j_{\kappa}(\rho)$ and a spherical Bessel function of the second kind $y_{\kappa}(\rho)$. Using these partial wave expansions, we can write the 3D-LSE as a set of one-dimensional integral equations coupled through the angular momentum quantum numbers, i.e.

$$\begin{aligned} \chi_{l',m'}^{plm}(r) = & \sqrt{\frac{2}{\pi}} i^l j_l(pr) \delta_{l,l'} \delta_{m,m'} \\ & + ip(-1)^{m'} \sqrt{\frac{2l'+1}{\pi}} \sum_{\lambda,\mu} \sum_{\kappa,\nu} \sqrt{(2\kappa+1)(2\lambda+1)} \begin{pmatrix} \kappa & \lambda & l' \\ 0 & 0 & 0 \end{pmatrix} \\ & \times \begin{pmatrix} \kappa & \lambda & l' \\ \nu & \mu & -m' \end{pmatrix} \int_0^{\infty} r'^2 dr' j_{l'}(pr_{<}) h_{l'}^*(pr_{>}) v_{\kappa,\nu}(r') \chi_{\lambda,\mu}^{plm}(r'). \end{aligned} \quad (\text{A.8})$$

Expression (A.8) is the coupled-wave Lippmann-Schwinger equation (CW-LSE). The quantities represented in tabular form in (A.8) are Wigner $3j$ -symbols, and are related to the Clebsch-Gordan coefficients $\langle j_1, m_1, j_2, m_2 | J, M \rangle$ —the projection of total angular-momentum

eigenstates onto uncoupled angular-momentum eigenstates—through the following relation

$$\begin{pmatrix} j_1 & j_2 & J \\ m_1 & m_2 & -M \end{pmatrix} = \frac{(-1)^{j_1-j_2+M}}{\sqrt{2J+1}} \langle j_1, m_1, j_2, m_2 | J, M \rangle. \quad (\text{A.9})$$

Although the CW-LSE looks daunting, the partial wave components $\chi_{l',m'}^{plm}(r)$ can be solved straightforwardly by perturbative iteration. If the scattering potential $V(\mathbf{r})$ is indeed a perturbation, which is true if it is much smaller than $H_0 = p^2/2$ (i.e. for sufficiently energetic electrons), then the initial guess $\chi_{l',m'}^{plm}(r) \sim \sqrt{2/\pi} i^l j_l(pr) \delta_{l,l'} \delta_{m,m'}$ is a reasonably good starting point², which can be successively improved by inserting it into the RHS of (A.8), taking the resulting function $\chi_{l',m'}^{plm}(r)$, re-inserting it into the RHS of (A.8), and so on and so forth until $\chi_{l',m'}^{plm}(r)$ stops changing from iteration to iteration. This procedure amounts to calculating the Born series. If the components $\chi_{l',m'}^{plm}(r)$ indeed stop changing from iteration to iteration, then a solution to the coupled-wave Lippmann-Schwinger equation has been found, which is also a positive-energy solution to the three-dimensional time-independent Schrödinger equation, with energy eigenvalue $\varepsilon = p^2/2$.

A.2 Bound-Free Transition Dipole Matrix Elements

Once the partial wave components $\chi_{l',m'}^{plm}(r)$ are obtained, by solving the CW-LSE (A.8), the full continuum state $\phi_{\mathbf{p}}^{(-)}(\mathbf{r})$ can be reconstructed via summation:

$$\phi_{\mathbf{p}}^{(-)}(\mathbf{r}) = \sum_{l,m} \sum_{l',m'} \chi_{l',m'}^{plm}(r) Y_{l',m'}(\hat{\mathbf{r}}) Y_{l,m}^*(\hat{\mathbf{p}}). \quad (\text{A.10})$$

Obviously, for numerical calculations all the summations over angular momenta have to be truncated at some sufficiently large value. But then, this poses a problem, particularly in regards to the expansion (A.5). Recall that the meaning of (A.5) is an expansion into spherical waves of the plane wave with momentum \mathbf{p} , measured *at infinity*. However, to recompose a plane wave *infinitely* far from the center requires an *infinite* number of terms in the partial wave expansion! That is, if the partial wave expansion

$$e^{i\mathbf{p}\cdot\mathbf{r}} = 4\pi \sum_{l=0}^{\infty} \sum_{m=-l}^l i^l j_l(pr) Y_{l,m}(\hat{\mathbf{r}}) Y_{l,m}^*(\hat{\mathbf{p}}) \quad (\text{A.11})$$

is truncated at some value $l = l_{\max}$, then it will accurately reproduce a plane wave only up to some distance r_0 away from the origin, after which the truncated sum turns into an utter mess. Given that photoelectrons are detected infinitely far from the interaction region, this would appear to preclude the numerical evaluation of angle-resolved photoionization cross-sections via the Lippmann-Schwinger equation.

²This actually amounts to guessing a plane wave for the full solution.

As we will see, this problem fortunately doesn't exist, because partial waves $\phi_{plm}^{(-)}$ with large angular momentum l hardly contribute to the final state in a bound-free dipole transition. To see this more clearly, recall that we're not really out to get the continuum states $\langle \mathbf{r} | \phi_{\mathbf{p}}^{(-)} \rangle$ *per se*; rather, we seek the bound-free transition dipole matrix elements $d(\mathbf{p}) = \langle \phi_{\mathbf{p}}^{(-)} | \mathbf{r} \cdot \hat{\mathbf{n}}_X | \psi \rangle$, for some electromagnetic field polarized along the unit vector $\hat{\mathbf{n}}_X$, between some initial bound state $|\psi\rangle$ and a positive-energy final state $\langle \phi_{\mathbf{p}}^{(-)} |$ that turns into a plane wave with momentum \mathbf{p} at infinity. This matrix element can be represented as an integral over space,

$$d(\mathbf{p}) = \int d^3r (\hat{\mathbf{r}} \cdot \hat{\mathbf{n}}_X) \psi(\mathbf{r}) r \phi_{\mathbf{p}}^{*(-)}(\mathbf{r}). \quad (\text{A.12})$$

Notice that the dot product $\hat{\mathbf{r}} \cdot \hat{\mathbf{n}}_X$ is just the cosine of the angle between the unit vectors $\hat{\mathbf{r}}$ and $\hat{\mathbf{n}}_X$. This is just a first-order Legendre polynomial, which we can expand into spherical harmonics as

$$\hat{\mathbf{r}} \cdot \hat{\mathbf{n}}_X = \frac{4\pi}{3} \sum_{n=-1}^1 Y_{1,n}^*(\hat{\mathbf{n}}_X) Y_{1,n}(\hat{\mathbf{r}}). \quad (\text{A.13})$$

According to (A.13), for an electromagnetic field polarized along the z -axis, only the $n = 0$ term contributes to the sum, while for a field polarized in the xy -plane, only the $n = \pm 1$ terms contribute.

Now, using the complete expansion (A.10) of the scattering wave in terms of partial wave components $\chi_{l',m'}^{plm}(r)$, and introducing the partial wave expansion of the initial state,

$$\psi(\mathbf{r}) = \sum_{\lambda=0}^{\infty} \sum_{\mu=-\lambda}^{\lambda} \psi_{\lambda,\mu}(r) Y_{\lambda,\mu}(\hat{\mathbf{r}}), \quad (\text{A.14})$$

the matrix element $d(\mathbf{p})$ may now be expressed as a linear combination

$$d(\mathbf{p}) = \sum_{n=-1}^1 \sum_{l=0}^{\infty} \sum_{m=-l}^l d_{l,m}^n(p) \quad (\text{A.15})$$

of spherical matrix elements $d_{l,m}^n(p)$, which are given by

$$\begin{aligned} d_{l,m}^n(p) &= \sqrt{\frac{4\pi}{3}} \sum_{l',m'} \sum_{\lambda,\mu} (-1)^{m'+n} \sqrt{(2\lambda+1)(2l'+1)} \begin{pmatrix} 1 & \lambda & l' \\ 0 & 0 & 0 \end{pmatrix} \\ &\quad \times \begin{pmatrix} 1 & \lambda & l' \\ -n & \mu & -m' \end{pmatrix} \int_0^{\infty} r^3 dr \psi_{\lambda,\mu}(r) \chi_{l',m'}^{*plm}(r). \end{aligned} \quad (\text{A.16})$$

Expression (A.16) for the spherical matrix elements solves the problem I previously raised regarding the truncation of the partial wave expansion (A.5) at some $l = l_{\max}$. This issue can now be clarified straightforwardly. Notice that the magnitude of the transition

matrix elements is directly related to the amount of overlap between the initial and final states. This overlap is represented by the integral in (A.16), in which the states are resolved in angular momentum. Since the partial wave components $\chi_{l',m'}^{plm}(r)$ of the final states are hurred out to larger radial distances for larger values of l , their overlap with the initial state's main components $\psi_{\lambda,\mu}(r)$, which are localized near $r = 0$, quickly goes to zero as l becomes larger. This means that the series expansion (A.5) of the plane wave scattering states into spherical scattering states can be safely truncated at some value $l = l_{\max}$.

A.3 Scattering States for a Long Range Potential

In realistic systems, with the exception of singly-negative ions, the photoelectron feels the *Coulomb* attraction of its parent ion. The Coulomb interaction creates a scattering potential which has the *worst* possible features: (i) it has a long range, falling off rather slowly as $-Z/r$ (where Z is the ionic charge), and (ii) it has a singularity at the origin³. The reason why I say it's the worst possible potential, is that it's just *barely* workable to be part of physics. If it was, say, the Weierstrass function, physicists could just leave it to the mathematicians to deal with!

In any event, the Coulomb potential poses a real problem: I currently solve the LSE by computing the Born series, which converges provided that the scattering potential is sufficiently weak. Indeed, it goes without saying that it takes quite an energetic photoelectron to see a “weak” Coulomb potential. In more rigorous terms, the convergence of the Born series is hindered by the long-range and singular nature of the Coulomb potential. In this section, I address this issue by making use of another feature of the LSE: the freedom to choose how to partition the full Hamiltonian $H = H_0 + V(\mathbf{r})$.

The simplest system with a long-range $-Z/r$ potential is the hydrogenic atom, described by the time-independent single-electron Schrödinger equation

$$-\frac{1}{2}\nabla^2\phi_{\mathbf{p}}^{(\pm)}(\mathbf{r}) - \frac{Z}{r}\phi_{\mathbf{p}}^{(\pm)}(\mathbf{r}) = \frac{p^2}{2}\phi_{\mathbf{p}}^{(\pm)}. \quad (\text{A.17})$$

Keeping the scattering picture in mind, the label “ (\pm) ” is attached to the solutions, in reference to incoming “ $(-)$ ” or outgoing “ $(+)$ ” scattering states. Since the $-Z/r$ potential goes to zero as $r \rightarrow \infty$, the solutions of (A.17) should asymptotically behave as free-particle waves. Therefore, we can again assume plane wave asymptotics, such that $\phi_{\mathbf{p}}^{(\pm)}(\mathbf{r})$ behaves as a plane wave with momentum \mathbf{p} at infinity. In fact, such a wave function $\phi_{\mathbf{p}}^{(\pm)}(\mathbf{r})$ is a known solution to the hydrogenic potential, and is called a *Coulomb scattering wave*:

$$\phi_{\mathbf{p}}^{(\pm)}(\mathbf{r}) = e^{-\frac{1}{2}\pi\eta}\Gamma(1 \pm i\eta)e^{i\mathbf{p}\cdot\mathbf{r}}{}_1F_1(\mp i\eta, 1, \pm i(kr \mp \mathbf{p} \cdot \mathbf{r})), \quad (\text{A.18})$$

³Granted, it's an integrable singularity, but it's still quite an annoyance, given that there is also a singularity due to the Green's function!

where ${}_1F_1(a, b, c)$ is a confluent hypergeometric function of the first kind⁴, and $\eta = -Z/p$ is the Sommerfeld parameter.

The spherical scattering states $\phi_{plm}^{(\pm)}(\mathbf{r})$, again given as partial wave components of the plane wave scattering states,

$$\phi_{\mathbf{p}}^{(\pm)}(\mathbf{r}) = \sum_{l=0}^{\infty} \sum_{m=-l}^l \phi_{plm}^{(\pm)}(\mathbf{r}) Y_{l,m}^*(\hat{\mathbf{p}}), \quad (\text{A.19})$$

are also solutions to (A.17). Recall that these states represent the scattering of a spherical wave incident upon the scattering potential. Now, because the scattering potential $-Z/r$ is spherically symmetric, it preserves the angular momentum of the incident spherical wave. Therefore the angular and radial parts of $\phi_{plm}^{(\pm)}(\mathbf{r})$ may be separated, and no partial wave expansion of $\phi_{plm}^{(\pm)}(\mathbf{r})$ is required. In fact, the states $\phi_{plm}^{(\pm)}(\mathbf{r})$ which solve A.17 are the *spherical Coulomb waves*, given by

$$\phi_{plm}^{(\pm)}(\mathbf{r}) = \sqrt{\frac{2}{\pi}} i^l e^{\pm i\sigma_l} \frac{F_l(pr; \eta)}{pr} Y_{l,m}(\hat{\mathbf{r}}), \quad (\text{A.20})$$

where $\sigma_l = \arg(\Gamma(l+1+i\eta))$ is called the *Coulomb phase shift*, and $F_l(pr; \eta)$ is the *radial Coulomb wave function*, given by

$$F_l(\rho; \eta) = 2^l \rho^{l+1} e^{-(i\rho + \frac{1}{2}\pi\eta)} \frac{|\Gamma(1+l+i\eta)|}{\Gamma(2l+2)} {}_1F_1(1+l-i\eta, 2l+2, 2i\rho). \quad (\text{A.21})$$

The spherical Coulomb wave (A.20) is reminiscent of the free spherical wave, given by the first term on the RHS of (A.6), where the role of the Bessel function is played by $e^{\pm i\sigma_l} F_l(pr; \eta)/(pr)$.

Now, just as the spherical Bessel function $j_l(\rho)$ has a linearly independent and singular (at the origin $r=0$) counterpart $y_l(\rho)$, $F_l(\rho; \eta)$ also has a linearly independent big brother $G_l(\rho; \eta)$, which is singular at the origin $\rho=0$. Naturally, $e^{\pm i\sigma_l} F_l(\rho; \eta)/\rho$ and $e^{\pm i\sigma_l} G_l(\rho; \eta)/\rho$ become $j_l(pr)$ and $y_l(pr)$, respectively, as $Z \rightarrow 0$.

Although $F_l(\rho; \eta)$ and $G_l(\rho; \eta)$ are quite difficult to compute numerically—requiring the evaluation continued fractions, recursion relations, definite integrals, asymptotic expansions, expansions in Airy, Bessel, or Bessel-Clifford functions—they can be taken as *known* functions.

We are now in a position to deal with the problem of computing scattering states for a more general potential $V^{(Z)}(\mathbf{r})$ that behaves like $-Z/r$ as $r \rightarrow \infty$. The Hamiltonian for an electron moving in such a potential can be written as

$$H = \underbrace{\frac{p^2}{2} - \frac{Z}{r}}_{H^{(C)}} + \underbrace{V^{(Z)}(\mathbf{r}) + \frac{Z}{r}}_{V^{(R)}(\mathbf{r})}, \quad (\text{A.22})$$

⁴I'm sure the only reason why everyone specifies the name of ${}_1F_1(a, b, c)$ is because it sounds cool. The phrase “confluent hypergeometric function of the first kind” hardly adds anything of value to a physics discussion, but hopefully it'll make me look smart ahead of my defense!

where the term Z/r is explicitly added to and subtracted from the total Hamiltonian H . Using this trick, it's clear that, although $V_Z(\mathbf{r})$ isn't a perturbation to the free-particle Hamiltonian $p^2/2$, the "reduced" potential $V^{(R)}(\mathbf{r})$ may be a perturbation to the Coulomb Hamiltonian $H^{(C)}$. This potential, whose long-range $-Z/r$ behavior has been eliminated, now falls off at least as fast as $1/r^2$. Based on these considerations, we can apply the Lippmann-Schwinger formalism previously developed by taking the unperturbed Hamiltonian as $H_0 = H^{(C)}$ and the scattering potential as $V(\mathbf{r}) = V^{(R)}(\mathbf{r})$, and then generalizing free spherical waves to spherical Coulomb waves: $\sqrt{2/\pi}j_l(pr) \rightarrow e^{-i\sigma_l}F_l(pr; \eta)/(pr)$, $\sqrt{2/\pi}y_l(pr) \rightarrow e^{-i\sigma_l}G_l(pr; \eta)/(pr)$. The CW-LSE (A.8) then becomes

$$\begin{aligned} \chi_{l'm'}^{plm}(r) = & \frac{1}{pr} \left(\sqrt{\frac{2}{\pi}} i^l e^{-i\sigma_l} F_l(pr) \delta_{l,l'} \delta_{m,m'} \right. \\ & + (-1)^{m'} \sqrt{\frac{2l'+1}{\pi}} \sum_{\lambda,\mu} \sum_{\kappa,\nu} \sqrt{(2\kappa+1)(2\lambda+1)} \begin{pmatrix} \kappa & \lambda & l' \\ 0 & 0 & 0 \end{pmatrix} \\ & \times \begin{pmatrix} \kappa & \lambda & l' \\ \nu & \mu & -m' \end{pmatrix} \int_0^\infty r' dr' F_{l'}(pr_{<}) (G_{l'}(pr_{>}) + iF_{l'}(pr_{>})) v_{\kappa,\nu}(r') \chi_{\lambda,\mu}^{plm}(r') \Big). \end{aligned} \quad (\text{A.23})$$

A.4 A Treatment of the Scattering Potential for Atoms and Molecules

So far the treatment presented in this Appendix applies to a general local⁵ potential $V(\mathbf{r})$, and one which may possess only integrable singularities and must asymptotically fall off at least as fast as $1/r$ as $r \rightarrow \infty$. Since the scattering theory laid out in this section is within the context of electron-atom and electron-molecule collisions, it is instructive to have a closer look at the form of the scattering potential for this particular class of processes.

Neglecting the exchange interaction between the free (positive-energy) electron and the bound ones, the scattering potential $V^{(Z)}(\mathbf{r})$ appearing in (A.22) can be broken down into two contributions:

$$V^{(Z)}(\mathbf{r}) = \underbrace{-\sum_{n=1}^N \frac{Z_n}{|\mathbf{r} - \mathbf{R}_n|}}_{V^{(N)}(\mathbf{r})} + V^{(e)}(\mathbf{r}), \quad (\text{A.24})$$

where the first term on the RHS of (A.24) is just the sum of Coulomb potentials due to the N nuclei located at positions \mathbf{R}_n with charges Z_n , and $V^{(e)}(\mathbf{r})$ is the electrostatic shielding potential, due to the bound electrons, felt by the free electron.

⁵By "local" I mean a potential that does not make an electron suddenly jump from one spatial location to another, i.e. $\langle \mathbf{r}' | V(\mathbf{r}) | \mathbf{r} \rangle = V(\mathbf{r}) \delta^3(\mathbf{r} - \mathbf{r}')$.

Given a set of bound electron orbitals $\{\psi_k(\mathbf{r})\}$ obtained e.g. via a self-consistent field calculation, the electronic charge density is just given by

$$\rho(\mathbf{r}) = \sum_k m_k |\psi_k(\mathbf{r})|^2, \quad (\text{A.25})$$

where $m_k = 0, 1$ or 2 is the occupation number of the k th orbital. From this definition, we note that

$$Z = \sum_{n=1}^N Z_n - \int d^3r \rho(\mathbf{r}), \quad (\text{A.26})$$

such that $V^{(Z)}(r) \rightarrow -Z/r$ as $r \rightarrow \infty$.

Now, assuming that the electrons and nuclei don't move during the course of photoionization (i.e. $\rho(\mathbf{r})$ and $\{\mathbf{R}_n\}$ are time-independent), we may derive the scattering potential $V^{(e)}(\mathbf{r})$ using electrostatics. Basically, $V^{(e)}(\mathbf{r})$ satisfies the Poisson equation $\nabla^2 V^{(e)}(\mathbf{r}) = -4\pi\rho(\mathbf{r})$ (recall that atomic units are used throughout). The solution to Poisson's equation can be represented in integral form as

$$V^{(e)}(\mathbf{r}) = \int d^3r' \frac{\rho(\mathbf{r}')}{|\mathbf{r} - \mathbf{r}'|} = \sum_k m_k \int d^3r' \frac{\phi_k^*(\mathbf{r}')\phi_k(\mathbf{r}')}{|\mathbf{r} - \mathbf{r}'|}, \quad (\text{A.27})$$

which is just the Coulomb operator from Hartree-Fock theory.

Now, since we have previously expanded all quantities in partial waves, we might as well treat $V^{(e)}(\mathbf{r})$ in a similar manner. Making use of the following partial wave expansions

$$V^{(e)}(\mathbf{r}) = \sum_{l=0}^{\infty} \sum_{m=-l}^l v_{l,m}^{(e)}(r) Y_{l,m}(\hat{\mathbf{r}}), \quad (\text{A.28a})$$

$$\rho(\mathbf{r}) = \sum_{l=0}^{\infty} \sum_{m=-l}^l \varrho_{l,m}(r) Y_{l,m}(\hat{\mathbf{r}}), \quad (\text{A.28b})$$

$$\frac{1}{|\mathbf{r} - \mathbf{r}'|} = \sum_{l=0}^{\infty} \sum_{m=-l}^l \frac{4\pi}{2l+1} \frac{r_{<}^l}{r_{>}^{l+1}} Y_{l,m}(\hat{\mathbf{r}}) Y_{l,m}^*(\hat{\mathbf{r}}'), \quad (\text{A.28c})$$

the partial wave components $v_{l,m}^{(e)}(r)$ of the electronic shielding potential are given by

$$v_{l,m}^{(e)}(r) = \frac{4\pi}{2l+1} \int_0^{\infty} \varrho_{l,m}(r') \frac{r_{<}^l}{r_{>}^{l+1}} r'^2 dr' \quad (\text{A.29a})$$

$$= \frac{4\pi}{2l+1} \left(\frac{1}{r^{l+1}} \int_0^r r'^{l+2} \varrho_{l,m}(r') dr' + r^l \int_r^{\infty} \frac{\varrho_{l,m}(r')}{r'^{l-1}} dr' \right). \quad (\text{A.29b})$$

One can avoid reevaluating the definite integrals in (A.29b) for each value of r —which would require $\mathcal{O}(n^2)$ operations, n being the number of radial grid points—by instead

using the following trick. If we call the first and second integral on the RHS of (A.29b) $I_{l,m}^{(1)}(r)$ and $I_{l,m}^{(2)}(r)$, respectively, we may evaluate them simply by propagating two ordinary differential equations with obvious initial conditions:

$$\frac{d}{dr} I_{l,m}^{(1)}(r) = r^{l+2} \varrho_{l,m}(r), \quad I_{l,m}^{(1)}(0) = 0 \quad (\text{A.30a})$$

$$\frac{d}{dr} I_{l,m}^{(2)}(r) = -\frac{\varrho_{l,m}(r)}{r^{l-1}}, \quad I_{l,m}^{(2)}(\infty) = 0. \quad (\text{A.30b})$$

Thus by propagating (A.30a) from $r = 0$ to $r = R$ and back-propagating (A.30b) from $r = R$ to $r = 0$ (of course choosing R to be sufficiently large), $v_{l,m}^{(e)}(r)$ can be computed on a radial grid in $\mathcal{O}(n)$ operations.

Finally, by decomposing the scattering potential $V^{(N)}(\mathbf{r})$ due to the nuclei using the Laplace expansion (A.28c), we represent the partial wave components $v_{l,m}^{(Z)}(r)$ of the total scattering potential $V^{(Z)}(\mathbf{r})$ as

$$v_{l,m}^{(Z)}(r) = \frac{4\pi}{2l+1} \left(-\sum_{n=1}^N Z_n \frac{R_{n<}^l}{R_{n>}^{l+1}} Y_{l,m}^*(\hat{\mathbf{R}}_n) + \int_0^\infty \varrho_{l,m}(r') \frac{r_{<}^l}{r_{>}^{l+1}} r'^2 dr' \right), \quad (\text{A.31})$$

$$\text{with } R_{n<} = \min(r, |\mathbf{R}_n|) \text{ and } R_{n>} = \max(r, |\mathbf{R}_n|).$$

For electron-atom or electron-molecule collisions, it is precisely $v_{l,m}(r) = v_{l,m}^{(Z)}(r) + \delta_{l,0}Z/r$ that should be used in (A.23) for computing the scattering states. As mentioned, this treatment of the potential neglects the exchange interaction between the free and bound electrons. This interaction becomes less important at higher energies, and seeing as the Born series expansion for computing the scattering states, as outlined in this Appendix, converges for sufficiently high energies, (A.31) should provide sufficient accuracy to qualitatively model scattering or photoionization experiments.

If better quantitative agreement is needed, it is necessary to include the non-local exchange interaction between the free electron and the bound electrons as an extra term in the scattering potential. If the bound electrons are represented by a set of orbitals $\{\phi_k(\mathbf{r})\}$, then this non-local scattering potential has matrix elements

$$W(\mathbf{r}, \mathbf{r}') = \langle \mathbf{r} | W | \mathbf{r}' \rangle = - \sum_k \frac{\phi_k^*(\mathbf{r}') \phi_k(\mathbf{r})}{|\mathbf{r} - \mathbf{r}'|} \quad (\text{A.32a})$$

$$\text{such that } \langle \mathbf{r} | W | \psi \rangle = \int d^3r' W(\mathbf{r}, \mathbf{r}') \psi(\mathbf{r}') = - \sum_k \phi_k(\mathbf{r}) \int \frac{\phi_k^*(\mathbf{r}') \psi(\mathbf{r}')}{|\mathbf{r} - \mathbf{r}'|} d^3r'. \quad (\text{A.32b})$$

This non-local scattering potential may also be decomposed into partial waves [213, 214, 58, 27, 8]

$$W(\mathbf{r}, \mathbf{r}') = \sum_{l=0}^{\infty} \sum_{m=-l}^l w_l(r, r') Y_{l,m}(\hat{\mathbf{r}}) Y_{l,m}^*(\hat{\mathbf{r}}'), \quad (\text{A.33})$$

and then included into the formalism outlined in this Appendix, with the additional approximation that its partial wave components be separable, i.e. $w_l(r, r') \simeq q_l(r) q_l(r')$.

Appendix B

A Little Bit of This and a Little Bit of That

B.1 The Obligatory Coordinate Transformations

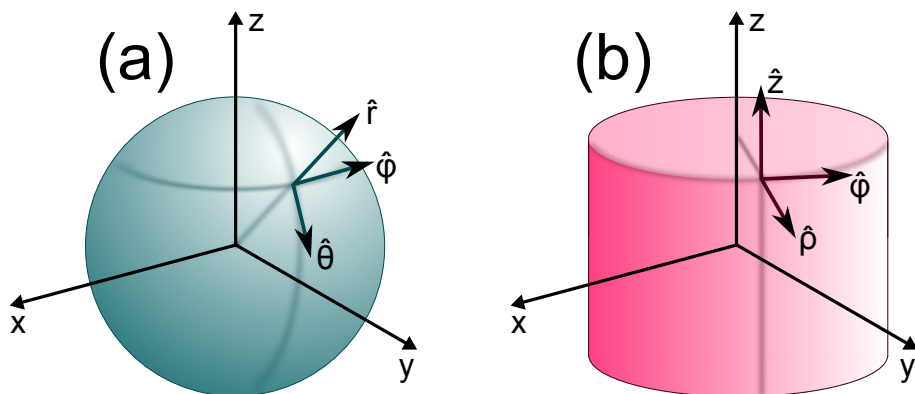


Figure B.1: Illustrations of the unit vectors pertaining to spherical (a) and cylindrical (b) coordinate systems. The rectangular (Cartesian) components \hat{x} , \hat{y} and \hat{z} (not shown) are just unit vectors oriented along the x , y and z axes, respectively.

This section is generally useful, but not particularly so in the context of this thesis. The rectangular, cylindrical and spherical coordinate systems are the most widely used in science and engineering. Although these tables can be found pretty much everywhere, especially now in the age of the internet, I reckon a little redundancy is not so bad. In the unlikely event that the internet goes down like the Library of Alexandria, well, you can always find a hard copy of these tables here. Really, my good conscience was pushing me to include them just for the sake of completeness. So here they are, for your own enjoyment during your Sunday morning coffee.

| the coordinate | rectangular coordinates | cylindrical coordinates | spherical coordinates |
|-------------------|---|--------------------------------------|---------------------------|
| x | x | $\rho \cos \phi$ | $r \sin \theta \cos \phi$ |
| y | y | $\rho \sin \phi$ | $r \sin \theta \sin \phi$ |
| z | z | z | $r \cos \theta$ |
| ρ | $\sqrt{x^2 + y^2}$ | ρ | $r \sin \theta$ |
| ϕ | $\arctan\left(\frac{y}{x}\right)$ | ϕ | ϕ |
| r | $\sqrt{x^2 + y^2 + z^2}$ | $\sqrt{\rho^2 + z^2}$ | r |
| θ | $\arctan\left(\frac{1}{z}\sqrt{x^2 + y^2}\right)$ | $\arctan\left(\frac{\rho}{z}\right)$ | θ |

Table B.1: Transformations between rectangular, cylindrical and spherical coordinates; the notation used here is such that the coordinate of \mathbf{v} along the direction of $\hat{\mathbf{a}}$ is $a = \mathbf{v} \cdot \hat{\mathbf{a}}$.

| unit vector | rectangular coordinates | cylindrical coordinates | spherical coordinates |
|-----------------------------|--|---|--|
| $\hat{\mathbf{x}}$ | $\hat{\mathbf{x}}$ | $\cos \phi \hat{\boldsymbol{\rho}} - \sin \phi \hat{\boldsymbol{\phi}}$ | $\sin \theta \cos \phi \hat{\mathbf{r}} + \cos \theta \cos \phi \hat{\boldsymbol{\theta}} - \sin \phi \hat{\boldsymbol{\phi}}$ |
| $\hat{\mathbf{y}}$ | $\hat{\mathbf{y}}$ | $\sin \phi \hat{\boldsymbol{\rho}} + \cos \phi \hat{\boldsymbol{\phi}}$ | $\sin \theta \sin \phi \hat{\mathbf{r}} + \cos \theta \sin \phi \hat{\boldsymbol{\theta}} + \cos \phi \hat{\boldsymbol{\phi}}$ |
| $\hat{\mathbf{z}}$ | $\hat{\mathbf{z}}$ | $\hat{\mathbf{z}}$ | $\cos \theta \hat{\mathbf{r}} - \sin \theta \hat{\boldsymbol{\theta}}$ |
| $\hat{\boldsymbol{\rho}}$ | $\cos \phi \hat{\mathbf{x}} + \sin \phi \hat{\mathbf{y}}$ | $\hat{\boldsymbol{\rho}}$ | $\sin \theta \hat{\mathbf{r}} + \cos \theta \hat{\boldsymbol{\theta}}$ |
| $\hat{\boldsymbol{\phi}}$ | $-\sin \phi \hat{\mathbf{x}} + \cos \phi \hat{\mathbf{y}}$ | $\hat{\boldsymbol{\phi}}$ | $\hat{\boldsymbol{\phi}}$ |
| $\hat{\mathbf{r}}$ | $\sin \theta \cos \phi \hat{\mathbf{x}} + \sin \theta \sin \phi \hat{\mathbf{y}} + \cos \theta \hat{\mathbf{z}}$ | $\sin \theta \hat{\boldsymbol{\rho}} + \cos \theta \hat{\mathbf{z}}$ | $\hat{\mathbf{r}}$ |
| $\hat{\boldsymbol{\theta}}$ | $\cos \theta \cos \phi \hat{\mathbf{x}} + \cos \theta \sin \phi \hat{\mathbf{y}} - \sin \theta \hat{\mathbf{z}}$ | $\cos \theta \hat{\boldsymbol{\rho}} - \sin \theta \hat{\mathbf{z}}$ | $\hat{\boldsymbol{\theta}}$ |

Table B.2: Orthogonal unit vectors $\hat{\mathbf{x}}$, $\hat{\mathbf{y}}$, $\hat{\mathbf{z}}$, $\hat{\boldsymbol{\rho}}$, $\hat{\boldsymbol{\phi}}$, $\hat{\mathbf{r}}$, $\hat{\boldsymbol{\theta}}$ in rectangular, cylindrical and spherical coordinates.

| differential operation | rectangular coordinates | cylindrical coordinates | spherical coordinates |
|----------------------------|--|--|---|
| Θf | $x \frac{\partial f}{\partial x} + y \frac{\partial f}{\partial y} + z \frac{\partial f}{\partial z}$ | $\rho \frac{\partial f}{\partial \rho} + z \frac{\partial f}{\partial z}$ | $r \frac{\partial f}{\partial r}$ |
| ∇f | $\frac{\partial f}{\partial x} \hat{\mathbf{x}} + \frac{\partial f}{\partial y} \hat{\mathbf{y}} + \frac{\partial f}{\partial z} \hat{\mathbf{z}}$ | $\frac{\partial f}{\partial \rho} \hat{\boldsymbol{\rho}} + \frac{1}{\rho} \frac{\partial f}{\partial \phi} \hat{\boldsymbol{\phi}} + \frac{\partial f}{\partial z} \hat{\mathbf{z}}$ | $\frac{\partial f}{\partial r} \hat{\mathbf{r}} + \frac{1}{r} \frac{\partial f}{\partial \theta} \hat{\boldsymbol{\theta}} + \frac{1}{r \sin \theta} \frac{\partial f}{\partial \phi} \hat{\boldsymbol{\phi}}$ |
| $\nabla^2 f$ | $\frac{\partial^2 f}{\partial x^2} + \frac{\partial^2 f}{\partial y^2} + \frac{\partial^2 f}{\partial z^2}$ | $\frac{1}{\rho} \frac{\partial}{\partial \rho} (\rho \frac{\partial f}{\partial \rho}) + \frac{1}{\rho^2} \frac{\partial^2 f}{\partial \phi^2} + \frac{\partial^2 f}{\partial z^2}$ | $\frac{1}{r^2} \frac{\partial}{\partial r} (r^2 \frac{\partial f}{\partial r}) + \frac{1}{r^2 \sin \theta} \frac{\partial}{\partial \theta} (\sin \theta \frac{\partial f}{\partial \theta}) + \frac{1}{r^2 \sin^2 \theta} \frac{\partial^2 f}{\partial \phi^2}$ |
| $\nabla \cdot \mathbf{f}$ | $\frac{\partial f_x}{\partial x} + \frac{\partial f_y}{\partial y} + \frac{\partial f_z}{\partial z}$ | $\frac{1}{\rho} \frac{\partial}{\partial \rho} (\rho f_\rho) + \frac{1}{\rho} \frac{\partial f_\phi}{\partial \phi} + \frac{\partial f_z}{\partial z}$ | $\frac{1}{r^2} \frac{\partial}{\partial r} (r^2 f_r) + \frac{1}{r \sin \theta} \frac{\partial}{\partial \theta} (\sin \theta f_\theta) + \frac{1}{r \sin \theta} \frac{\partial f_\phi}{\partial \phi}$ |
| $\nabla \times \mathbf{f}$ | $\begin{pmatrix} \frac{\partial f_z}{\partial y} - \frac{\partial f_y}{\partial z} \\ \frac{\partial f_x}{\partial z} - \frac{\partial f_z}{\partial x} \\ \frac{\partial f_y}{\partial x} - \frac{\partial f_x}{\partial y} \end{pmatrix} \begin{matrix} \hat{\mathbf{x}} \\ \hat{\mathbf{y}} \\ \hat{\mathbf{z}} \end{matrix}$ | $\begin{pmatrix} \frac{1}{\rho} \frac{\partial f_z}{\partial \phi} - \frac{\partial f_\phi}{\partial z} \\ \frac{\partial f_\rho}{\partial z} - \frac{\partial f_z}{\partial \rho} \\ \frac{\partial}{\partial \rho} (\rho f_\phi) - \frac{\partial f_\rho}{\partial \phi} \end{pmatrix} \begin{matrix} \hat{\boldsymbol{\rho}} \\ \hat{\boldsymbol{\phi}} \\ \hat{\mathbf{z}} \end{matrix}$ | $\begin{pmatrix} \frac{1}{r \sin \theta} \left(\frac{\partial}{\partial \theta} (\sin \theta f_\phi) - \frac{\partial f_\theta}{\partial \phi} \right) \\ + \frac{1}{r} \left(\frac{1}{\sin \theta} \frac{\partial f_r}{\partial \phi} - \frac{\partial}{\partial r} (r f_\phi) \right) \\ + \frac{1}{r} \left(\frac{\partial}{\partial r} (r f_\theta) - \frac{\partial f_r}{\partial \theta} \right) \end{pmatrix} \begin{matrix} \hat{\mathbf{r}} \\ \hat{\boldsymbol{\theta}} \\ \hat{\boldsymbol{\phi}} \end{matrix}$ |

Table B.3: A few of the most common differential operators, acting on a scalar field f and a vector field \mathbf{f} ; the notation f_a denotes the component of \mathbf{f} along the unit vector $\hat{\mathbf{a}}$.

B.2 The Beloved Atomic Units

Having been consumed by their passion and love for atomic units, atomic physicists tend to forget how to relate to their measurement devices. Such a communication breakdown is typical between two genders, despite their best efforts to relate to one another. Atomic physicists, on the one hand, speak in atomic units, while their significant others (their measurement devices) speak in French, in the *Système international d'unités* (SI). In an attempt to solve this lingering problem, Table B.4 and Table B.5 are meant to bridge this communication gap, and rekindle the fire.

| name and symbol | | value in SI units | value in atomic units (a.u.) |
|--|-----------------|--|---|
| Avogadro's number | N_A | $6.02214179 \times 10^{23}$ 1/mol | $6.02214179 \times 10^{23}$ 1/mol |
| Bohr's magneton | μ_B | $9.2740154 \times 10^{-24}$ C m ² /s | 5.0×10^{-1} $e\hbar/m_e$ |
| Bohr's radius | a_0 | $5.2917720859 \times 10^{-11}$ m | 1×10^0 a_0 |
| Boltzmann's constant | k_B | $1.3806504 \times 10^{-23}$ kg m ² /s ² K | 1×10^0 k_B |
| the Compton wavelength of the electron | λ_e | $2.4263102175 \times 10^{-12}$ m | $4.58506182 \times 10^{-2}$ a_0 |
| Coulomb's constant | k_e | 8.987551788×10^9 kg m ² /s ² C ² | 1×10^0 $\hbar^2/m_e a_0 e^2$ |
| Dirac's constant | \hbar | $1.054571628 \times 10^{-34}$ kg m ² /s | 1×10^0 \hbar |
| the electron's charge | e | $1.602176487 \times 10^{-19}$ C | 1×10^0 e |
| the electron's classical radius | r_e | 2.81794×10^{-15} m | 5.3251354×10^{-5} a_0 |
| the electron's g-factor | g_e | -2.0023193×10^1 | -2.0023193×10^1 |
| the electron's mass | m_e | $9.10938215 \times 10^{-31}$ kg | 1×10^0 m_e |
| an electron volt | eV | $1.602176487 \times 10^{-19}$ kg m ² /s ² | $3.67493254 \times 10^{-2}$ $\hbar^2/m_e a_0^2$ |
| the fine structure constant | α | $7.2973525376 \times 10^{-3}$ | $7.29735254 \times 10^{-3}$ |
| the gravitational constant | G | 6.67428×10^{-11} m ³ /kg s ² | 2.4006×10^{-43} $\hbar^2/m_e^3 a_0$ |
| the ideal gas constant | R | 8.314472×10^0 kg m ² /s ² mol K | $6.02214179 \times 10^{23}$ k_B /mol |
| the neutron's mass | m_n | $1.674927211 \times 10^{-27}$ kg | 1.83868366×10^3 m_e |
| the proton's mass | m_p | $1.672621637 \times 10^{-27}$ kg | 1.83615267×10^3 m_e |
| Rydberg's wave number | R_∞ | 1.097373157×10^7 1/m | 5.8070486×10^{-4} $1/a_0$ |
| the speed of light | c | 2.99792458×10^8 m/s | 1.37036×10^2 $\hbar/m_e a_0$ |
| the Stefan-Boltzmann constant | σ | 5.6704×10^{-8} kg/s ³ K ⁴ | 8.759496×10^{-6} $m_e^2 a_0^2 k_B^4/\hbar^5$ |
| the vacuum's permeability | μ_0 | $1.2566370614 \times 10^{-6}$ kg m/C ² | $6.69176251 \times 10^{-4}$ $m_e a_0/e^2$ |
| the vacuum's permittivity | ε_0 | $8.854187817 \times 10^{-12}$ s ² C ² /m ³ kg | $7.95774715 \times 10^{-2}$ $m_e a_0 e^2/\hbar^2$ |

Table B.4: Physical constants in SI and atomic units

| physical quantity | atomic unit | value in SI units |
|---|----------------------------------|---|
| acceleration | $\hbar^2/m_e^2 a_0^3$ | $9.044216074 \times 10^{22} \text{ m/s}^2$ |
| angular momentum | \hbar | $1.054571628 \times 10^{-34} \text{ kg m}^2/\text{s}$ |
| area | a_0^2 | $2.800285181 \times 10^{-21} \text{ m}^2$ |
| electric capacitance | $m_e a_0^2 e^2 / \hbar^2$ | $5.887890513 \times 10^{-21} \text{ C}^2 \text{ s}^2 / \text{m}^2 \text{ kg}$ |
| electric charge | e | $1.602176487 \times 10^{-19} \text{ C}$ |
| electric charge density | e/a_0^3 | $1.081202300 \times 10^{12} \text{ C/m}^3$ |
| electric conductance | e^2/\hbar | $2.434134797 \times 10^{-4} \text{ C}^2 \text{ m}^2 \text{ s/kg}$ |
| electric conductivity | $e^2/\hbar a_0$ | $4.599848137 \times 10^6 \text{ C}^2 \text{ m s/kg}$ |
| electric current | $e\hbar/m_e a_0^2$ | $6.623617625 \times 10^{-3} \text{ C/s}$ |
| electric current density | $e\hbar/m_e a_0^4$ | $2.365336813 \times 10^{18} \text{ C/m}^2 \text{ s}$ |
| electric dipole moment | $e a_0$ | $8.478352811 \times 10^{-30} \text{ C m}$ |
| electric displacement (D) | e/a_0^2 | $5.721476148 \times 10^1 \text{ C/m}^2$ |
| electric field (F) | $\hbar^2/m_e a_0^3 e$ | $5.142206313 \times 10^{11} \text{ kg m/s}^2 \text{ C}$ |
| electric flux | $\hbar^2/m_e a_0 e$ | $1.439964414 \times 10^{-9} \text{ kg m}^3/\text{s}^2 \text{ C}$ |
| electric resistance | \hbar/e^2 | $4.108235917 \times 10^3 \text{ kg/m}^2 \text{ s C}^2$ |
| electric resistivity | $\hbar a_0/e^2$ | $2.173984815 \times 10^{-7} \text{ kg/m s C}^2$ |
| electric scalar potential (ϕ) | $\hbar^2/m_e a_0^2 e$ | $2.721138383 \times 10^1 \text{ kg m}^2/\text{s}^2 \text{ C}$ |
| energy | $\hbar^2/m_e a_0^2$ | $4.359743935 \times 10^{-18} \text{ kg m}^2/\text{s}^2$ |
| energy density | $\hbar^2/m_e a_0^5$ | $2.942101077 \times 10^{13} \text{ kg/m s}^2$ |
| entropy | k_B | $1.380650400 \times 10^{-23} \text{ kg m}^2/\text{s}^2 \text{ K}$ |
| force | $\hbar^2/m_e a_0^3$ | $8.238722046 \times 10^{-8} \text{ kg m/s}^2$ |
| frequency | $\hbar/m_e a_0^2$ | $4.134137330 \times 10^{16} \text{ 1/s}$ |
| group delay dispersion | $m_e^2 a_0^4/\hbar^2$ | $5.851001394 \times 10^{-34} \text{ s}^2$ |
| gyromagnetic ratio | e/m_e | $1.758820149 \times 10^{11} \text{ C/kg}$ |
| inductance | $m_e a_0^2/e^2$ | $9.937347478 \times 10^{-14} \text{ kg m}^2/\text{C}^2$ |
| irradiance ($\frac{1}{2}\varepsilon_0 c F^2$) | $\hbar^3/m_e^2 a_0^6 8\pi\alpha$ | $3.509444930 \times 10^{20} \text{ kg/s}^3$ |
| length | a_0 | $5.291772086 \times 10^{-11} \text{ m}$ |
| magnetic dipole moment | $e\hbar/m_e$ | $1.854801828 \times 10^{-23} \text{ C m}^2/\text{s}$ |
| magnetic field (B) | $\hbar/a_0^2 e$ | $2.350517381 \times 10^5 \text{ kg/s C}$ |
| magnetic flux | \hbar/e | $6.582118990 \times 10^{-16} \text{ kg m}^2/\text{s C}$ |
| magnetic vector potential (A) | $\hbar/a_0 e$ | $1.243840226 \times 10^{-5} \text{ kg m/s C}$ |
| magnetizing field (H) | $e\hbar/m_e a_0^3$ | $1.251682332 \times 10^8 \text{ C/m s}$ |
| mass | m_e | $9.109382150 \times 10^{-31} \text{ kg}$ |
| mass density | m_e/a_0^3 | $6.147315859 \times 10^0 \text{ kg/m}^3$ |
| moment of inertia | $m_e a_0^2$ | $2.550886784 \times 10^{-51} \text{ kg m}^2$ |
| momentum | \hbar/a_0 | $1.992851564 \times 10^{-24} \text{ kg m/s}$ |
| power | $\hbar^3/m_e^2 a_0^4$ | $1.802378015 \times 10^{-1} \text{ kg m}^2/\text{s}^3$ |
| power density | $\hbar^3/m_e^2 a_0^6$ | $6.436408790 \times 10^{19} \text{ kg/s}^3$ |
| pressure | $\hbar^2/m_e a_0^5$ | $2.942101077 \times 10^{13} \text{ kg/m s}^2$ |
| temperature | $\hbar^2/m_e a_0^2 k_B$ | $3.157746476 \times 10^5 \text{ K}$ |
| time | $m_e a_0^2/\hbar$ | $2.418884328 \times 10^{-17} \text{ s}$ |
| velocity | $\hbar/m_e a_0$ | $2.187691252 \times 10^6 \text{ m/s}$ |
| viscosity | \hbar/a_0^3 | $7.116602188 \times 10^{-4} \text{ kg/m s}$ |
| volume | a_0^3 | $1.481847095 \times 10^{-31} \text{ m}^3$ |

Table B.5: The atomic units of some fundamental physical quantities.

B.3 A Simple Relation Between Bandwidth, Dispersion and Duration

Here, I prove the approximate relation

$$\tau^2 = \tau_0^2 + \gamma^2 \delta^2 \quad (\text{B.1})$$

between the duration τ , the Fourier-limited duration τ_0 , the bandwidth δ and the group-delay dispersion (GDD) γ (a constant GDD is assumed here) of a pulse with an arbitrary spectrum and constant GDD; the quantities τ , τ_0 and δ are taken as standard deviations of their respective distributions. I have not yet seen this relation anywhere in the literature, so I decided to devote this part of the Appendix to its proof, because it is quite a useful relation, e.g. the iCrap procedure wouldn't be of any use without it!

Let us first define spectral and temporal profiles as

$$\tilde{f}(\omega) = \tilde{f}_0(\omega) e^{\frac{i}{2}\gamma\omega^2} \quad (\text{B.2a})$$

$$f(t) = \frac{1}{\sqrt{2\pi}} \int_{-\infty}^{\infty} \tilde{f}(\omega) e^{i\omega t} d\omega = \mathcal{F}^{-1}[\tilde{f}(\omega)](t). \quad (\text{B.2b})$$

Let's assume, without any lack of generality in this case, that $\tilde{f}(\omega)$ and $f(t)$ are centered around $\omega = 0$ and $t = 0$, respectively.

The duration τ is defined as the standard deviation of $f(t)$, which is the square-root of the variance

$$\tau^2 = \int_{-\infty}^{\infty} t^2 |f(t)|^2 dt = \int_{-\infty}^{\infty} |-it f(t)|^2 dt = \int_{-\infty}^{\infty} \left| \mathcal{F}^{-1}[\tilde{f}'(\omega)](t) \right|^2 dt. \quad (\text{B.3})$$

In the following derivation, the prime symbol ("'") denotes differentiation with respect to the argument and the pulse is normalized according to $\int_{-\infty}^{\infty} |f(t)|^2 dt = \int_{-\infty}^{\infty} |\tilde{f}(\omega)|^2 d\omega = 1$. Assuming γ is frequency-independent, then (B.2a) implies $\tilde{f}'(\omega) = \tilde{f}'_0(\omega) e^{\frac{i}{2}\gamma\omega^2} + i\gamma\tilde{f}(\omega)$. Inserting this expression for $\tilde{f}'(\omega)$ into the rightmost-hand-side of (B.3), we obtain

$$\tau^2 = \int_{-\infty}^{\infty} |I(t; \gamma)|^2 dt + \gamma^2 \int_{-\infty}^{\infty} |f'(t)|^2 dt \quad (\text{B.4a})$$

$$+ \gamma \int_{-\infty}^{\infty} (I^*(t; \gamma) f'(t) + I(t; \gamma) f'^*(t)) dt,$$

$$I(t; \gamma) = \mathcal{F}^{-1}[\tilde{f}'_0(\omega) e^{\frac{i}{2}\gamma\omega^2}](t). \quad (\text{B.4b})$$

In analogy to (B.3), the bandwidth-limited duration is given by

$$\tau_0^2 = \int_{-\infty}^{\infty} \left| \mathcal{F}^{-1}[\tilde{f}'_0(\omega)](t) \right|^2 dt. \quad (\text{B.5})$$

Now, $I(t; \gamma)$ and $\tilde{f}'_0(\omega)e^{\frac{i}{2}\gamma\omega^2}$ are Fourier transforms of each other. Thus, from Parseval's theorem, we have

$$\int_{-\infty}^{\infty} |I(t; \gamma)|^2 dt = \int_{-\infty}^{\infty} \left| \tilde{f}'_0(\omega)e^{\frac{i}{2}\gamma\omega^2} \right|^2 d\omega = \int_{-\infty}^{\infty} \left| \tilde{f}'_0(\omega) \right|^2 d\omega = \tau_0^2, \quad (\text{B.6})$$

where (B.5) in combination with Parseval's theorem was used for the last equation on the RHS of (B.6).

The bandwidth δ is given, also in analogy to (B.3), as

$$\delta^2 = \int_{-\infty}^{\infty} \omega^2 |\tilde{f}(\omega)|^2 d\omega = \int_{-\infty}^{\infty} \left| i\omega \tilde{f}(\omega) \right|^2 d\omega. \quad (\text{B.7})$$

Since $i\omega \tilde{f}(\omega)$ and $f'(t)$ are Fourier transforms of each other, then from Parseval's theorem,

$$\delta^2 = \int_{-\infty}^{\infty} \left| i\omega \tilde{f}(\omega) \right|^2 d\omega = \int_{-\infty}^{\infty} |f'(t)|^2 dt. \quad (\text{B.8})$$

Using (B.6) and (B.8), we may now represent the duration τ as

$$\tau^2 = \tau_0^2 + \gamma^2 \delta^2 + 2\gamma \int_{-\infty}^{\infty} \Re[I^*(t; \gamma) f'(t)] dt \quad (\text{B.9a})$$

$$= \tau_0^2 + \gamma^2 \delta^2 + 2\gamma \int_{-\infty}^{\infty} \Im[\omega \tilde{f}'_0(\omega) \tilde{f}_0^*(\omega)] d\omega, \quad (\text{B.9b})$$

where we have used $I(t; \gamma) = \mathcal{F}^{-1}[\tilde{f}'_0(\omega)e^{\frac{i}{2}\gamma\omega^2}](t)$ and $f'(t) = \mathcal{F}^{-1}[i\omega \tilde{f}(\omega)](t)$ to obtain (B.9b). Now, if the pulse's GDD is constant over its spectrum, $\tilde{f}_0(\omega)$ is a strictly real quantity, and therefore the last term on the RHS of (B.9b) is exactly equal to zero, yielding (B.1), *quod erat demonstrandum*.

Relation (B.1) is the reason why iCrap can be applied for arbitrary XUV spectra (of course, provided that the attosecond pulse is short compared to the half-period of the streaking field).

Bibliography

- [1] M.J. Abel et al. , *Chem. Phys.* **366** (2009), 9.
- [2] I. Abella, *Phys. Rev. Lett.* **9** (1962), 453.
- [3] P. Agostini et al. , *Phys. Rev. Lett.* **42** (1979), 1127.
- [4] S. Akturk et al. , *Opt. Expr.* **11** (2003), 491.
- [5] M.V. Ammosov et al. , *Zh. Eksp. Teor. Fiz.* **91** (1986), 2008.
- [6] P. Antoine et al. , *Phys. Rev. Lett.* **77** (1996), 1234.
- [7] T. Baeva et al. , *Phys. Rev. E: Stat. Nonlinear Soft Matter Phys.* **74** (2006), 046404.
- [8] B. Bagchi und B. Mulligan, *Phys. Rev. C* **10** (1974), 126.
- [9] A. Bahabad et al. , *Nat. Photonics* **4** (2010), 570.
- [10] A. Baltuška et al. , *Nature* **421** (2003), 611.
- [11] A. Baltuška et al. , *Opt. Lett.* **23** (1998), 1474.
- [12] G. Birkhoff und J. von Neumann, *Annals of mathematics* **37** (1936), 823.
- [13] D. Bohm, *Phys. Rev.* **85** (1952), 166.
- [14] N. Bohr, *Philosophical magazine* **30** (1915), 394.
- [15] M. Born et al. , *Z. Phys.* **35** (1926), 557.
- [16] W. Boutu et al. , *Nat. Phys.* **4** (2008), 545.
- [17] R.W. Boyd: *Nonlinear optics*. Academic press, Burlington, MA, 2003.
- [18] T. Brabec und F. Krausz, *Phys. Rev. Lett.* **78** (1997), 3282.
- [19] T. Brabec und F. Krausz, *Rev. Mod. Phys.* **72** (2000), 545.
- [20] B.H. Bransden und C.J. Joachain: *Quantum Mechanics*. Pearson Education Limited, Harlow, Essex, 2000.

- [21] G. Breitenbach und S. Schiller, *J. Mod. Opt.* **44** (1997), 2207.
- [22] F. Brunel, *J. Opt. Soc. Am. B: Opt. Phys.* **7** (1990), 521.
- [23] S.V. Bulanov, *Phys. Plasmas* **1** (1994), 745.
- [24] S.V. Bulanov et al. , *Phys. Rev. Lett.* **91** (2003), 085001.
- [25] N. Burnett et al. , *Appl. Phys. Lett.* **31** (1977), 172.
- [26] Q. Cao et al. , *Appl. Phys. B* **77** (2003), 239.
- [27] R.L. Cassola und R.D. Koshel, *J. Phys. A: Gen. Phys.* **1** (1968), 224.
- [28] A.L. Cavalieri et al. , *Nature* **449** (2007), 1029.
- [29] A.L. Cavalieri et al. , *New J. Phys.* **9** (2007), 242.
- [30] D.W. Chandler und P.L. Houston, *J. Chem. Phys.* **87** (1987), 1445.
- [31] I.P. Christov et al. , *Phys. Rev. Lett.* **78** (1997), 1251.
- [32] H.D. Cohen und U. Fano, *Phys. Rev.* **150** (1966), 30.
- [33] J. Colgan et al. , *Phys. Rev. Lett.* **98** (2007), 153001.
- [34] P. Colosimo et al. , *Nat. Phys.* **4** (2008), 386.
- [35] E. Constant et al. , *Phys. Rev. A: At. Mol. Opt. Phys.* **56** (1997), 3870.
- [36] P.B. Corkum, *Phys. Rev. Lett.* **71** (1993), 1994.
- [37] P.B. Corkum und F. Krausz, *Nat. Phys.* **3** (2007), 381.
- [38] P.B. Corkum et al. , *Phys. Rev. Lett.* **62** (1989), 1259.
- [39] P.B. Corkum et al. , *Opt. Lett.* **19** (1994), 1870.
- [40] A. Damascelli et al. , *Rev. Mod. Phys.* **75** (2003), 473.
- [41] J. Dehmer und D. Dill, *J. Chem. Phys.* **61** (1974), 692.
- [42] N.B. Delone und V.P. Krainov, *J. Opt. Soc. Am. B: Opt. Phys.* **8** (1991), 1207.
- [43] K.W. DeLong et al. , *Opt. Lett.* **19** (1994), 2152.
- [44] A. Di Piazza et al. , *Phys. Rev. D: Part. Fields* **72** (2005).
- [45] P.A.M. Dirac, *Proc. R. Soc. London, Ser. A* **114** (1927), 243.
- [46] P.A.M. Dirac, *Rev. Mod. Phys.* **17** (1945), 195.

- [47] R. Dörner et al. , *Phys. Rep.* **330** (2000), 95.
- [48] M. Drescher et al. , *Nature* **419** (2002), 803.
- [49] B. Dromey et al. , *Nat. Phys.* **2** (2006), 456.
- [50] B. Dromey et al. , *Nat. Phys.* **5** (2009), 146.
- [51] G. Duchateau et al. , *Phys. Rev. A: At. Mol. Opt. Phys.* **63** (2001), 053411.
- [52] G. Duchateau et al. , *Phys. Rev. A: At. Mol. Opt. Phys.* **66** (2002), 023412.
- [53] N. Dudovich et al. , *Nat. Phys.* **2** (2006), 781.
- [54] H. Everett III, *Rev. Mod. Phys.* **29** (1957), 454.
- [55] U. Fano, *Rev. Mod. Phys.* **29** (1957), 74.
- [56] U. Fano und J. Cooper, *Rev. Mod. Phys.* **40** (1968), 441.
- [57] X. Feng et al. , *Opt. Expr.* **18** (2010), 1316.
- [58] P. Ferey und B. Buck, *Nuclear Physics* **32** (1962), 353 .
- [59] M. Ferray et al. , *J. Phys. B: At. Mol. Opt. Phys.* **21** (1988), L31.
- [60] R.P. Feynman, *Rev. Mod. Phys.* **20** (1948), 367.
- [61] J.R. Fienup, *Opt. Lett.* **3** (1978), 27.
- [62] J.R. Fienup, *Appl. Opt.* **21** (1982), 2758.
- [63] M. Fiess et al. , *Rev. Sci. Instrum.* **81** (2010), 093103.
- [64] D.N. Fittinghoff et al. , *Phys. Rev. Lett.* **69** (1992), 2642.
- [65] D.N. Fittinghoff et al. , *J. Opt. Soc. Am. B: Opt. Phys.* **12** (1995), 1955.
- [66] M.V. Frolov et al. , *Phys. Rev. Lett.* **102** (2009).
- [67] M.B. Gaarde, *Opt. Expr.* **8** (2001), 529.
- [68] M.B. Gaarde und K.J. Schafer, *Opt. Lett.* **31** (2006), 3188.
- [69] M.B. Gaarde et al. , *Phys. Rev. A: At. Mol. Opt. Phys.* **59** (1999), 1367.
- [70] J. Gagnon und V.S. Yakovlev, *Opt. Expr.* **17** (2009), 17678.
- [71] J. Gagnon und V.S. Yakovlev, *Appl. Phys. B* (2010), accepted.
- [72] J. Gagnon et al. , *Appl. Phys. B* **92** (2008), 25.

- [73] J. Gagnon et al. , *J. Phys. B: At. Mol. Opt. Phys.* **41** (2008), 215104.
- [74] J. Gagnon et al. , *Phys. Rev. A: At. Mol. Opt. Phys.* **82** (2010), 033435.
- [75] T.F. Gallagher, *Phys. Rev. Lett.* **61** (1988), 2304.
- [76] M. Geissler et al. , *New J. Phys.* **9** (2007).
- [77] E.A. Gibson et al. , *Science* **302** (2003), 95.
- [78] S. Gilbertson et al. , *Phys. Rev. Lett.* **105** (2010), 093902.
- [79] R.J. Glauber, *Phys. Rev.* **131** (1963), 2766.
- [80] M. Göppert-Mayer, *Ann. Phys.* **401** (1931), 273.
- [81] S. Gordienko et al. , *Phys. Rev. Lett.* **93** (2004).
- [82] K. Gottfried und T.M. Yan: *Quantum Mechanics: Fundamentals*. Springer-Verlag, New York, 2003.
- [83] E. Goulielmakis et al. , *Science* **305** (2004), 1267.
- [84] E. Goulielmakis et al. , *Science* **317** (2007), 769.
- [85] E. Goulielmakis et al. , *Science* **320** (2008), 1614.
- [86] E. Goulielmakis et al. , *Nature* **466** (2010), 739.
- [87] X. Gu et al. , *Opt. Lett.* **27** (2002), 1174.
- [88] M.C. Gutzwiller: *Chaos in Classical and Quantum Mechanics*. Springer-Verlag, New York, 1991.
- [89] S.E. Harris et al. , *Opt. Commun.* **100** (1993), 487.
- [90] D.R. Hartree, *Proc. Cambridge Philos. Soc. Math. Phys. Sciences* **24** (1928), 89.
- [91] W. Heisenberg, *Z. Phys.* **33** (1925), 879.
- [92] W. Heisenberg und H. Euler, *Z. Phys.* (1936), 714.
- [93] E.J. Heller, *J. Chem. Phys.* **75** (1981), 2923.
- [94] M. Hentschel et al. , *Nature* **414** (2001), 509.
- [95] M.G. Hofstetter et al. , *Opt. Expr.* **19** (2011), 1767.
- [96] J. Itatani et al. , *Phys. Rev. Lett.* **88** (2002), 173903.
- [97] J. Itatani et al. , *Physica Scripta* **2004** (2004), 112.

- [98] P. Johnsson et al. , *Phys. Rev. Lett.* **95** (2005), 013001.
- [99] P. Johnsson et al. , *Phys. Rev. Lett.* **99** (2007).
- [100] A.S. Kadyrov et al. , *J. Phys. B: At. Mol. Opt. Phys.* **38** (2005), 509.
- [101] D.J. Kane, *IEEE J. Select. Top. in Quantum Electron.* **4** (1998), 278.
- [102] D.J. Kane, *IEEE J. Quantum Electron.* **35** (1999), 421.
- [103] D.J. Kane, *J. Opt. Soc. Am. B: Opt. Phys.* **25** (2008), A120.
- [104] D.J. Kane, G. Rodriguez, A.J. Taylor und T.S. Clement, *J. Opt. Soc. Am. B: Opt. Phys.* **14** (1997), 935.
- [105] D.J. Kane und R. Trebino, *IEEE J. Quantum Electron.* **29** (1993), 571.
- [106] S. Kazamias und P. Balcou, *Phys. Rev. A: At. Mol. Opt. Phys.* **69** (2004), 063416.
- [107] A.K. Kazansky und N.M. Kabachnik, *J. Phys. B: At. Mol. Opt. Phys.* **39** (2006), 5173.
- [108] L.V. Keldysh, *Zh. Eksp. Teor. Fiz.* **20** (1965), 1307.
- [109] S.D. Kevan, *Phys. Rev. Lett.* **50** (1983), 526.
- [110] R. Kienberger et al. , *Nature* **427** (2004), 817.
- [111] M. Kitzler et al. , *Phys. Rev. Lett.* **88** (2002), 173904.
- [112] M.F. Kling et al. , *Science* **312** (2006), 246.
- [113] M.F. Kling et al. , *New J. Phys.* **10** (2008), 025024.
- [114] D.H. Ko et al. , *New J. Phys.* **12** (2010), 063008.
- [115] B. Kohler et al. , *Opt. Lett.* **20** (1995), 483.
- [116] S.O. Konorov et al. , *Phys. Rev. E: Stat. Nonlinear Soft Matter Phys.* **70** (2004), 057601.
- [117] A. Kornev und B. Zon, *J. Phys. B: At. Mol. Opt. Phys.* **35** (2002), 2451.
- [118] F. Krasniqi et al. , *Phys. Rev. A: At. Mol. Opt. Phys.* **81** (2010), 033411.
- [119] J.L. Krause et al. , *Phys. Rev. A: At. Mol. Opt. Phys.* **45** (1992), 4998.
- [120] J.L. Krause et al. , *Phys. Rev. Lett.* **68** (1992), 3535.
- [121] C. Lanczos, *Z. Phys.* **68** (1931), 204.

- [122] A. Levi und H. Stark, *J. Opt. Soc. Am. A* **1** (1984), 932.
- [123] M. Lewenstein et al. , *Phys. Rev. Lett.* **49** (1994), 2117.
- [124] M. Lewenstein et al. , *Phys. Rev. A: At. Mol. Opt. Phys.* **51** (1995), 1495.
- [125] A. L’Huillier et al. , *Phys. Rev. A: At. Mol. Opt. Phys.* **48** (1993), R3433.
- [126] X. Li et al. , *Phys. Rev. A: At. Mol. Opt. Phys.* **39** (1989), 5751.
- [127] R. Lichters, *Phys. Plasmas* **3** (1996), 3425.
- [128] T. Liebsch et al. , *Phys. Rev. A: At. Mol. Opt. Phys.* **52** (1995), 457.
- [129] M.A.P. Lima et al. , *Phys. Rev. A: At. Mol. Opt. Phys.* **41** (1990), 327.
- [130] F. Lindner et al. , *Phys. Rev. Lett.* **95** (2005), 040401.
- [131] R. Lopez-Martens et al. , *Phys. Rev. Lett.* **94** (2005).
- [132] R.R. Lucchese et al. , *Phys. Rev. A: At. Mol. Opt. Phys.* **25** (1982), 2572.
- [133] T.H. Maiman, *Nature* **187** (1960), 493.
- [134] Y. Mairesse und F. Quéré, *Phys. Rev. A: At. Mol. Opt. Phys.* **71** (2005), 011401.
- [135] Y. Mairesse et al. , *Science* **302** (2003), 1540.
- [136] L. Mandel und E. Wolf, *Rev. Mod. Phys.* **37** (1965), 231.
- [137] H. Mashiko et al. , *Phys. Rev. Lett.* **100** (2008), 103906.
- [138] U. Mohideen et al. , *Phys. Rev. Lett.* **71** (1993), 509.
- [139] H.G. Muller, *Appl. Phys. B* **74** (2002), s17.
- [140] Y. Nabekawa et al. , *Phys. Rev. Lett.* **96** (2006).
- [141] R.G. Newton: *Scattering theory of waves and particles*. Springer-Verlag, New York, 1982.
- [142] H. Nishioka et al. , *Opt. Lett.* **20** (1995), 2505.
- [143] M. Nisoli et al. , *Opt. Lett.* **22** (1997), 522.
- [144] Y. Nomura et al. , *Nat. Phys.* **5** (2009), 124.
- [145] G. Öhrwall et al. , *J. Phys. B: At. Mol. Opt. Phys.* **36** (2003), 3937.
- [146] D.H. Parker und A.T.J.B. Eppink, *J. Chem. Phys.* **107** (1997), 2357.

- [147] P.M. Paul et al. , *Science* **292** (2001), 1689.
- [148] G.G. Paulus et al. , *Phys. Rev. Lett.* **72** (1994), 2851.
- [149] L.Y. Peng et al. , *New J. Phys.* **10** (2008), 025030.
- [150] A.M. Perelomov et al. , *Zh. Eksp. Teor. Fiz.* **23** (1966), 924.
- [151] T. Pfeifer et al. , *Opt. Expr.* **15** (2007), 17120.
- [152] L. Plaja et al. , *J. Opt. Soc. Am. B: Opt. Phys.* **15** (1998), 1904.
- [153] T. Popmintchev et al. , *Proc. Nat. Acad. Sci. U.S.A.* **106** (2009), 10516.
- [154] M. Protopapas, *Phys. Rev. A: At. Mol. Opt. Phys.* **53** (1996), R2933.
- [155] F. Quere et al. , *Phys. Rev. Lett.* **96** (2006).
- [156] F. Quere et al. , *Phys. Rev. Lett.* **100** (2008).
- [157] L.R. R et al. , *Phys. Rev. A: At. Mol. Opt. Phys.* **22** (1980), 421.
- [158] J. Rehr und R. Albers, *Rev. Mod. Phys.* **72** (2000), 621.
- [159] J. Reichert et al. , *Opt. Commun.* **172** (1999), 59 .
- [160] T. Remetter et al. , *Nat. Phys.* **2** (2006), 323.
- [161] C. Roothaan, *Rev. Mod. Phys.* **23** (1951), 69.
- [162] L. Roso et al. , *Laser Part. Beams* **18** (2000), 467.
- [163] I.N. Ross et al. , *Opt. Commun.* **144** (1997), 125 .
- [164] S.G. Rykovanov et al. , *New J. Phys.* **10** (2008).
- [165] J.J. Sakurai: *Modern Quantum Mechanics*. Addison-Wesley, New York, 1994.
- [166] P. Salières et al. , *Science* **292** (2001), 902.
- [167] G. Sansone et al. , *Phys. Rev. Lett.* **94** (2005), 193903.
- [168] G. Sansone et al. , *Science* **314** (2006), 443.
- [169] E. Schrodinger, *Die Naturwissenschaften* **14** (1926), 664.
- [170] E. Schrodinger, *Phys. Rev.* **28** (1926), 1049.
- [171] M. Schultze et al. , *New J. Phys.* **9** (2007), 243.
- [172] M. Schultze et al. , *Science* **328** (2010), 1658.

- [173] J. Schwinger, *Phys. Rev.* **82** (1951), 664.
- [174] M.O. Scully und K. Drühl, *Phys. Rev. A: At. Mol. Opt. Phys.* **25** (1982), 2208.
- [175] T. Sekikawa et al. , *Nature* **432** (2004), 605.
- [176] Y.R. Shen: *The Principles of Nonlinear Optics*. Wiley, 1984.
- [177] B. Smirnov und M. Chibisov, *Zh. Eksp. Teor. Fiz.* **22** (1966), 585.
- [178] O. Smirnova et al. , *Phys. Rev. A: At. Mol. Opt. Phys.* **77** (2008), 033407.
- [179] I.J. Sola et al. , *Nat. Phys.* **2** (2006), 319.
- [180] A. Sommerfeld, *Ann. Phys.* **51** (1916), 1.
- [181] H. Stark et al. , *J. Opt. Soc. Am. A* **8** (1991), 566.
- [182] A. Stingl et al. , *Opt. Lett.* **20** (1995), 602.
- [183] D. Strickland und G. Mourou, *Opt. Commun.* **56** (1985), 219 .
- [184] R. Szipöcs et al. , *Opt. Lett.* **19** (1994), 201.
- [185] G. Taft et al. , *Opt. Lett.* **20** (1995), 743.
- [186] E.J. Takahashi et al. , *Phys. Rev. Lett.* **101** (2008), 253901.
- [187] K. Takatsuka und V. McKoy, *Phys. Rev. A: At. Mol. Opt. Phys.* **24** (1981), 2473.
- [188] J. Tate et al. , *Phys. Rev. Lett.* **98** (2007).
- [189] O. Tcherbakoff et al. , *Phys. Rev. A: At. Mol. Opt. Phys.* **68** (2003).
- [190] H.R. Telle et al. , *Appl. Phys. B* **69** (1999), 327.
- [191] G. Tempea et al. , *J. Opt. Soc. Am. B: Opt. Phys.* **16** (1999), 669.
- [192] C. Thaury et al. , *Nat. Phys.* **3** (2007), 424.
- [193] C. Thaury et al. , *Nat. Phys.* **4** (2008), 631.
- [194] I. Thomann et al. , *Opt. Expr.* **17** (2009), 4611.
- [195] R. Trebino: *Frequency-Resolved Optical Gating: The Measurement of Ultrashort Laser Pulses*. Kluwer Academic Publishers, 2000.
- [196] R. Trebino und D.J. Kane, *J. Opt. Soc. Am. A* **10** (1993), 1101.
- [197] R. Trebino et al. , *Rev. Sci. Instrum.* **68** (1997), 3277.

- [198] G.D. Tsakiris et al. , *New J. Phys.* **8** (2006).
- [199] P. Tzallas et al. , *Nature* **426** (2003), 267.
- [200] M. Uiberacker et al. , *Nature* **446** (2007), 627.
- [201] J. Ullrich, *Rep. Prog. Phys.* **66** (2003), 1463.
- [202] J. Ullrich et al. , *J. Phys. B: At. Mol. Opt. Phys.* **30** (1997), 2917.
- [203] J.H. Van Vleck, *Proc. Nat. Acad. Sci. U.S.A.* **14** (1928), 178.
- [204] G.S. Voronov und N.B. Delone, *Zh. Eksp. Teor. Fiz.* **1** (1965), 66.
- [205] G.S. Voronov und N.B. Delone, *Zh. Eksp. Teor. Fiz.* **23** (1966), 54.
- [206] T. Weber et al. , *J. Phys. B: At. Mol. Opt. Phys.* **34** (2001), 3669.
- [207] E.P. Wigner, *Phys. Rev.* **40** (1932), 749.
- [208] A. Wonisch et al. , *Appl. Opt.* **45** (2006), 4147.
- [209] V.S. Yakovlev und A. Scrinzi, *Phys. Rev. Lett.* **91** (2003), 153901.
- [210] V.S. Yakovlev et al. , *J. Mod. Opt.* **52** (2005), 395.
- [211] V.S. Yakovlev et al. , *Opt. Expr.* **15** (2007), 15351.
- [212] V.S. Yakovlev et al. , *Phys. Rev. Lett.* **105** (2010), 073001.
- [213] Y. Yamaguchi, *Phys. Rev.* **95** (1954), 1628.
- [214] Y. Yamaguchi und Y. Yamaguchi, *Phys. Rev.* **95** (1954), 1635.
- [215] H.B. Yang, *Phys. Rev. Lett.* **92** (2004), 246403.
- [216] G.L. Yudin et al. , *J. Phys. B: At. Mol. Opt. Phys.* **41** (2008), 045602.
- [217] J. Zhang et al. , *Opt. Expr.* **11** (2003), 601.
- [218] B. Zimmermann et al. , *Nat. Phys.* **4** (2008), 649.
- [219] W.H. Zurek, *Rev. Mod. Phys.* **75** (2003), 715.

Acknowledgments

Throughout this work, I received support from a very special group of researchers, who are driven by a passion for discovery that is rare even among scientists. First and foremost, I would like to thank Vlad Yakovlev not only for all the illuminating physics discussions and insights he provided to me, but also for the very useful and rewarding—both personally and professionally—research opportunities he gave to me. I cannot begin to repay Vlad for the amount of time and energy he has put into guiding my research. Discussions with my colleague Michael Korbman were also crucial in deepening my understanding of the quantum world, and to grasp concepts that I would have otherwise missed.

Also, in this respect I would like to thank Thomas Udem and Peter Hommelhoff¹ for an inspiring lecture on Quantum Optics. It was the very last physics course I took before graduating (knocking on wood), and is probably the one I'll remember the most. It blew my f@©#!ng mind!

Of course, I will not forget Prof. Dr.³ Andrey Kamarou. Although we haven't actually worked together, I got to know Andrey because he was in my office for a short while before he moved into the cage. Andrey and I had very interesting discussions about various subjects, such as technology, philosophy and linguistics. In fact, according to Andrey, I am a *Doctor of Divinity*!

I would also like to thank Elisabeth Magerl for helping me to understand a problem that had been bothering me for a long time: why the heck does Hawking radiation make a black hole become smaller!? You know, I just thought it was strange, because according to the mainstream explanation, Hawking radiation is generated when a particle-antiparticle pair is created near the event horizon, such that one enters the black hole and the other flies off into space. So, from the perspective of an outside observer, the black hole radiated a particle out, and therefore has lost energy which should make it become smaller. But the thing is, if the black hole gobbled up the other particle, shouldn't it have actually gotten bigger, regardless of what the other particle does? Mass is always positive after all. Well now, thanks to Elisabeth, I know the answer to why the black hole becomes smaller as a result of Hawking radiation, and I'll leave it to my defense committee to ask me why this is so.

During my degree, I had the chance to collaborate with many other very bright and very inspiring colleagues. I'm thinking of you, Martin Schultze (Martinius!), Ivanka Grguras,

¹Also, Peter, thanks for teaching an ignorant Canadian how to properly pour a weißbier! Although I was quite drunk at the time, I still remember how to do it!

Markus Fieß, Michael Hofstetter, Mohammed Hassan, and Adrian Wirth. I've also had the pleasure to discuss physics with Andreas Maier and Adrian Cavalieri, who, together with Reinhard Kienberger and Wolfram Helml are doing pioneering measurements at the new LCLS facility.

Wolfie in particular deserves special praise for insisting that I read books. Currently, my official policy is to not read books. Why? Because I'm part of the generation that doesn't read books, it's as plain and simple as that. I'm part of the generation where girls only care about their looks, and guys just don't read books. But Wolfie he's a missionary crusader, and he recently lent me a book that I find quite intriguing, it's called Schrödinger's Cat. So let's see, I might begin to read books...

Of course, I can't forget the interesting and illuminating physics discussions I had with Eleftherios Goulielmakis. Lefteris was sitting in the office right next door to mine. So whenever I felt like chatting about arbitrary things, including but not limited to physics, and venting my frustrations about my papers getting rejected all the time, Lefteris was *always* there for support. He's quite a morale booster. And then, when Nicholas Karpowicz joined the group and moved in with Lefteris, all of a sudden I found myself floating over to the office next door twice as often! Nick is quite an amazing guy as well, he's a theorist and an experimentalist *at the same time*, literally, I don't know how he does it. By the way Nick, why is it that unicorns have only one horn? I have to say, I'm not entirely satisfied with the answer you got from the Fabelwesenplanungsausschuss. Tell me, what is the *real* correct answer? Here, I'll give you a hint: it starts with an "F".

Before moving in with Lefteris, Nick was initially sharing an office in the cage with Balint Horvath, who left back in 2009. Balint was an influential figure for me because he introduced me to kool music, kool clubs, and the city of Hamburg! Man, I'll never forget when Balint and I joined up with Franz Tavella for one surreal weekend of partying in Hamburg, the Reeperbahn was something else... While we were there, we also met up with Antonia Popp from the MPQ and Giuseppe Sansone from the Politecnico in Milano—some other people were with us but I don't remember their names².

Hamburg is a pretty messed up place, I'll tell you that much. I remember as we were entering the city, Balint and I were looking around, and asking ourselves why were all these junkies littering the U-Bahn, oh my god they were everywhere! Was the entire city of Hamburg populated with junkies? Following a weekend of (cough, cough) fun and games, we eventually returned home to Munich, somehow. Once landed in Munich, we looked at the people walking around at the Flughafen München, and we saw a bunch of posh snobs. We paused, and thought to ourselves, what's wrong with all these people walking around with such nice clothes and their noses in the air? And then we paused again... looked at each other, then looked at the snobs, and then realized that *we* were now the junkies! In my acknowledgments, I have to thank the municipality of Hamburg for turning me into a junkie, it's a very magical place. However, Hamburg also helped me to become a real adult. "All the Hamburgers of the world **unite!**"

But parties didn't only happen in Hamburg, let me tell you, because obviously Munich

²Don't worry, they were cool too.

has the Oktoberfest going on every year! The best time I had there was last year, when my good friend Daniel Herrmann twisted my arm to go with the high-field people, including Johannes Wenz, Christoph Wandt, Antonia Popp, Sandro Klingebiel, Christoph Skrobol, Mattias Fuchs and I'm sure some other colleagues were there, but I don't remember exactly who... oh yeah, Shao Wei Chou was also there, and he could barely stand up towards the end of the evening, hahaha! We were dancing around the tables singing crappy 70's redneck music the whole time, it was amazing. To be sure, you can always count on the high-field people for an awesome party!

But if my entire social interaction with colleagues was constant unrestrained madness and drunken delirium, I think my mind would have been reduced to a little dried nut before I could even have had the chance to graduate! You know, it's also important to experience quiet and happy moments too. I remember such happy and reasonable times spent in the company of Chris Sears and Laura Sears. My wife Jia and I got to know them well thanks to our exchange of cat-sitting services. Chris and Laura are now back in California, and I wish them all the best there.

I am also grateful to Raphael Tautz for his hospitality, and the tasty smoked meat he had me try at his home. Raphael is also a fan of computer games, and we had a great time playing Unreal Tournament. I also remember having quite a few good laughs with Tibor Wittman, Yutaka Nomura (Yutaka, sorry that I got your bike stolen, but your TV still works perfectly fine), Laszlo Veisz, Augustin Schiffrin (Augustin, calice, fais attention aux ours!), Lauryna Lötscher, Ioachim Pupeza (Geile Sau!), Julia Mikhailova, Stefan Karsch, Matthias Kling and Nora Johnson (the Jayhawkers), Matthias Kübel and Oliver Herrwerth³. As well, Sergei Rykovanov was, to the best of my knowledge, the only one who managed to find the W.E.T. C.R.A.P. pseudo-acronym I hid in my 2009 Frauen Chiemsee presentation. By the way, Sarah Stebbings and Simon Watson should know that I can now correctly pronounce "Worcestershire", check it out: wustərʃər! In addition to all these wonderful colleagues, I am deeply indebted to my digital spiritual friends Gottfrid Svartholm and Frederik Neij for providing me with hours upon hours of entertainment.

Of course, I certainly cannot forget my Chinese connection: Tiejun Wang, Xueqing Yan, Hui Chun Wu and Yunpei Deng. Despite our cultural differences, we had some very fun times together! Tiejun mon tabernacle, comment trouves-tu ça à Québec? J'espère que tout va bien pour toi là-bas, et que t'aimes ton poste à l'université Laval. On prendra bien une brosse ensemble un jour, soit à Québec ou en Chine, peu importe. Xueqing, I hope all is going well for you and Jiao Shia back in Beijing, I certainly hope to see you there some time. Hui Chun, it also a great pleasure meeting you, and I'm glad I got to see you once again this year during Prof. Meyer-ter-Vehn's birthday. I wish you all the best in Los Alamos, and please keep away from dangerous radiation (stay with the good vibes). Yunpei, Yunpei, what can I say? Well, I'll begin with an apology: I'm sorry for grabbing your head like a basketball. I could tell that you were angry about that, and rightly so. You're an awesome guy, my friend! I think you'll be doing great things in the future. I

³I owe several masses of beer to Matthias, Oliver and Balint, who kindly translated my Summary to the Zusammenfassung.

wish all goes well for you during your quest for professorship. When they put hoops in front of you, don't just jump through them, *burn* through them man! Serve them their own asses on a golden platter, just like the Italians and the Spanish did to the Germans this year.

All this being said, if it were not for Ferenc Krausz, who provided invaluable guidance to me throughout my research, I would not have had this wonderful opportunity to participate in such ground-breaking science and meet all these amazing people. I have yet to comprehend how Ferenc can manage so many projects at once, and still find the time to provide excellent guidance to his $\gtrsim 100$ students. Ferenc I have to say, you are quite The Professor!

Finally, I would like to express my love to my family—my mom June, my dad Martin and my sister Lisa—as well as to my beloved parents in law—Mama Mei and Baba Zhi Qiang—for their support. And last but not least, to my lovely and beautiful wife Jia Zhou, who has always been by my side, providing her continual support to me here in Germany. Thank you, I love you my little darling baboushka!

Personal Record

Justin Gagnon

Born: July 12, 1981, in Halifax, Nova Scotia, Canada

Nationality: Canadian

Education:

2000-2004 Bachelor of Science, Honours Physics

University of Ottawa

thesis: *Analytical Characterization of Polarization Mode Dispersion and Polarization-Dependent Losses in Optical Fibers*

advisor: Liang Chen

2004-2006 Master of Science, Physics

University of Ottawa and National Research Council Canada

thesis: *Laser Coulomb Explosion Imaging of Polyatomic Molecules*

advisor: Paul Corkum and Ravi Bhardwaj

2007- Doctoral studies, Theoretical Physics

Ludwig-Maximilians-Universität München and

Max-Planck-Institut für Quantenoptik

thesis: *Attosecond Electron Spectroscopy – Theory and its Applications*

advisor: Ferenc Krausz

List of Publications

1. E. Goulielmakis, M. Schultze, M. Hofstetter, V. S. Yakovlev, J. Gagnon, M. Uiberacker, A. L. Aquila, E. M. Gullikson, D. T. Atwood, R. Kienberger, F. Krausz and U. Kleineberg, *Single-cycle nonlinear optics*, Science **320** (2008), 1614
2. J. Gagnon, E. Goulielmakis and V. S. Yakovlev, *The accurate FROG characterization of attosecond pulses from streaking measurements*, Appl. Phys. B **92** (2008), 25
3. J. Gagnon, K. F. Lee, D. M. Rayner, P. B. Corkum and V. R. Bhardwaj, *Coincidence imaging of polyatomic molecules via laser-induced Coulomb explosion*, J. Phys. B: At. Mol. Opt. Phys. **41** (2008), 215104
4. J. Gagnon and V. S. Yakovlev, *The robustness of attosecond streaking measurements*, Opt. Expr. **17** (2009), 17678
5. J. Gagnon, V. S. Yakovlev, E. Goulielmakis, M. Schultze and F. Krausz, *A New Generalized Projections Algorithm Geared Towards Sub-100 Attosecond Pulse Characterization*, Ultrafast Phenomena XVI: Proceedings of the 16th International Conference **92** (2009), 911
6. E. Goulielmakis, M. Schultze, M. Hofstetter, M. Uiberacker, J. Gagnon, V. S. Yakovlev, U. Kleineberg, F. Krausz, *Sub-100-as soft x-ray pulses*, Ultrafast Phenomena XVI: Proceedings of the 16th International Conference **92** (2009), 3
7. E. Goulielmakis, M. Schultze, F. Reiter, U. Graf, J. Gagnon, M. Hofstetter, V. S. Yakovlev, R. Kienberger, U. Kleineberg and F. Krausz, *En route to the generation and attosecond control of intense single-cycle light pulses*, 2009 IEEE LEOS Annual Meeting Conference Proceedings (2009), 313
8. M. Schultze, M. Fieß, N. Karpowicz, J. Gagnon, M. Korbman, M. Hofstetter, S. Neppl, A. L. Cavalieri, Y. Komninos, T. Mercouris, C. A. Nicolaides, R. Pazourek, S. Nagele, J. Feist, J. Burgdörfer, A. M. Azzeer, R. Ernstorfer, R. Kienberger, U. Kleineberg, E. Goulielmakis, F. Krausz and V. S. Yakovlev, *Delay in Photoemission*, Science **328** (2010), 1658
9. V. S. Yakovlev, J. Gagnon, N. Karpowicz and F. Krausz, *Attosecond Streaking Enables the Measurement of Quantum Phase*, Phys. Rev. Lett. **105** (2010), 073001
10. M. Hofstetter, M. Schultze, M. Fieß, A. Guggenmos, J. Gagnon, E. Magerl, E. Botschafter, R. Ernstorfer, R. Kienberger, E. Gullikson, F. Krausz, U. Kleineberg, *First*

Attosecond Pulse Control by Multilayer Mirrors above 100 eV Photon Energy, 17th International Conference on Ultrafast Phenomena, 2010

11. J. Gagnon, V. S. Yakovlev and F. Krausz, *Laser-dressed scattering of an attosecond electron wave packet*, Phys. Rev. A: At. Mol. Opt. Phys. **82** (2010), 033435

12. M. Fieß, M. Schultze, E. Goulielmakis, B. Dennhardt, J. Gagnon, M. Hofstetter, R. Kienberger and F. Krausz, *Versatile apparatus for attosecond metrology and spectroscopy*, Rev. Sci. Instrum. **81** (2010), 093103

13. J. Gagnon and V. S. Yakovlev, *The direct evaluation of attosecond chirp from a streaking measurement*, Appl. Phys. B (2010), accepted

14. M. G. Hofstetter, M. Schultze, M. Fieß, B. Dennhardt, A. Guggenmos, J. Gagnon, V. S. Yakovlev, E. Goulielmakis, R. Kienberger, E. M. Gullikson, F. Krausz and U. Kleineberg, *Attosecond dispersion control by extreme ultraviolet multilayer mirrors*, Opt. Expr. **19** (2011), 1767